CCM 79-7

Center for Composite Materials

THE ULTRASONIC INSPECTION OF INTERLAMINAR DAMAGE IN COMPOSITE MATERIALS

BRUCE ALLEN YOST

DEPARTMENT OF DEFENSE
PLASTICS TECHNICAL EVALUATION CENTER
ARRADCOM, DOVER, N. J. 07801

College of Engineering
University of Delaware
Newark, Delaware

DISCLAIMER NOTICE

THIS DOCUMENT IS BEST QUALITY AVAILABLE. THE COPY FURNISHED TO DTIC CONTAINED A SIGNIFICANT NUMBER OF PAGES WHICH DO NOT REPRODUCE LEGIBLY.

-- 1 OF 2
-- ***DTIC DOES NOT HAVE THIS ITEM***
-- 1 - AD NUMBER: D429734
-- 5 - CORPORATE AUTHOR: DELAWARE UNIV NEWARK CENTER FOR COMPOSITE
-- MATERIALS
-- 6 - UNCLASSIFIED TITLE: THE ULTRASONIC INSPECTION OF INTERLAMINAR
-- DAMAGE IN COMPOSITE MATERIALS,
-- 10 - PERSONAL AUTHORS: [illegible],
-- 11 - REPORT DATE: MAY 15, 1973
-- 12 - PAGINATION: 124P
-- 14 - REPORT NUMBER: CCM-73-7
-- 20 - REPORT CLASSIFICATION: UNCLASSIFIED
-- 21 - SUPPLEMENTARY NOTE: PRESENTED AS A SENIOR THESIS.
-- 22 - LIMITATIONS (ALPHA): [illegible] DISTRIBUTION
-- UNLIMITED. AVAILABILITY: CENTER FOR COMPOSITE MATERIALS, COLLEGE OF
-- ENGINEERING, UNIVERSITY OF DELAWARE, NEWARK, DELAWARE 19711.
-- 33 - LIMITATION CODES: 1 2
-- ******
-- 2 OF 2
-- ***DTIC DOES NOT HAVE THIS ITEM***
-- 1 - AD NUMBER: D910207
-- 5 - CORPORATE AUTHOR: DELAWARE UNIV NEWARK CENTER FOR COMPOSITE
-- MATERIALS

-- 6 - UNCLASSIFIED TITLE: THE ULTRASONIC INSPECTION OF INTERLAMINAR
-- DAMAGE IN COMPOSITE MATERIALS
-- 10 - PERSONAL AUTHORS: YOST,BRUCE ALLEN ,
-- 11 - REPORT DATE: MAY , 1973
-- 12 - PAGINATION: 124P
-- 14 - REPORT NUMBER: CCM-73-7
-- 20 - REPORT CLASSIFICATION: UNCLASSIFIED
-- 22 - LIMITATIONS (ALPHA): AVAILABILITY: REQUEST FROM CENTER FOR
-- COMPOSITE MATERIALS, UNIVERSITY OF DELAWARE, NEWARK, DE 19711.
-- 33 - LIMITATION CODES: 1
-- ******
-- END OF DISPLAY LIST

-- ENTER "?" FOR COMMANDS

THE ULTRASONIC INSPECTION OF INTERLAMINAR DAMAGE IN COMPOSITE MATERIALS

PRESENTED BY

Bruce A. Yost

and

Dr. R. Byron Pipes

Center for Composite Materials

University of Delaware

Newark, Delaware

on

May 10, 1979

for

Senior Thesis

Abstract

Ultrasonic inspection techniques were used to interrogate the internal damage of E glass/epoxy disks (3M - Scotchply 1003) that had been subjected to fatigue loadings and static loadings. Two types of disks were examined; defective disks which contained implanted Teflon defects of various sizes and pristine disks with no implanted defects. The growth of overall damage in each disk, as well as, the growth of individual delaminations were monitored with "C" scan techniques. The location of each delamination was determined through examination of the reflected waveform; photomicrographs revealed the actual location of each delamination and the two results were compared. Locations of delaminations were adequately determined by the ultrasonic methods. Finally, a finite element model of a pristine disk was developed. The validity of this model was proven through comparison of predicted and observed deflections and radial strains.

Table of Contents

Nomenclature

Symbol	Definition
A_{ij} (i,j = 1,2,6)	Extensional stiffness matrix
a	Radius of a disk
B_{ij} (i,j = 1,2,6)	Bending-stretching coupling matrix
Ch^{ij} (n = 1-4)	Constants
D	Flexural stiffness of a plate
D_{ij} (i,j = 1,2,6)	Flexural stiffness matrix
E^{ij}	Elastic modulus of a disk
Er	Elastic modulus in the radial direction
Ex	Elastic modulus in the x direction
Ex'	Elastic modulus in the x direction of a rotated coordinate system
Ey	Elastic modulus in the y direction
Ey'	Elastic modulus in the y direction of a rotated coordinate system
Eθ	Elastic modulus in the theta direction
G	Shear modulus of the laminate
h	Thickness of a disk
Mr	Stress couple in the radial direction
Mx	Stress couple in the x direction
Mxy	Stress couple in the x-y plane
My	Stress couple in the y direction
Mθ	Stress couple in the theta direction
P	Magnitude of a concentrated load
p	Magnitude of a lateral load
Q_{ij} (i,j = 1,2,6)	Stiffness matrix
r^{ij}	Radial distance from the center of a disk
w	Displacement in the z direction
z	Out of plane distance from the center of a disk
γxy	Shear strain in the x-y plane
∇^4	Biharmonic operator
εr	Radial strain
εx	Strain in x direction
εy	Strain in y direction
θ	Angle measurement
ν	Poisson's ratio of a disk
νrθ	Major Poisson's ratio of the laminate in polar coordinates
νxy	Major Poisson's ratio of the laminate in cylindrical coordinates

Nomenclature (Cont'd)

Symbol	Definition
νyx	Minor Poisson's ratio of the laminate in cylindrical coordinates
$\nu \theta r$	Minor Poisson's ratio of the laminate in polar coordinates
π	3.1416
σr	Stress in the radial direction
σx	Normal stress in the x direction
σy	Normal stress in the y direction
$\sigma \theta$	Stress in the theta direction
τxy	Shear stress in the x-y plane

List of Figures

List of Figures (cont'd)

List of Figures (cont'd)

List of Figures (cont'd)

List of Tables

I. Introduction

Today, many methods of detecting the internal damage of materials are in use. Acoustic emission, X-rays, and ultrasonic scanning are just a few of these methods. This paper deals with the ultrasonic inspection of interlaminar damage in E glass/epoxy (3M - Scotchply 1003) laminates with stacking sequences $[0/45/90/-45]_{2s}$. Ultrasonic "C" scanning is discussed in detail in Appendix A.

The details of manufacturing the fiberglass plates and the fiberglass disks are contained in Appendix B and Appendix C, respectively. Each disk was subjected to a fatigue load or a static load as described in Section II. These loads produced both bending stresses and interlaminar shear stresses. The shear stresses produced interlaminar damage near the loading point where the shear stresses were greatest. Ultrasonic "C" scans of this damaged area were made and are contained in Section III. Section III also contains photomicrographs of two damaged disks. These photomicrographs proved the validity of the ultrasonic "C" scan technique.

A finite-element model of a pristine disk is developed in Section IV, while Section V contains verification of the finite-element model. Deflection and radial strain comparisons are the two methods of verification of the finite-element model discussed in Section V.

Section VI offers conclusions and suggestions while References and Acknowledgments are found in Section VII and Section VIII, respectively.

II. Test Procedures

Three sets of tests were performed using the fiberglass disks. The tests were called Fatigue I, Fatigue II, and Static I, respectively. Each test utilized the apparatus shown in Figure 1. This apparatus consists of a plunger and a collar. Inside the collar is a knife edge that is 4.75 inches in diameter. The knife edge provided simple support boundary conditions for the disks. The plunger contained an adaptation on one end which allowed various sizes of ball bearings to be inserted into the end of the plunger. The ball bearings approximated a point load; the loads, whether they were fatigue or static, were always applied at the center of the disk. Four sizes of ball bearings were used - 1.000 inches, 0.875 inches, 0.75 inches, and 0.50 inches in diameter.

A. Fatigue I Phase

The testing performed in the Fatigue I Phase utilized the disks numbered 51-74. After some experimentation and two static tests to determine an approximate maximum load for an unflawed disk, a mean load for the fatigue loading was chosen. A sinusoidal loading, with the chosen mean load of 181.8 lb compression and a load amplitude of 148.7 lb, was imposed at a frequency of 10 Hz. Each disk was loaded for a specified number of cycles and then scanned to detect flaw growth or propagation (see Table 1A; the number of cycles shown are cumulative). By scanning the disks after each cycle interval, a cumulative history of the fatigue damage was obtained. In addition

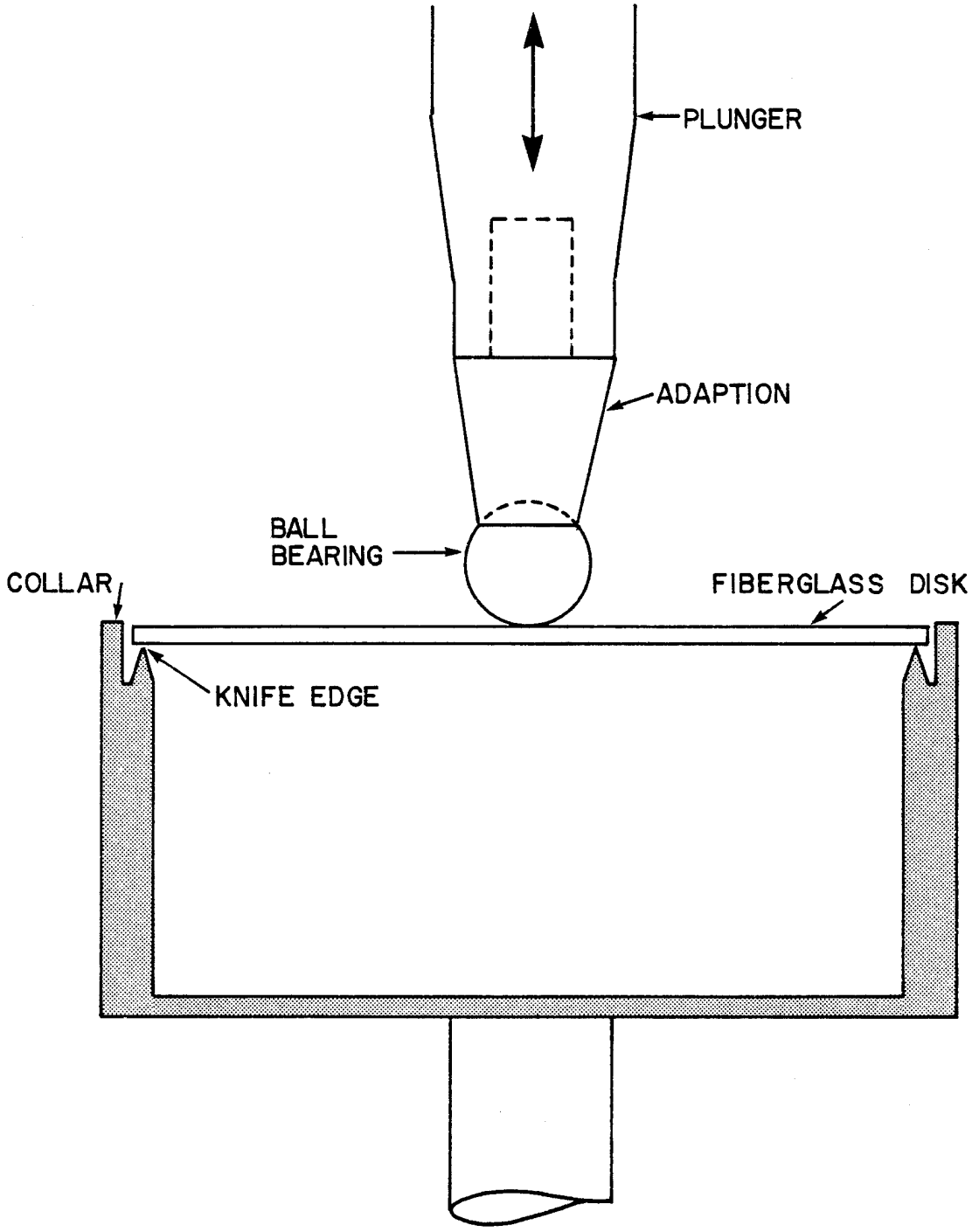

Figure 1 The Test Fixture

Table 1 A Fatigue I Test Program

No. of Cycles / Disk	1000	2500	3750	5000	7500	10000	15000	20000	30000	40000	50000
51	X	X	X	X	X	X	X	X	X	X	X
52	X	X	X	X	X	X	X	X	X	X	X
53	X	X	X	X	X	X	X	X	X	X	X
54	X	X	X	X	X	X	X	X	X	X	X
61	X	X	X	X	X	X	X	X			
62	X	X	X	X	X	X	X	X	X	X	X
63	X	X	X	X	X	X	X	X	X	X	X
64	X	X	X	X	X	X	X	X			
71	X	X	X	X	X	X	X	X			
72	X	X	X	X	X	X	X	X	X	X	X
73	X	X	X	X	X	X	X	X	X	X	X
74	X	X	X	X	X	X	X	X	X	X	X

X - Tested at the corresponding number of cycles

to obtaining the damage pictorial, the tests were designed to study the effects of ball bearing size on the rate and amount of damage developed. The disks numbered 51, 61, and 71 were loaded with a one-half inch diameter ball bearing, while 52, 62, and 72 were loaded with a three-quarters inch ball. A seven-eighths inch diameter ball was used in conjunction with 53, 63, and 73 while 54, 64, and 74 were tested using a one inch diameter ball.

B. Fatigue II Phase

The Fatigue II Phase involved the disks numbered 111-133. The fatigue loading utilized in Fatigue I, as well as, the method of incremental scanning were very similar to those of Fatigue II. The only differences between the Fatigue I and Fatigue II phases were the types of disks examined, the ball bearing size chosen, and the fatigue cycle increments. All of the disks in Fatigue II were loaded with a one inch diameter ball. In addition to obtaining a cumulative history of the overall fatigue damage of the disks through "C" scans, the testing was designed to study the growth of the implanted Teflon defect (see Table 1B; the number of cycles shown are cumulative).

C. Static I Phase

The disks numbered 81 - 104 were used in the Static I Phase. Each disk was statically loaded with a 1.0 inch diameter ball bearing in increments of 220 lb. After the desired loading was obtained, each disk was unloaded and scanned to detect general damage in the disk and any growth of the implanted Teflon defect. Both sides of each disk were scanned to show the

Table 1 B Fatigue II Test Program

No. of Cycles / Disk	1000	2000	3000	4000	5000	7500	10000	15000
111	X	X	X					
112	X	X	X	X	X	X	X	X
113	X	X	X	X	X	X	X	X
114	X	X	X	X	X			
121	X	X	X	X	X			
122	X	X	X	X	X	X	X	X
123	X	X						
124	X	X	X	X	X	X	X	
131	X	X	X	X	X	X	X	
132	X	X	X	X	X	X	X	
133	X	X	X	X	X	X	X	

X - Tested at the corresponding number of cycles

damage above and below the implanted defect. The procedure of scanning both sides of the disk was identical to that used in Fatigue II (see Table 2; the loadings shown are not cumulative).

Table 2 Static I Test Program

Load (lb)	220	440	660
Disk			
81	X	X	X
82	X	X	X
83	X	X	X
84	X	X	X
91	X	X	X
92	X	X	X
93	X	X	X
94	X	X	X
101	X	X	X
102	X	X	X
103	X	X	X
104	X	X	X

X - Tested at the corresponding load

III. Test Results

In order to assess the internal damage of the defective and the pristine disks between loadings, ultrasonic scanning techniques that provided clear and concise pictures of the extent of the damage had to be developed. Three techniques of scanning that were used in evaluating the damaged disks are shown in Figure 2.

Technique "A" involves starting the gated region after the front surface reflection and ending it immediately after the back surface reflection. This setting provides cumulative information about the damage which exists in the disk. With such a gate setting, the scan shows the damaged regions as medium to dark gray. If, however, a large delamination lies near the front surface, any damage below this delamination will not be shown on the scan. Because the delamination is so large, the ultrasonic system treats the delamination as the back surface reflection and the waveform shown in Figure 3 appears on the oscilloscope. Notice that second and third multiples of this delamination are common when this situation occurs.

In technique "B", the gate is centered on the back surface reflection. Using this technique, any damage outside the gated region of the waveform shows as white to light gray on a scan. This technique was rarely used because the cumulative information of the damage in the disk that it offers is more difficult to interpret than that of technique "A".

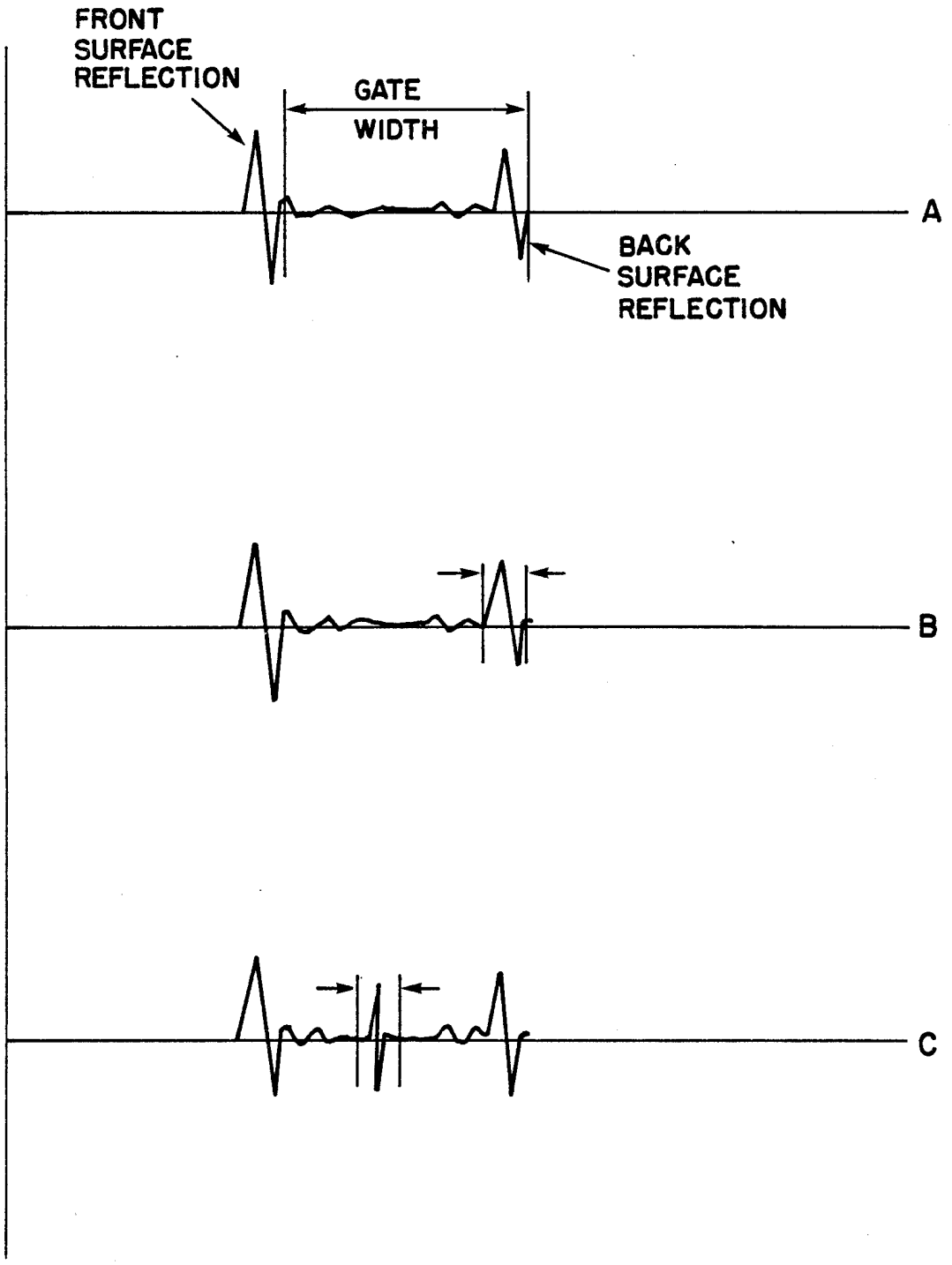

Figure 2 Gate Settings

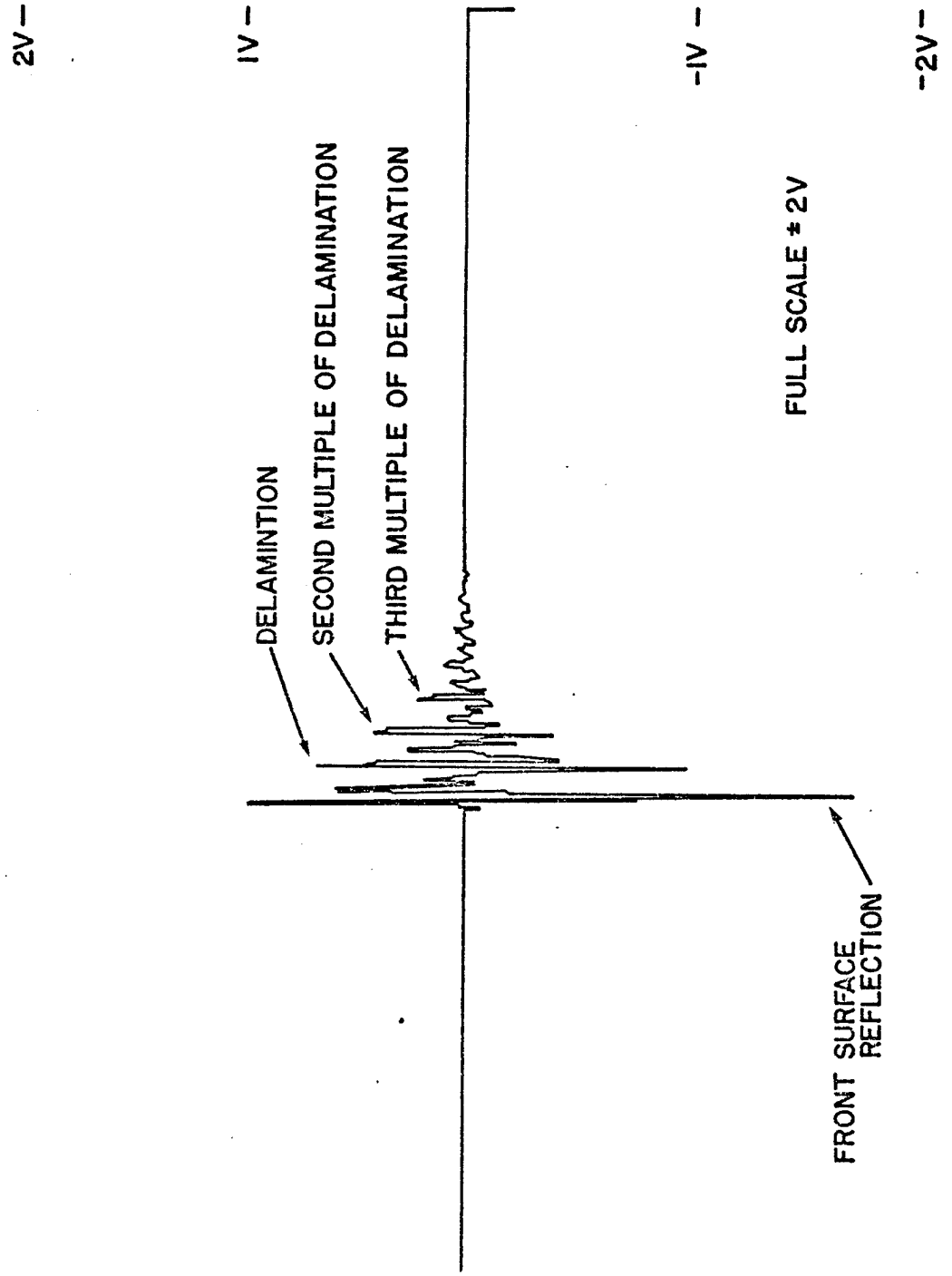

Figure 3 An Ultrasonic Waveform of a Damaged Region (x4)

To obtain a picture of the delamination, the width of the gate must be as small as possible as shown in technique "C". If the gate width is too large, other delaminations may appear in the scan or second multiples of delaminations that are closer to the front surface may also appear in the scan. Often, it is impossible to obtain a scan of a specific delamination because the reflection of a second multiple of another delamination coincides exactly with the delamination reflection. The resulting scan is a picture of the delamination and a second multiple of another delamination. This multiple effect presents a tremendous problem in isolating individual delaminations near the center of a disk. Thus, only delaminations near the surface can be clearly revealed because here, the second multiple effect is virtually non-existent.

To get an overall picture of the damage incurred to the fiberglass disks after they were tested, scanning technique "A" was used. Many attempts were made to find the right combination of settings on the ultrasonic equipment that would produce clear and informative scans. The settings that were finally chosen are listed in Figure 4. The gated waveform produced by these settings is shown in Figure 5, where the top waveform is the reflected waveform in its entirety and the bottom waveform is the gated portion of the reflected waveform.

The scans from the Static I Phase are shown in Figures 7, 8, 9, and 10. These scans were taken after a static load of 660 lb had been applied to each disk. Each scan is representative of the damage incurred in the other disks with the same size implanted defect. The scans show that the overall damage for each type of disk was approximately the same. The

"C" SCAN DATA SHEET

TRANSDUCER	ANTOM				
FREQ (MHz)	20				
TYPE	TUNED				
FOCUSSED LENGTH	1.25 in.				
INTENSITY	1.6				
SCAN SPEED	5	INDEX SPEED	10	INDEX INCR.	.010 in.
REP RATE	5K				
DAMPING	50Ω				
ENERGY	2				
RECVR. ATTEN	04				
H.P. FILTER	OUT				
BLANKING	40 μ sec				
MAIN BANG DELAY	50 μ sec				
INTERFACE DELAY	2.2 μ sec				
GATE DELAY	50.2 μ sec				
GATE WIDTH	2.3 μ sec				
PEAK POLARITY	POSITIVE				
PEAK GAIN	X10				
RCVR. GAIN	40 dB				
MODE	P/E INTERFACE				

NOTES

THESE SETTINGS WERE STANDARD FOR EVERY "C" SCAN

Figure 4 "C" Scan Data Sheet

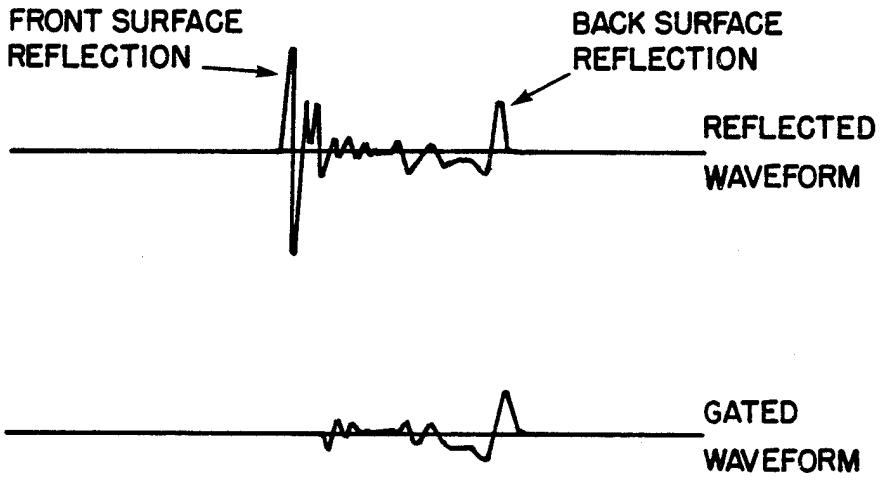

Figure 5 Gated Waveform No. 1

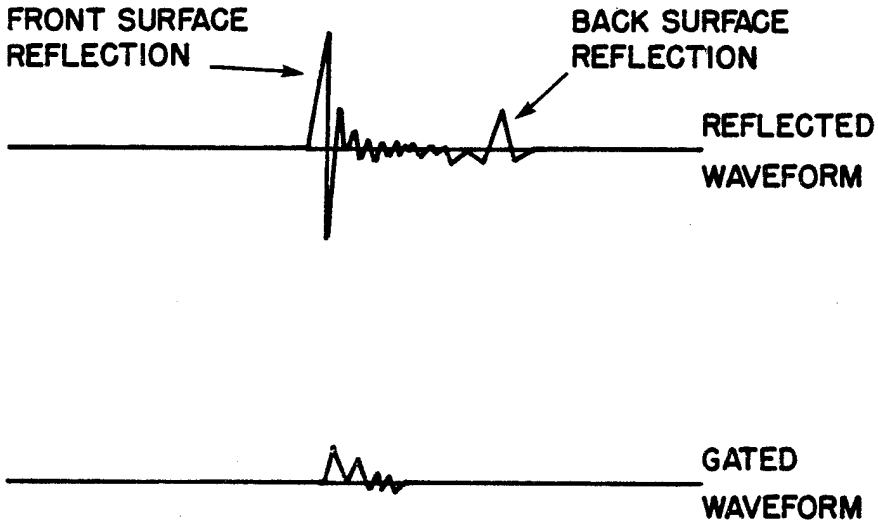

Figure 6 Gated Waveform No. 2

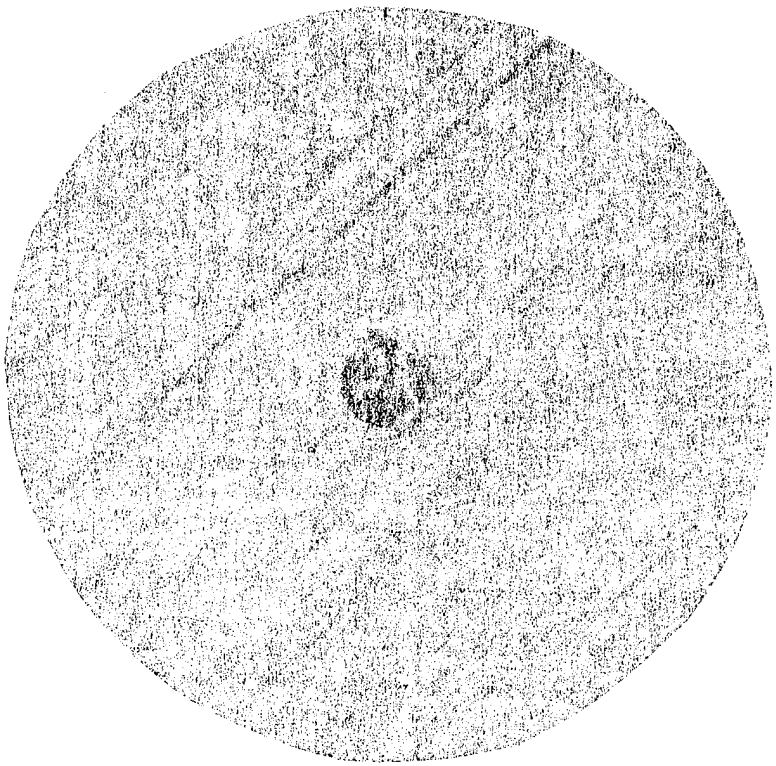

Scan of the loaded side of the disk

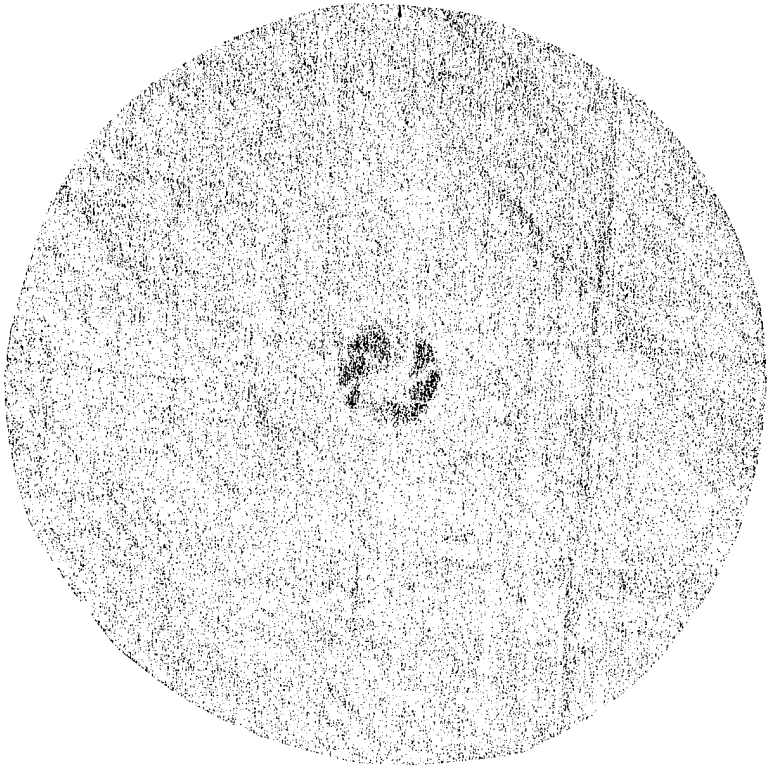

Scan of the unloaded side of the disk

Figure 7 Scans of Disk 81 After a 660 lb. Load

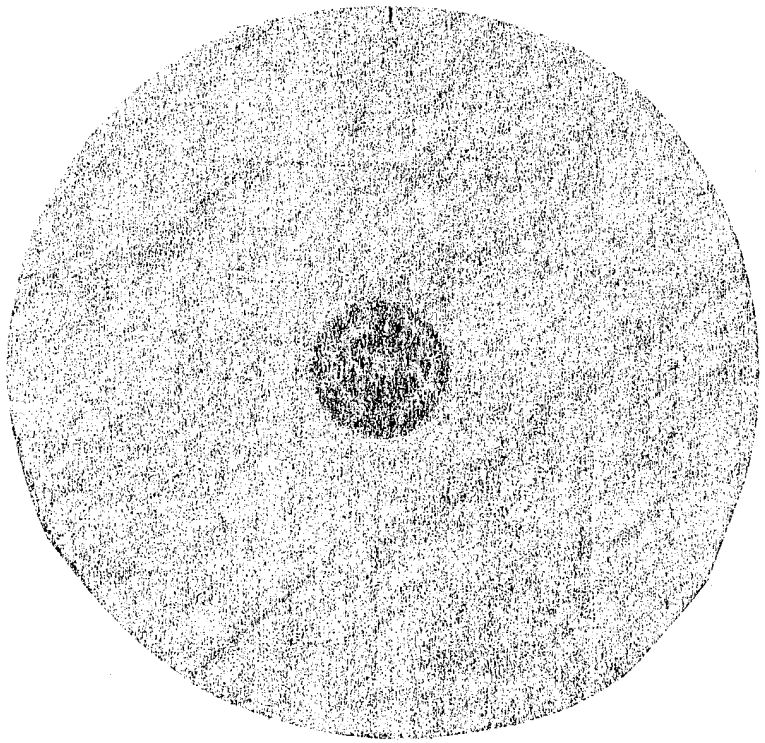

Scan of the loaded side of the disk

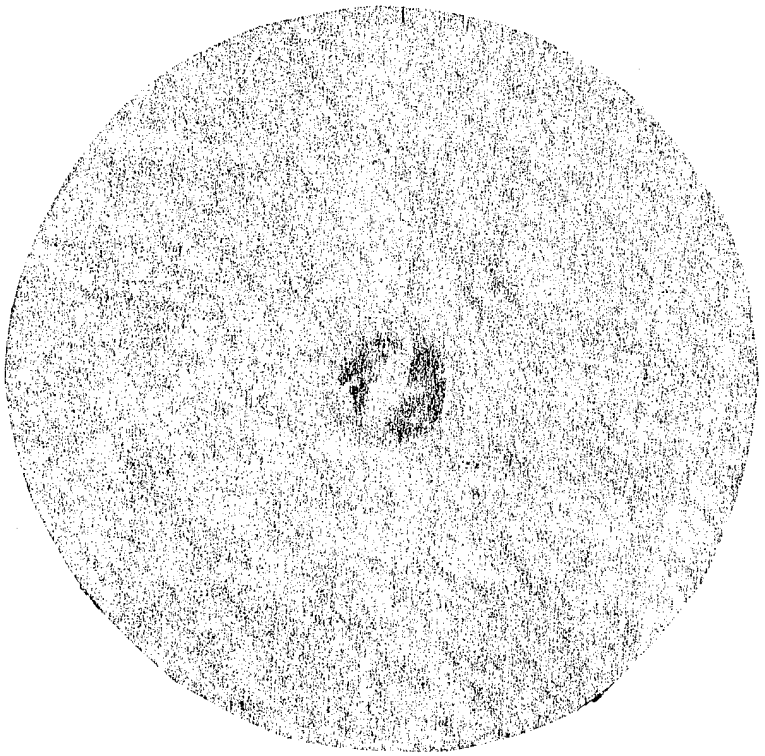

Scan of the unloaded side of the disk

Figure 8 Scans of Disk 92 After a 660 lb. Load

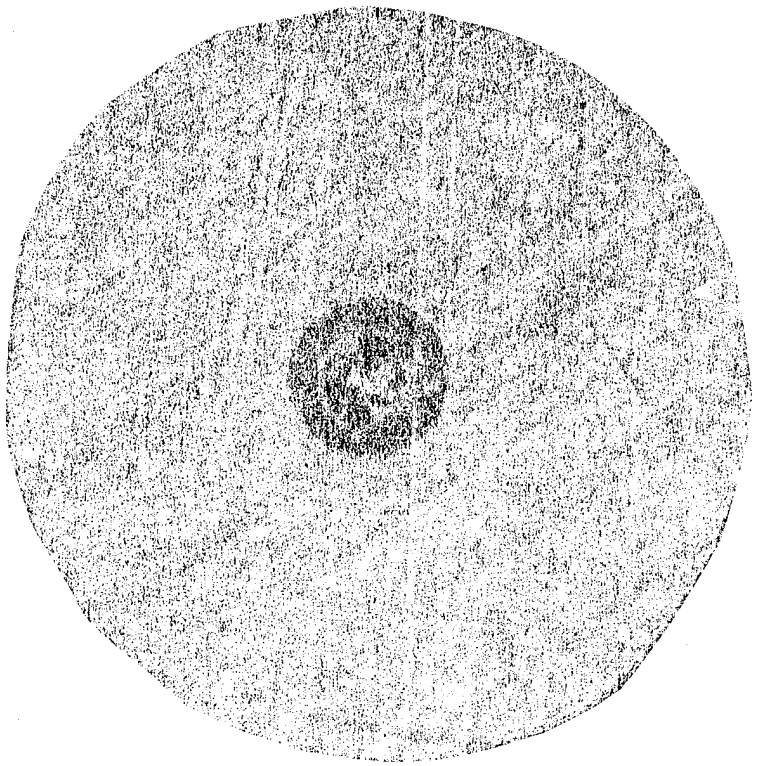

Scan of the loaded side of the disk

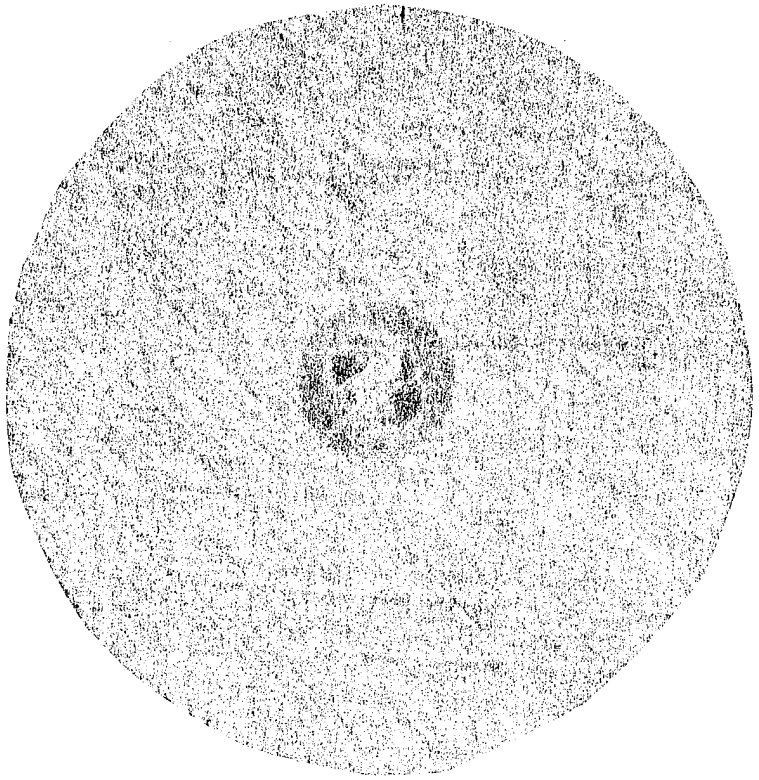

Scan of the unloaded side of the disk

Figure 9 Scans of Disk 83 After a 660 lb. Load

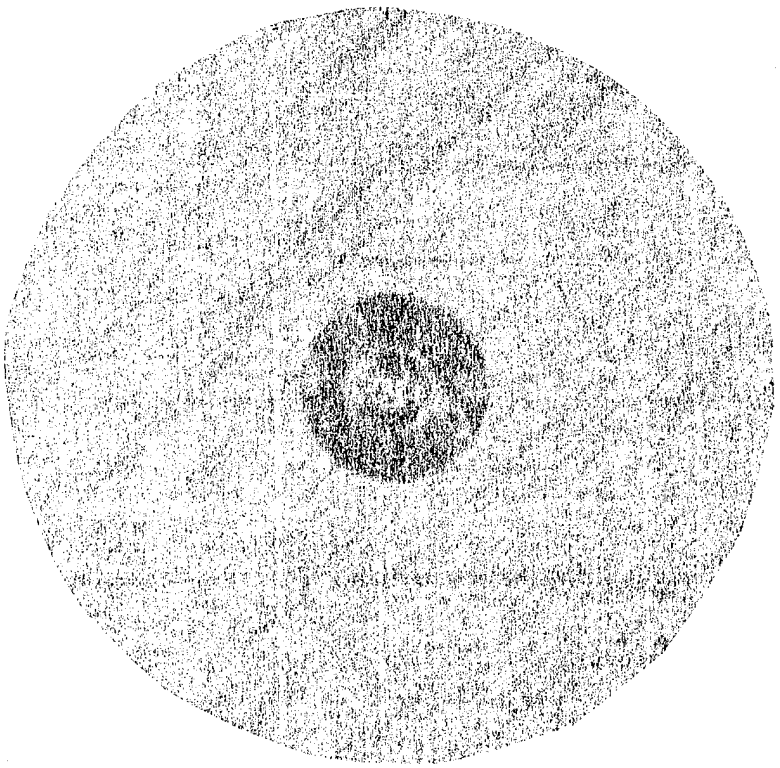

Scan of the loaded side of the disk

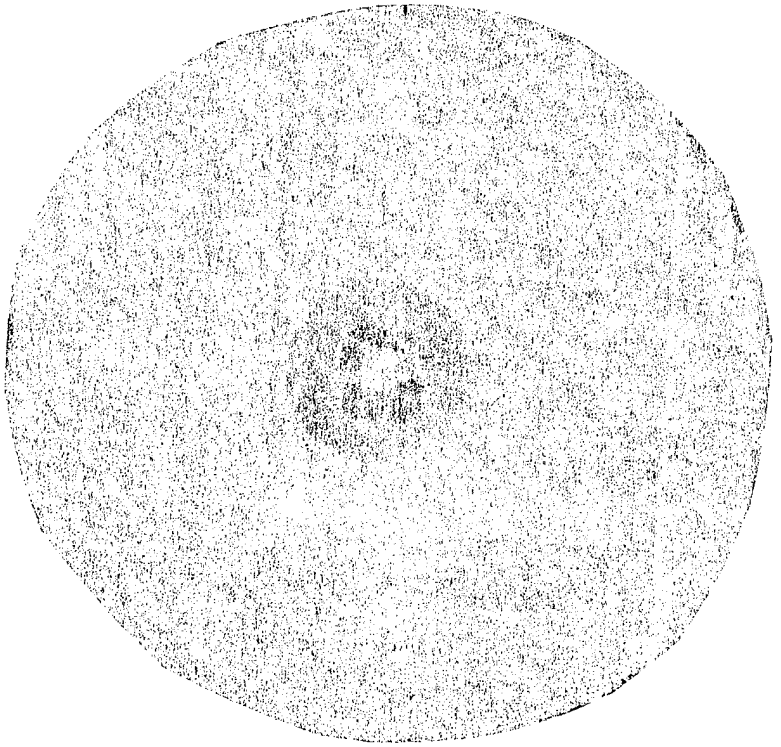

Scan of the unloaded side of the disk

Figure 10 Scans of Disk 94 After a 660 lb. Load

damaged area appears to lie above and below the implanted defect; no implanted defect showed any evidence of growth. The damaged area appears to form "lobe-like" patterns that are symmetrical around the center of the disk. The scan for disk 81 (unloaded side of the disk) shows the lobes that have developed due to the static loading of the disk.

The scans from the Fatigue II Phase are shown in Figures 11, 12, 13, and 14. These scans were taken after 10,000 cumulative cycles of fatigue loading. Each scan is representative of the damage incurred by the other disks with the same implanted defect size. Again, the overall damage for each type of disk was approximately the same and the damaged area forms "lobe-like" patterns. However, the damaged areas are much larger than those of the disks statically loaded and the lobes of damaged areas are much more evident. Most of the damaged areas appear to lie above and below the implanted defects. However, the size of the damaged areas (many of which cover the implanted defects) allow no conclusions to be made as to whether the implanted defects have propagated or not.

To determine the growth of implanted defects, a photomicrograph was made of disk 121 after 5000 cycles. Producing a photomicrograph of a disk involves three basic steps. They are:

1. The portion of the disk that one wishes to photomicrograph is sectioned by a diamond saw. Figure 15 shows the region cut from disk 121.
2. The specimen is mounted in an epoxy base and a selected side of the specimen is polished with 5 types of wet sandpaper (180, 240, 320, 400, and 600 grit) and 5 types of diamond dust (9, 6, 3, 1, and .25 micron).

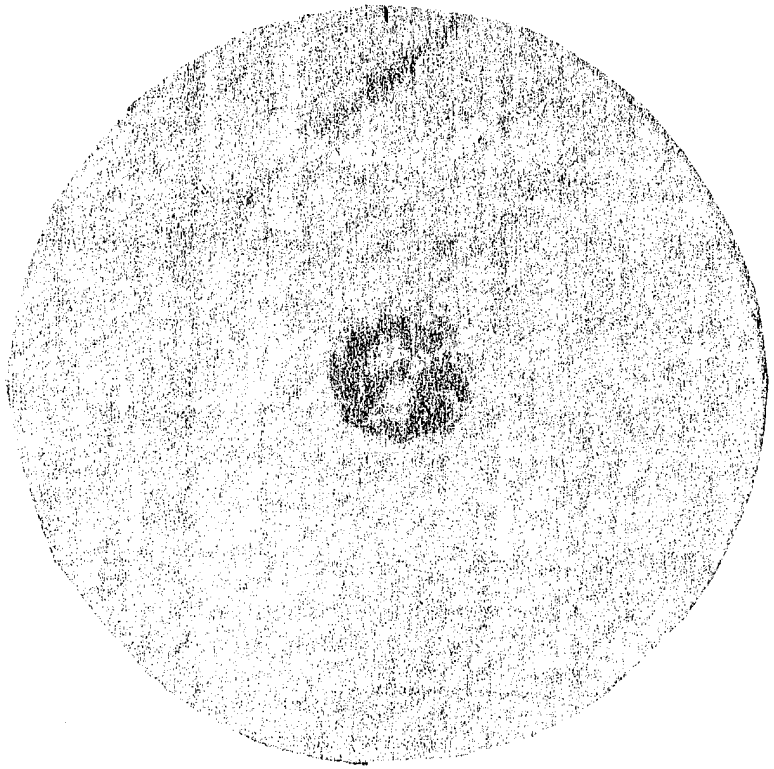

Scan of the loaded side of the disk

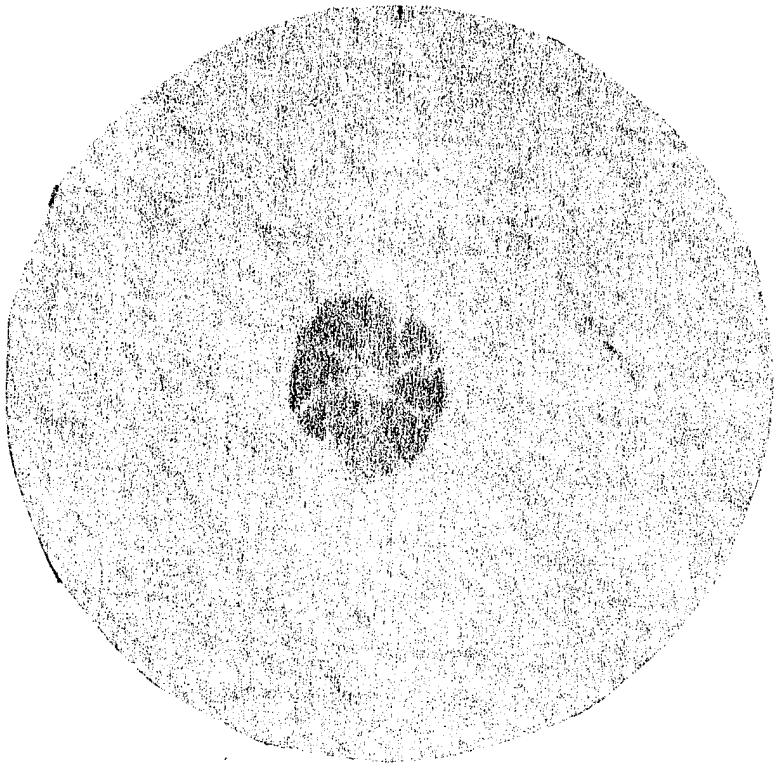

Scan of the unloaded side of the disk

Figure 11 Scans of Disk 131 After 10,000 Fatigue Cycles

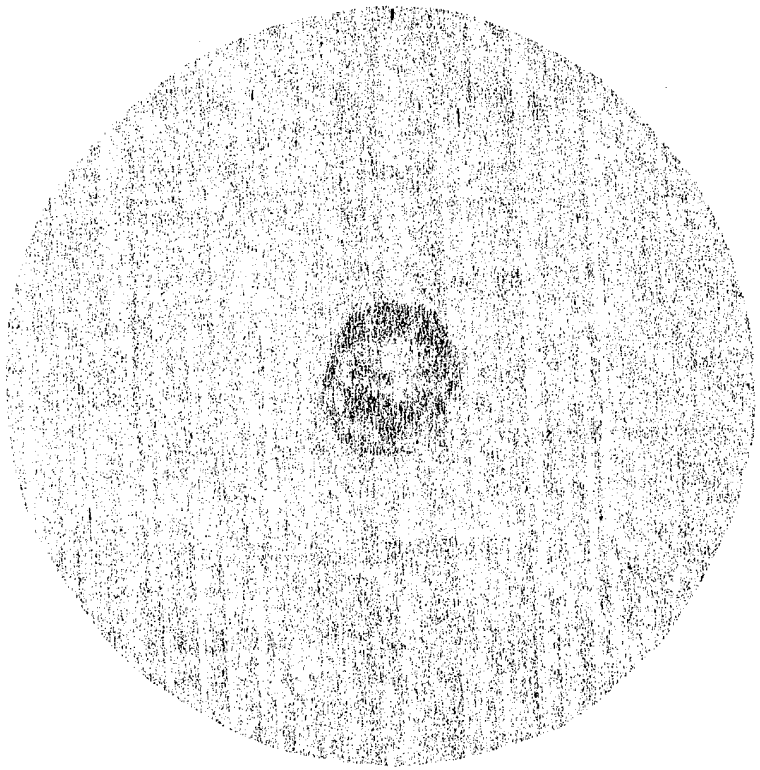

Scan of the loaded side of the disk

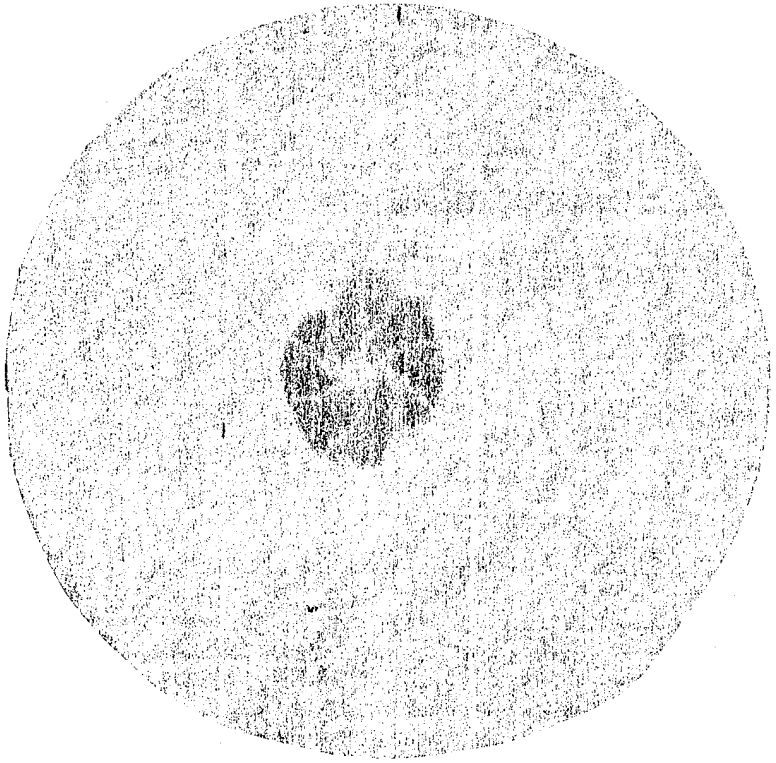

Scan of the unloaded side of the disk

Figure 12 Scans of Disk 122 After 10,000 Fatigue Cycles

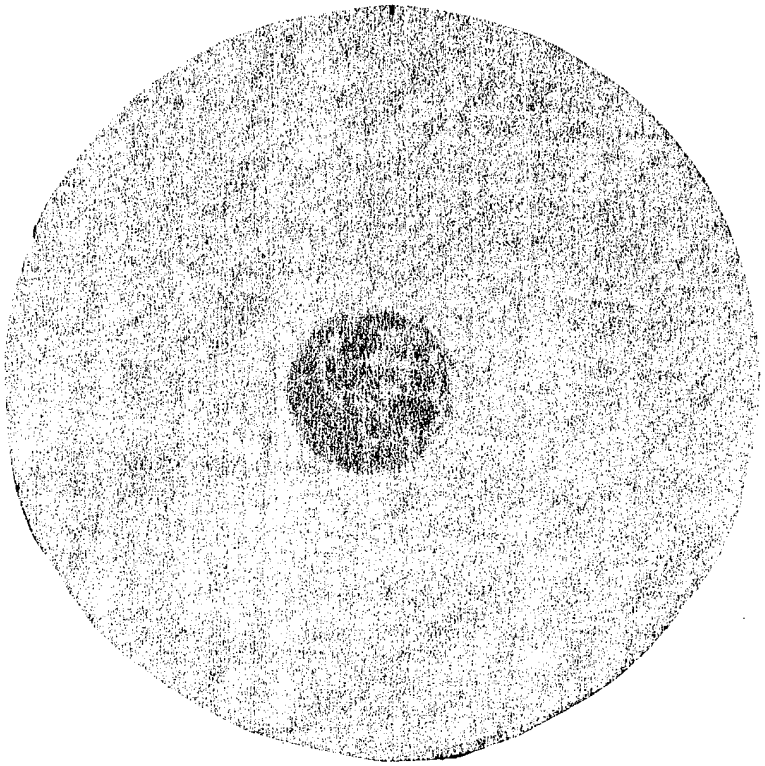

Scan of the loaded side of the disk

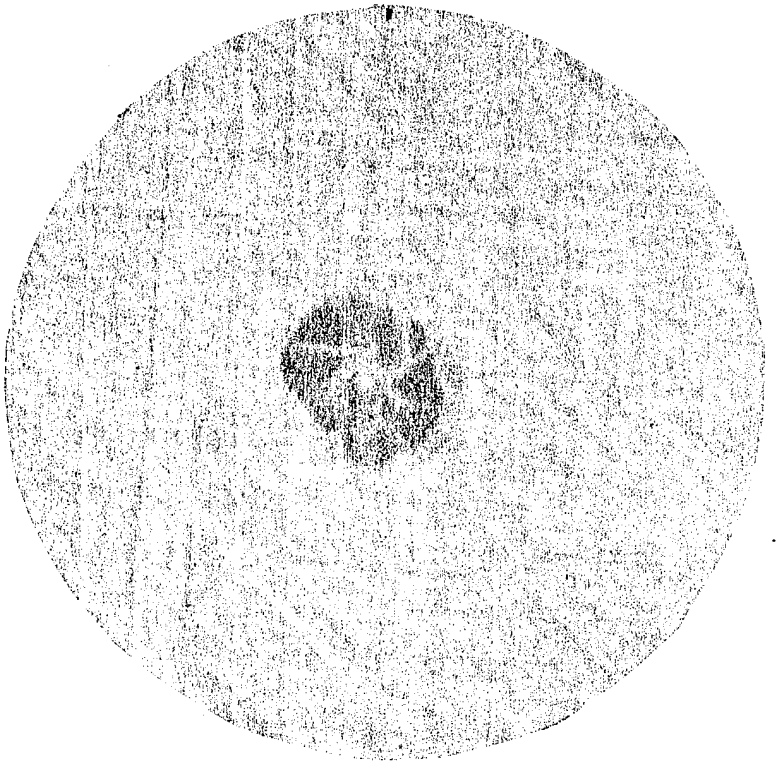

Scan of the unloaded side of the disk

Figure 13 Scans of Disk 113 After 10,000 Fatigue Cycles

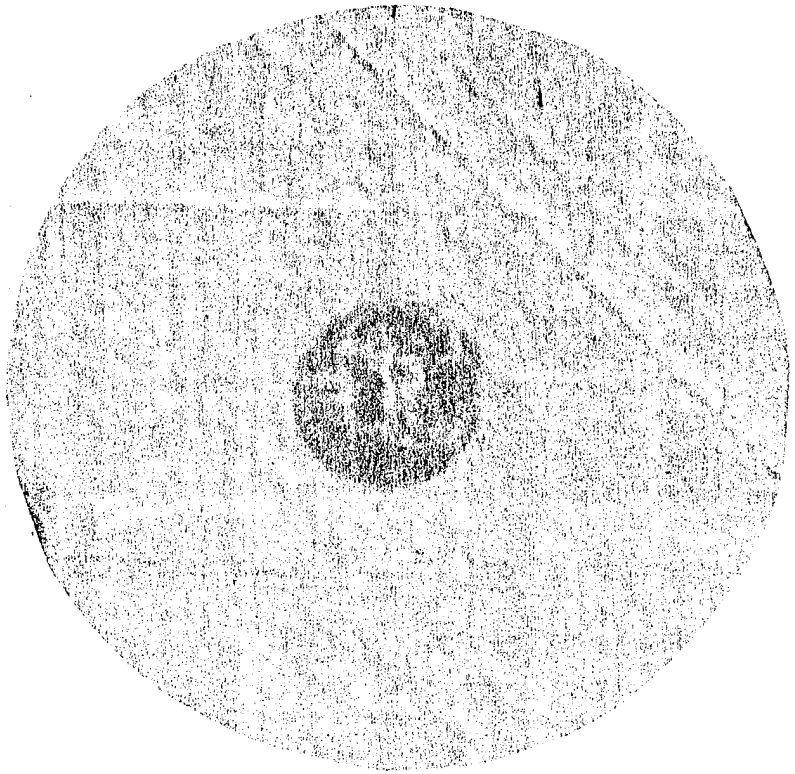

Scan of the loaded side of the disk

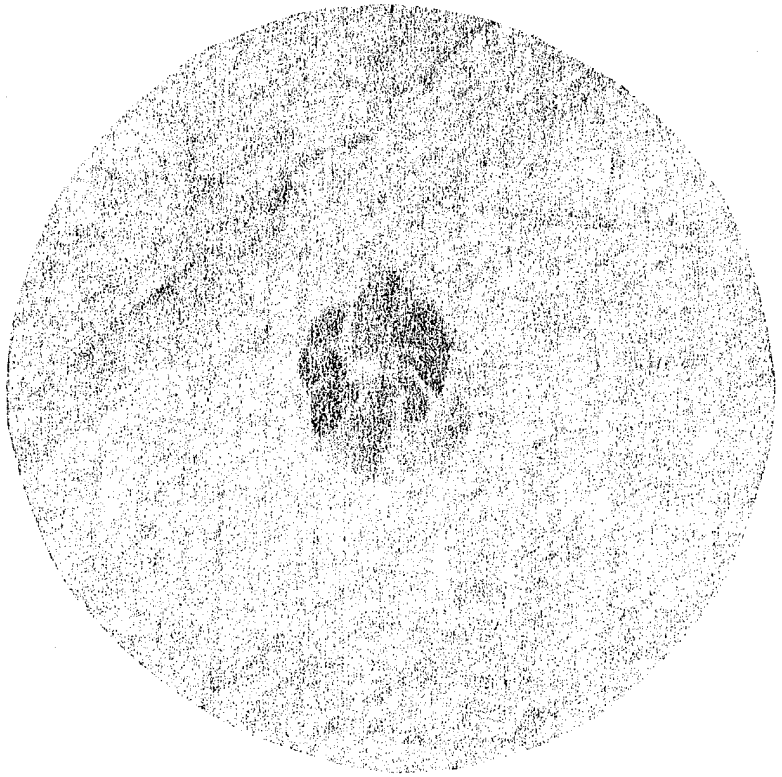

Scan of the unloaded side of the disk

Figure 14 Scans of Disk 124 After 10,000 Fatigue Cycles

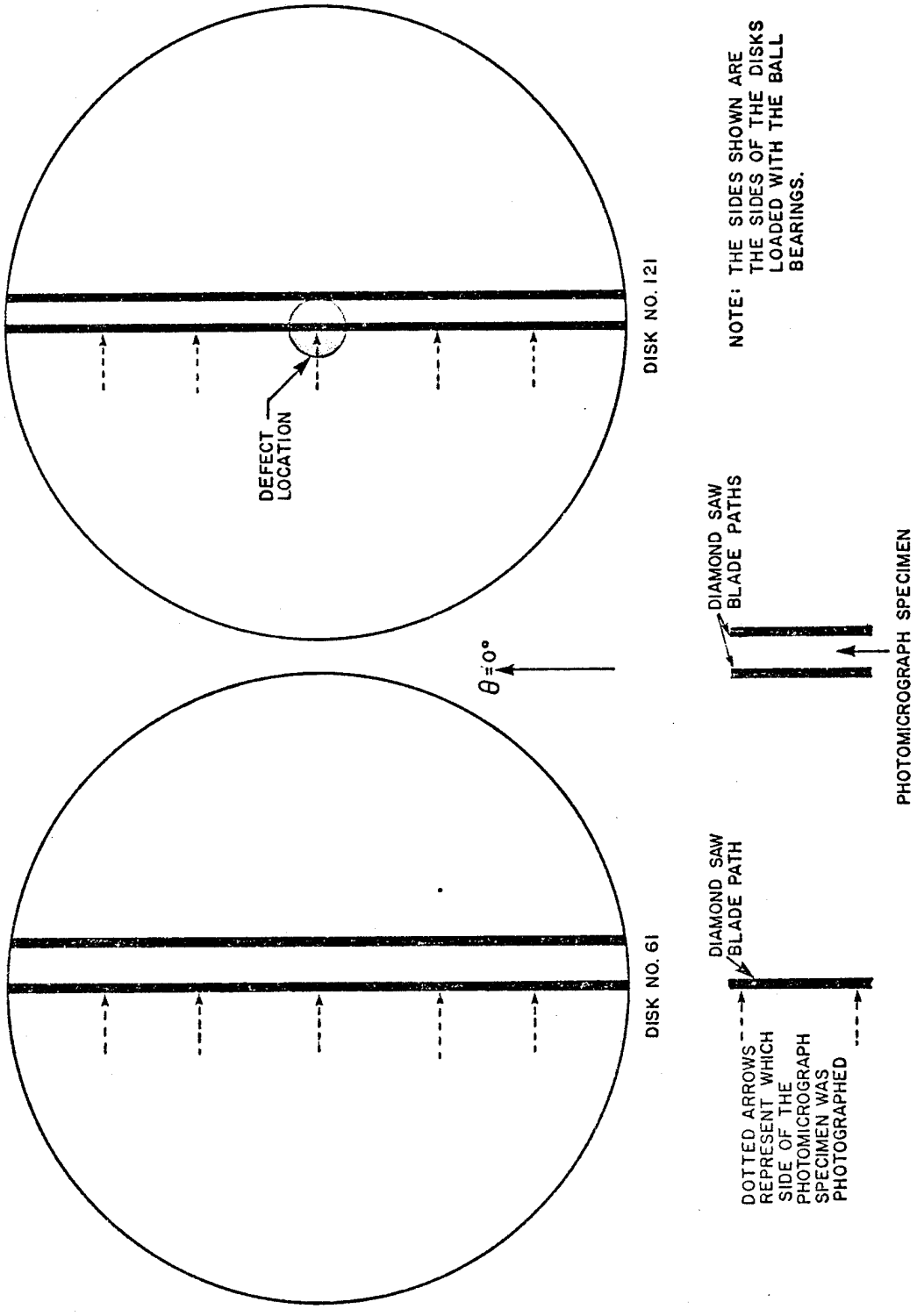

Figure 15 Photomicrograph Specimens

3. The polished specimen is observed under a microscope and selected portions of the specimen are photographed.

The photomicrograph of the damaged region of disk 121 was too large to include in this report. Therefore, representation of the photomicrograph is shown in Figure 16. In this picture, the regions with long horizontal lines represent the 0^{o} laminae, the small cross-hatched area in the center of the picture represents the implanted defect, and the remaining black lines represent cracks and delaminations in the disk. Two things should be noted. First of all, the implanted defect did propagate under the loading. Therefore, it is safe to assume that other implanted defects also grew. The second item to be noted is that may of the cracks and delaminations in the disk occur at ply interfaces. This interlaminar damage is well shown by the cracks and delaminations labeled "A".

To correlate the interlaminar damage shown by the photomicrograph to the "lobe-like" patterns shown on the ultrasonic scans, a combination of scanning techniques "A" and "C" were used. First of all, an overall view of the damage from one side of the disk was made using scanning technique "A" (see Figure 17, left). After the scan was made, the transducer was placed over a "lobe-like" pattern. The resulting waveform in the oscilloscope showed the waveform of the delamination that produced the "lobe-like" pattern on the scan. Using scanning technique "C", the delamination was "captured" on a scan. This process was repeated for each of the "lobe-like" patterns. Before the transducer was moved to a different lobe pattern, however, the delamination waveform was photographed. After scanning one side of the disk, the entire procedure was repeated for the other side of the disk.

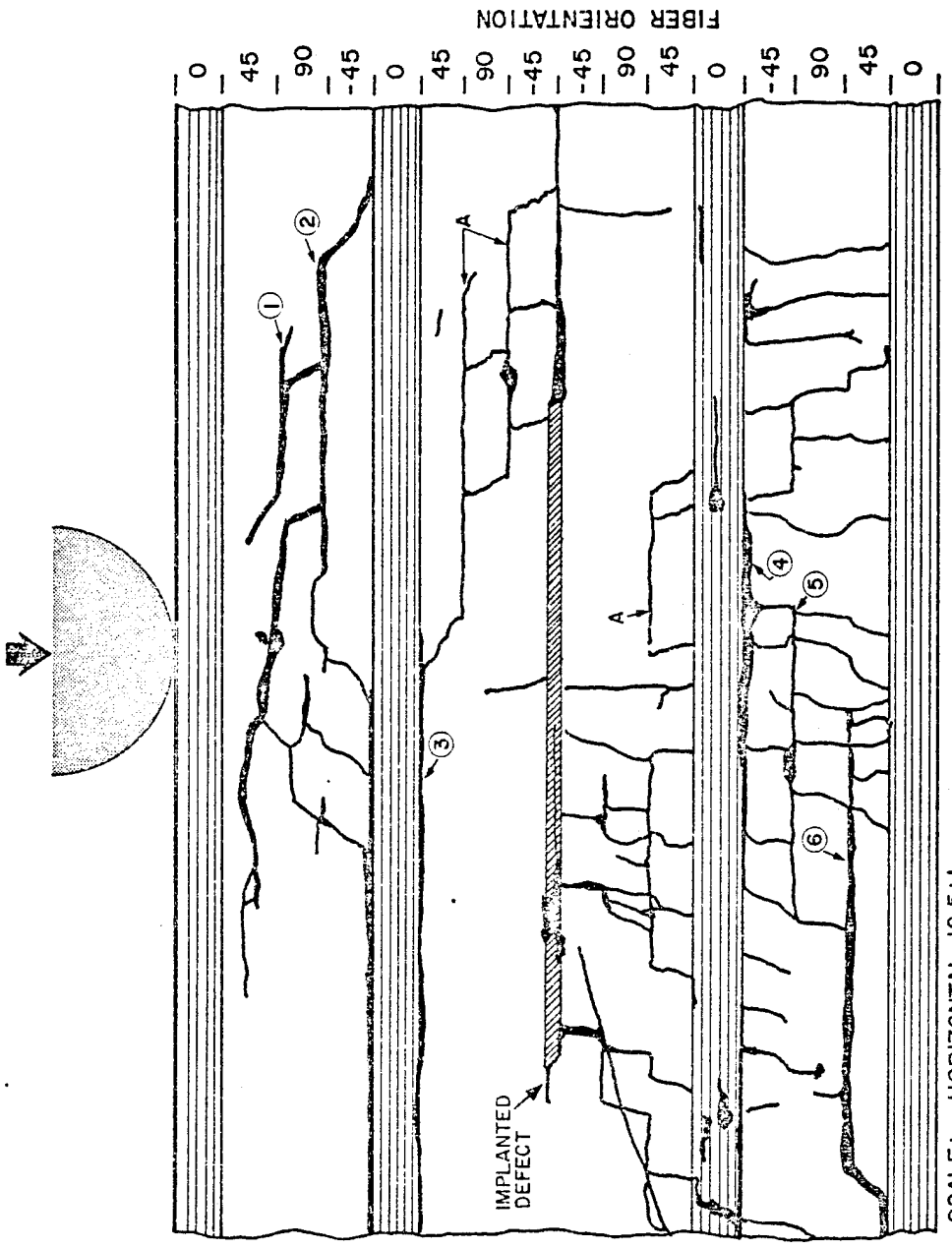

Figure 16 A Representation of the Photomicrograph of Disk 121

Using the resulting scans (see Figures 17, 18, 19, and 20) and the photographed waveforms, a composite picture of the damage in the disk was made. This picture is drawn in Figure 21.

To determine the depth at which each delamination occured in the disk, the gate setting used to scan the delamination was employed. The distance between the front surface reflection and the back surface reflection was 0.134 inches (the thickness of the plate) which corresponds to a time interval of 2.2 μ sec. The gate delay time (i.e. the gate setting shown) is also known so the depth at which each of the delaminations occur ban be calculated. Knowing these depths and the line along which the photomicorgraph was taken (the side of the disk that the photomicrograph depicts can be seen in Figure 15) a comparison between the damage shown by the scan and the actual damage shown by the photomicrograph can be made. This comparison is shown in the following chart:

Table 3 A Comparison for Disk 121

Disk Letter	Gate Delay (μ sec)	Corresponding Depth (Inches)	Corresponding Ply Interface	Delamination Label on Photomicrograph
A	.26	.016	2- 3	1
B	.42	.026	3- 4	2
C	.68	.041	5- 6	3
E	1.68	.102	12-13	4
F	1.83	.112	13-14	5
G	1.94	.118	14-15	6

The results of the comparison are very good. The damage predicted by the scans was verified by the photomicrograph.

Before discussing the results of the Fatigue I Phase, two items should be noted about the Fatigue II Phase. First, the scan in Figure

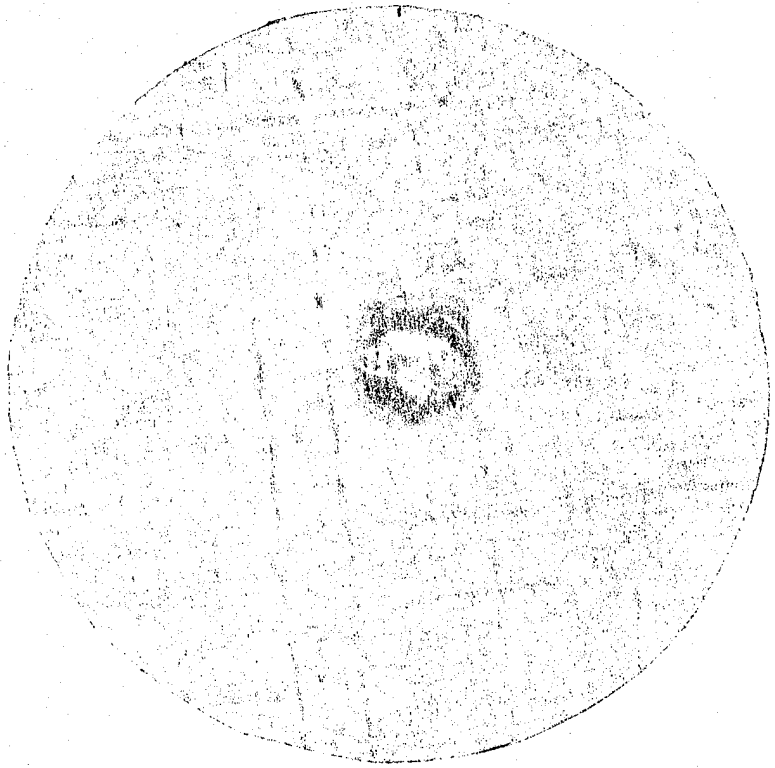

Scan of the loaded side of the disk

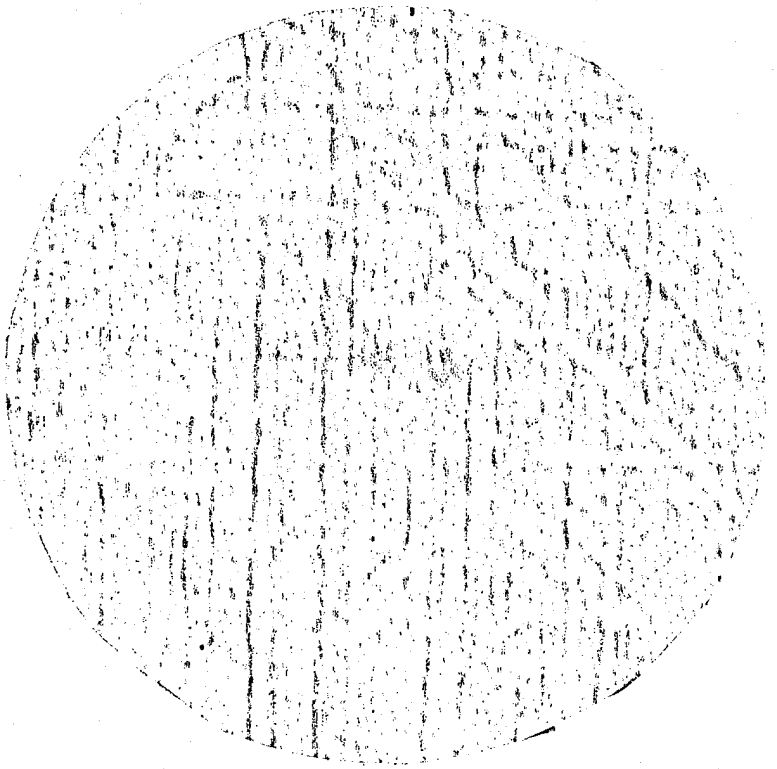

(A)

Figure 17 Scans of Delaminations in Disk 121

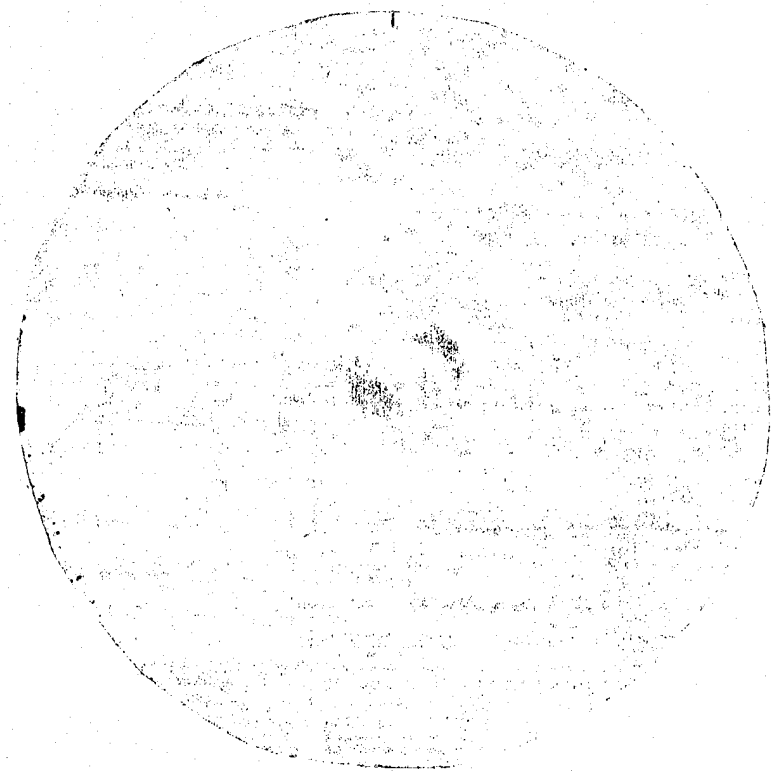

(B)

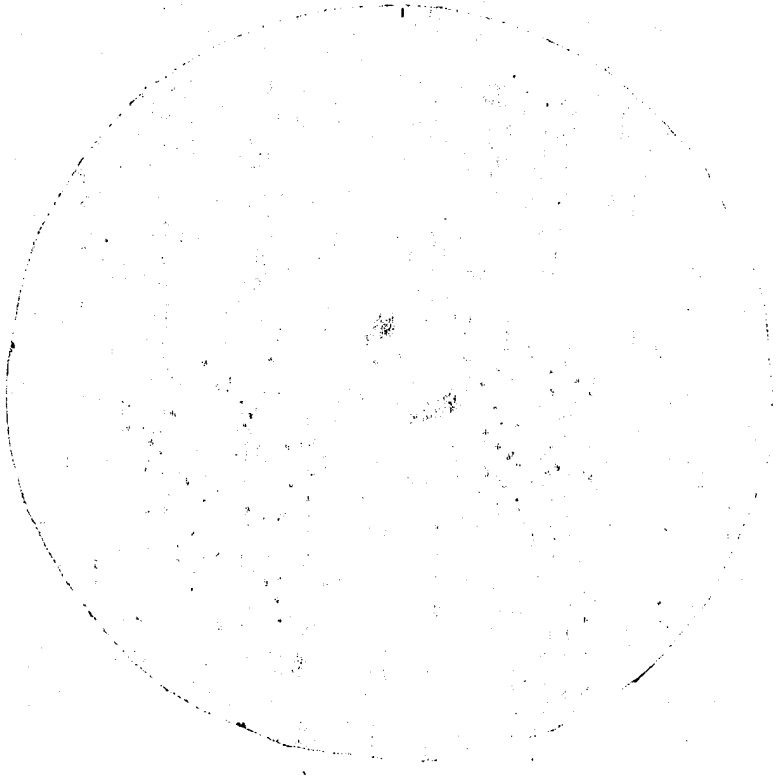

(C)

Figure 18 Scans of Delaminations in Disk 121

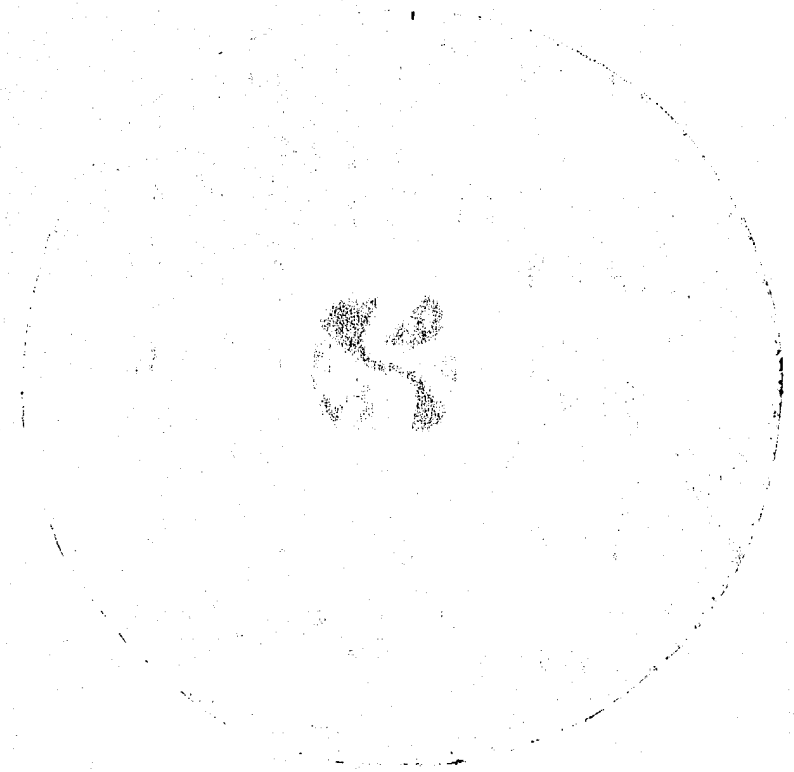

(E)

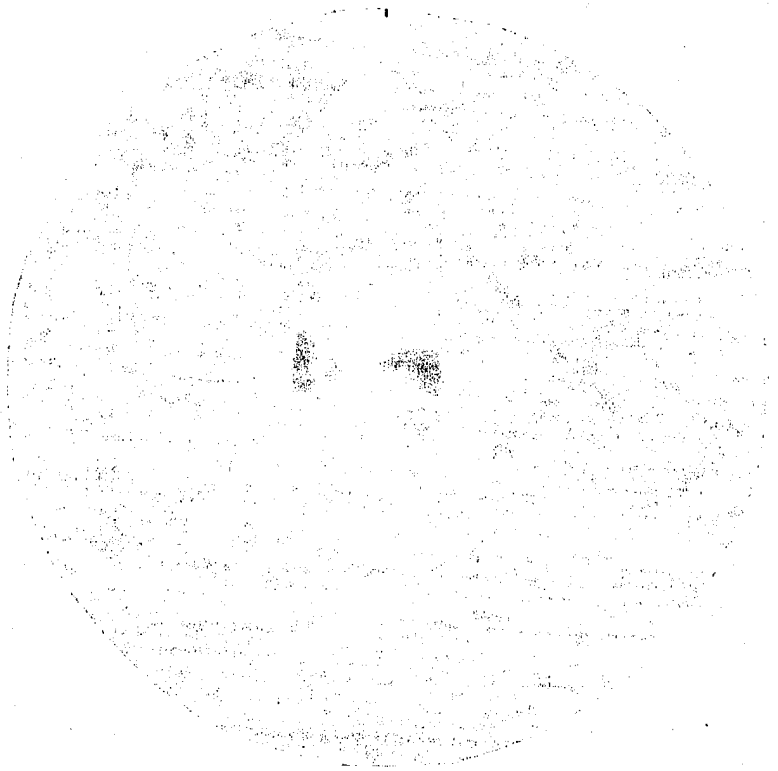

(F)

Figure 19 Scans of Delaminations in Disk 121

(G)

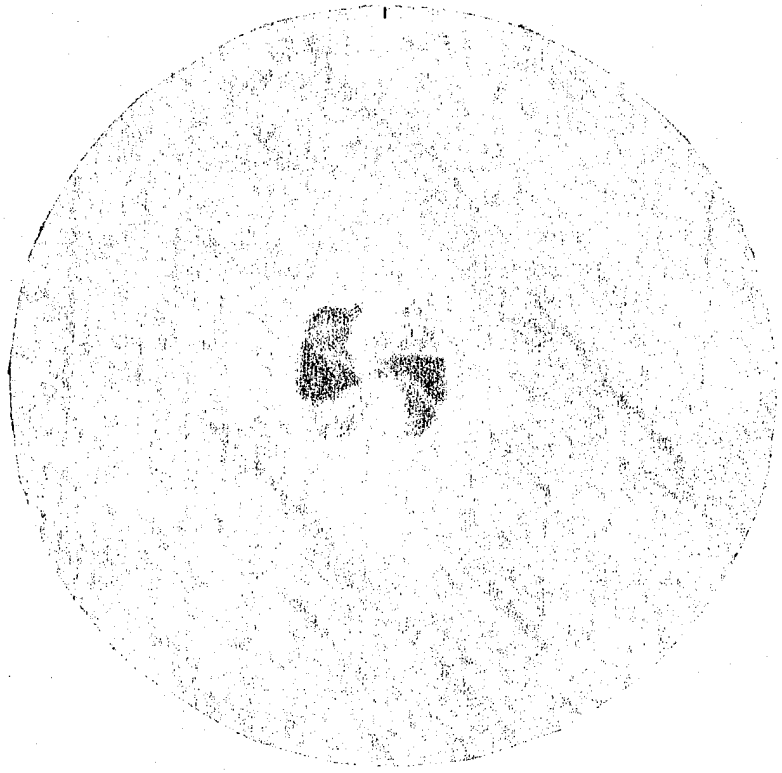

Scan of the unloaded side of the disk

Figure 20 Scans of Delaminations in Disk 121

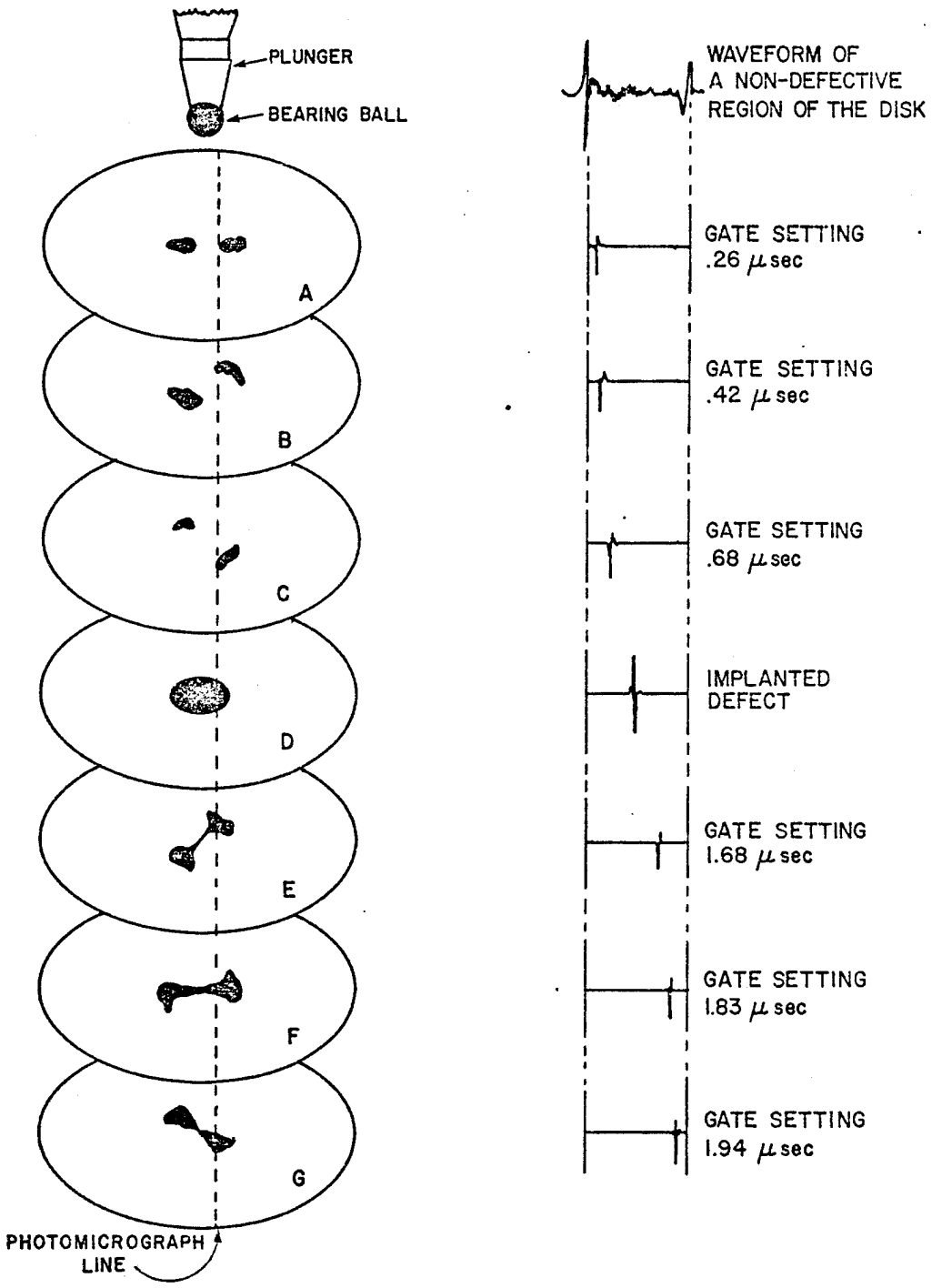

Figure 21 A Drawing of the Damage in Disk 121

19 (E) shows a scan of the second multiple of another delamination. The actual delamination is the darker pair of lobes, while the lighter pair of lobes are the second multiple of another delamination closer to the back surface.

The scan in Figure 17 (A) shows the effects of scanning a delamination that lies near the surface of a disk. The texture of the surface of the disk, as well as, the delamination appear in the resuling scan.

The scans from the Fatigue I Phase are shown in Figures 22, 23, 24, and 25. These scans were taken after 50,000 cumulative cycles of fatigue loading. Once again, the overall damage for each type of disk was approximately the same and the damaged area formed "lobe-like" patterns. An interesting observation is the size of the damaged area. The damaged region of the pristine disk is approximately the same size as the damaged region of the defective disk, yet the former was subjected to 50,000 cycles while the latter, only 10,000 cycles. Thus, as one would expect, the implanted defect is shown to increase the rate of damage in the disk.

To investigate the "lobe-like" damage patterns, disk 61 (which had been loaded to 20,000 cycles) was subjected to the type of analysis discussed previously. A photomicrograph was made of the disk (see Figure 15) and the resulting representation is shown in Figure 26. Individual scans of the "lobe-like" delaminations were made and can be found in Figures 27, 28, 29, and 30. Using these scans and the photographed waveforms, a composite picture of the damage in the disk was made. This picture is drawn in Figure 31. The depth at wich each delamination occurs in the disk was determined and compared to the depth of the delaminations shown in the

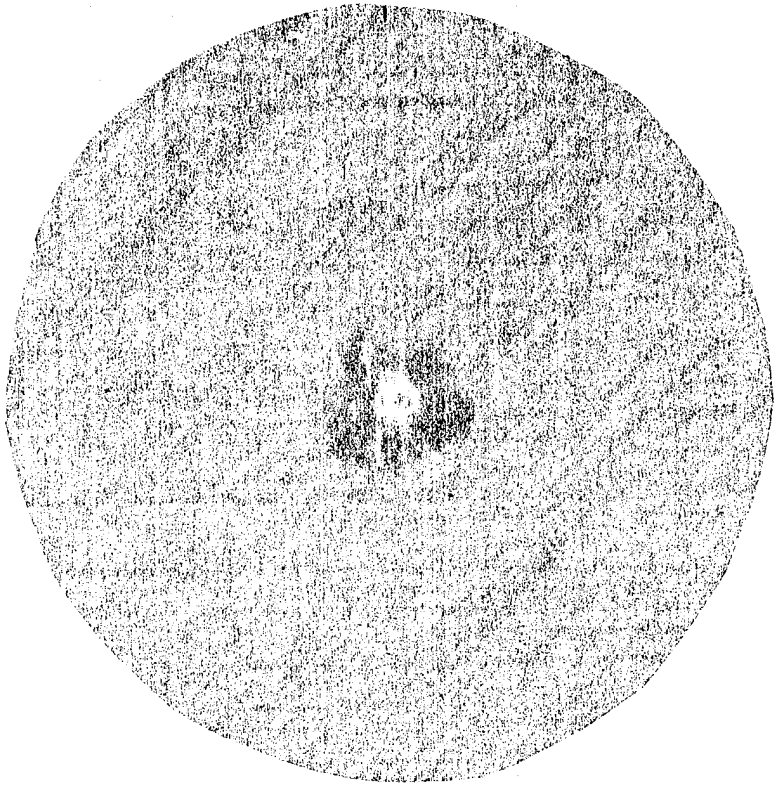

Scan of Disk 51 After 50,000 Fatigue Cycles

Figure 22

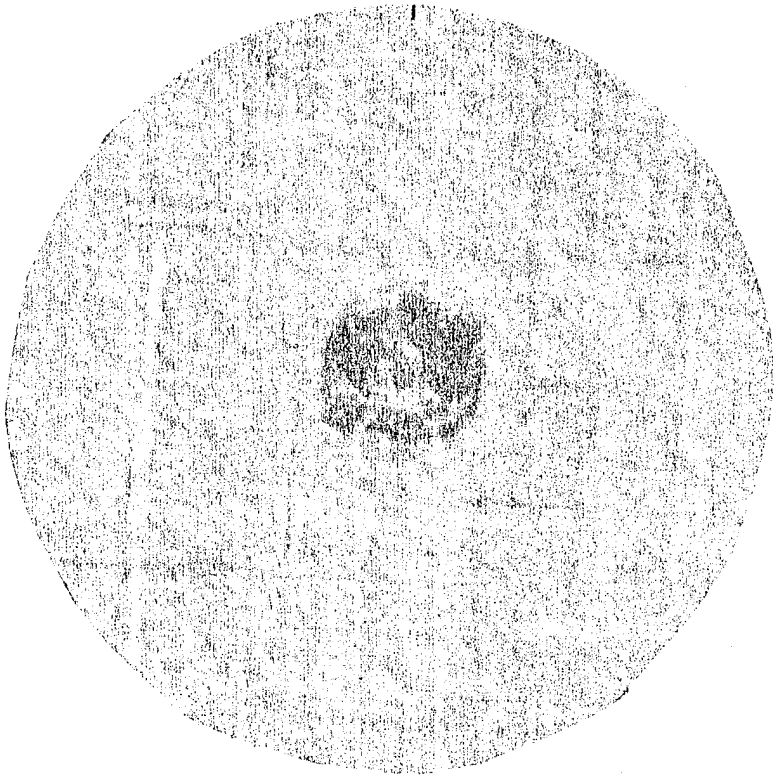

Scan of Disk 62 After 50,000 Fatigue Cycles

Figure 23

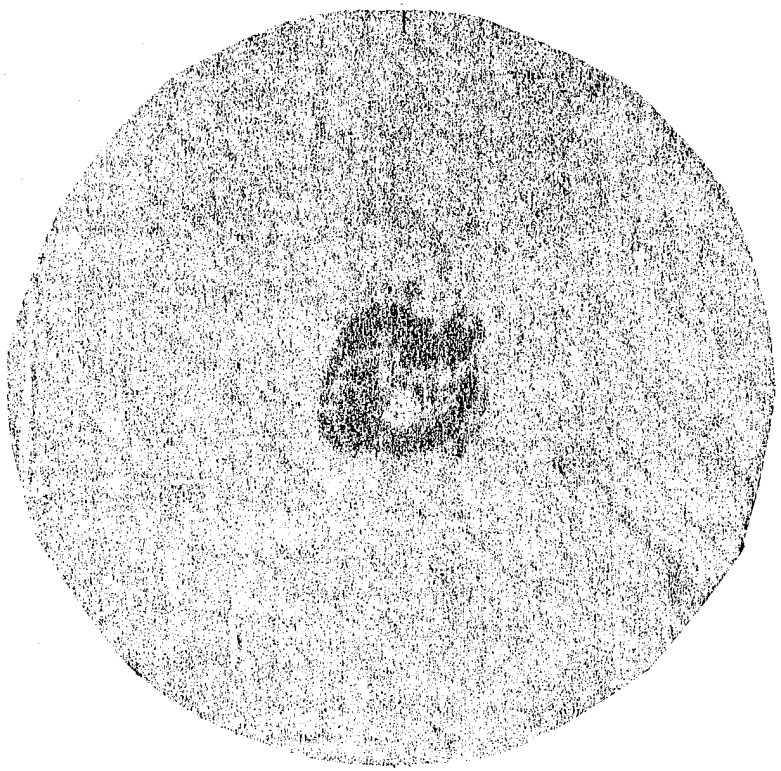

Scan of Disk 63 After 50,000 Fatigue Cycles

Figure 24

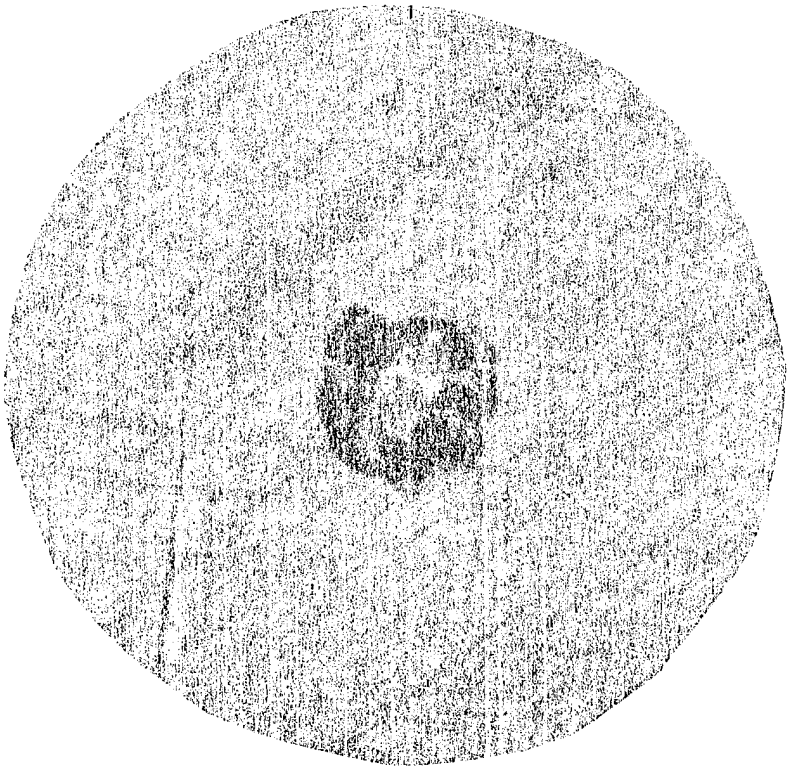

Scan of Disk 74 After 50,000 Fatigue Cycles

Figure 25

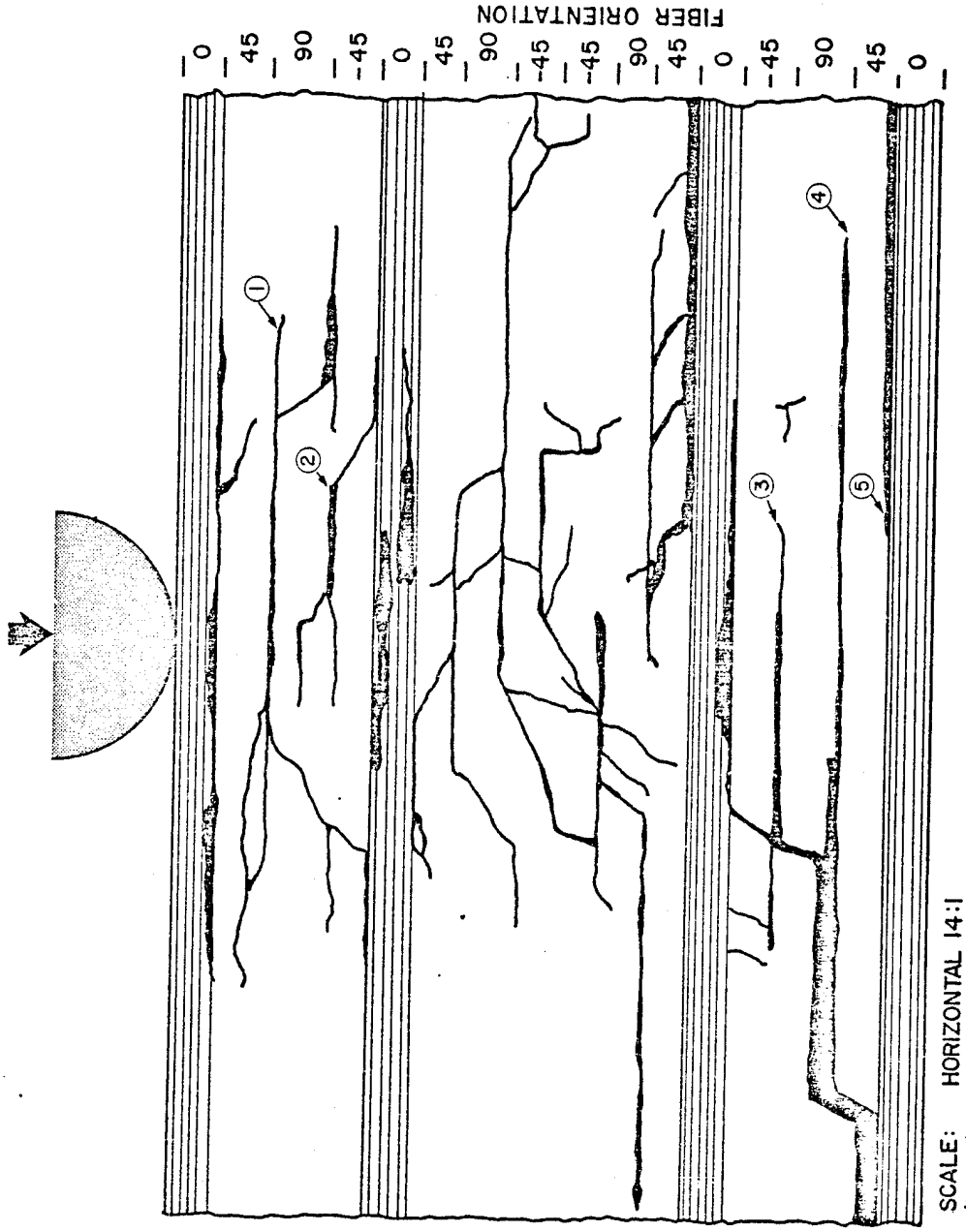

Figure 26 A Representation of the Photomicrograph of Disk 61

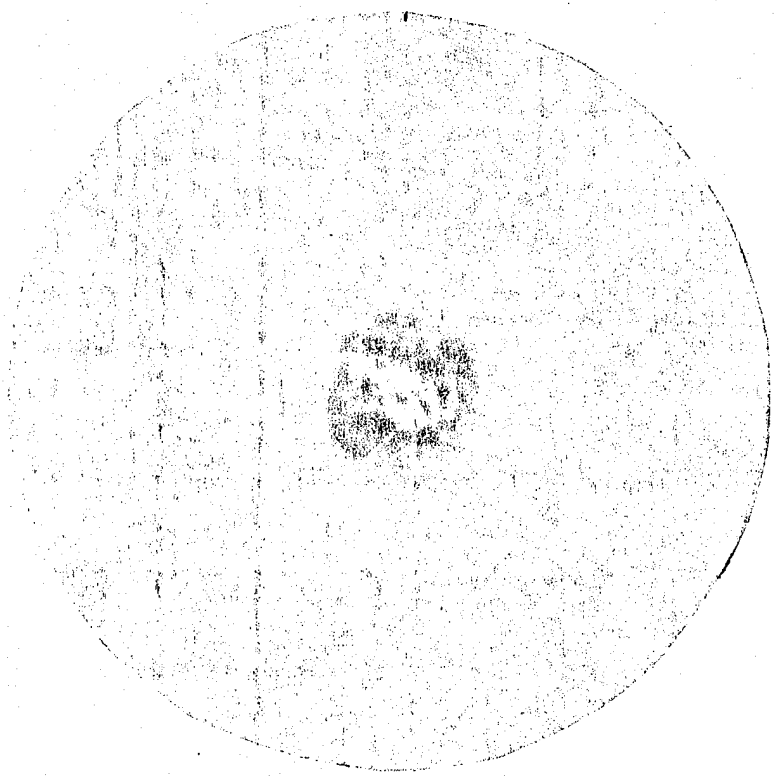

Scan of the loaded side of the disk

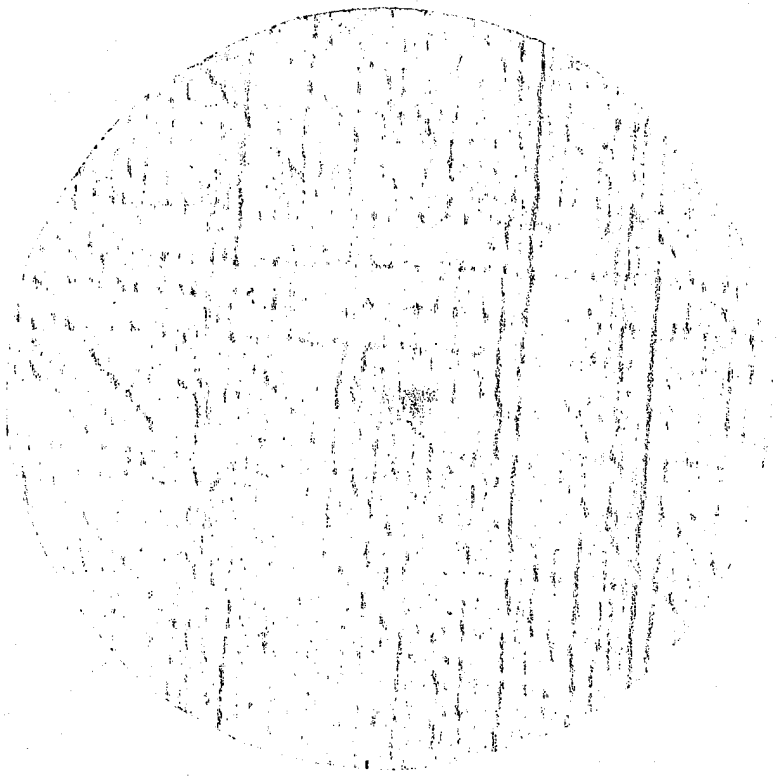

(A)

Figure 27 Scans of Delaminations in Disk 61

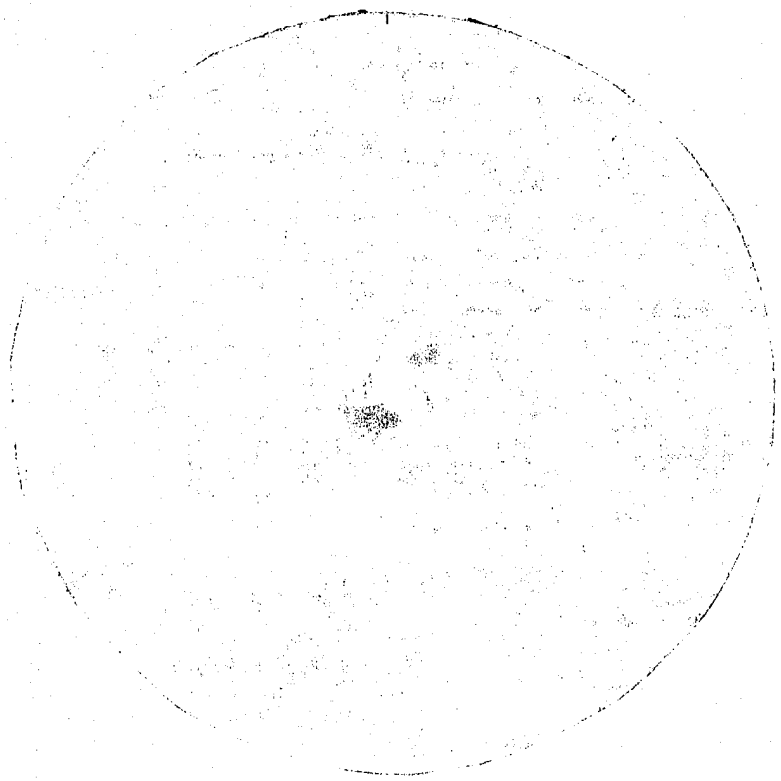

(B)

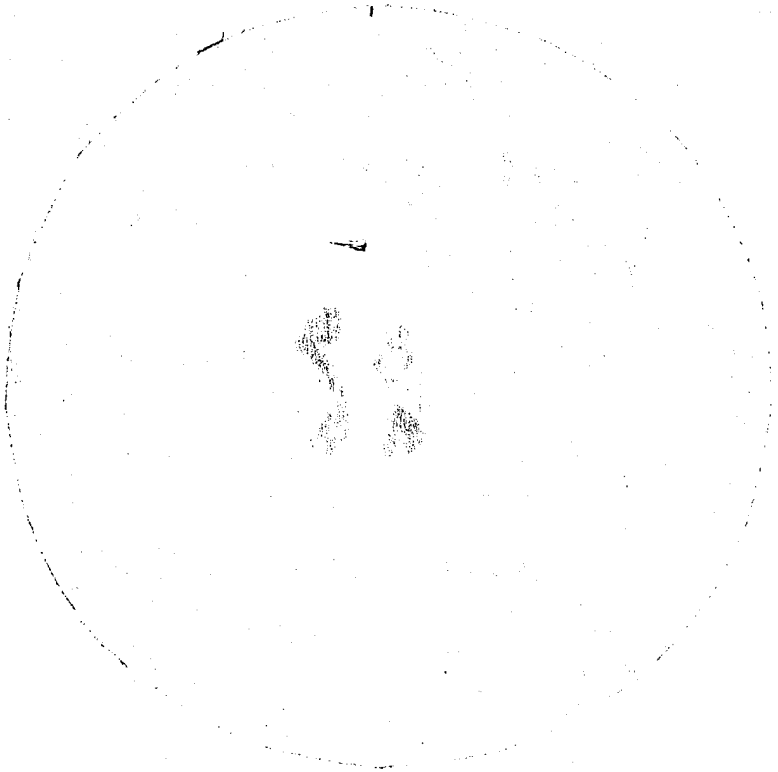

(C)

Figure 28 Scans of Delaminations in Disk 61

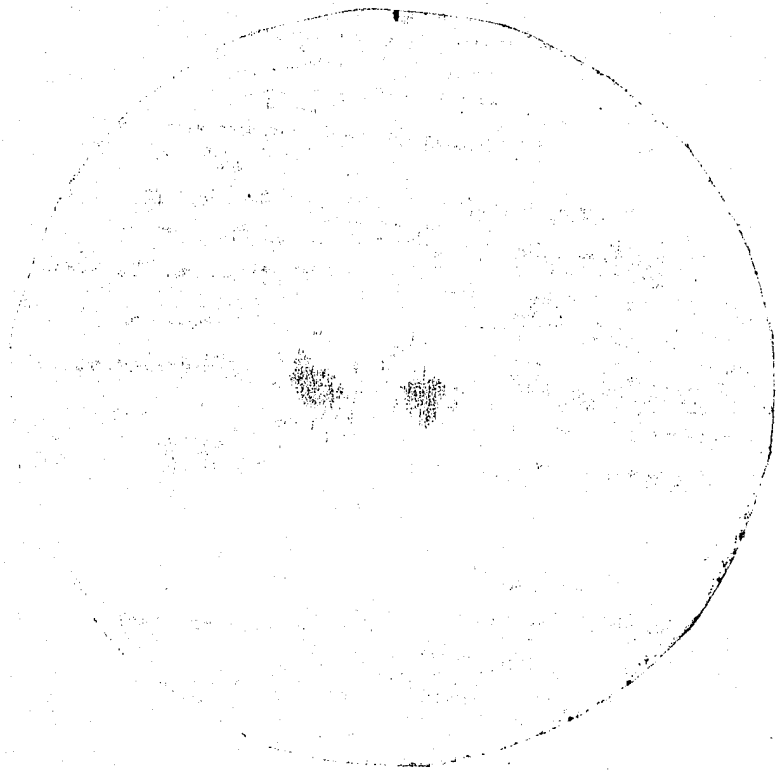

(D)

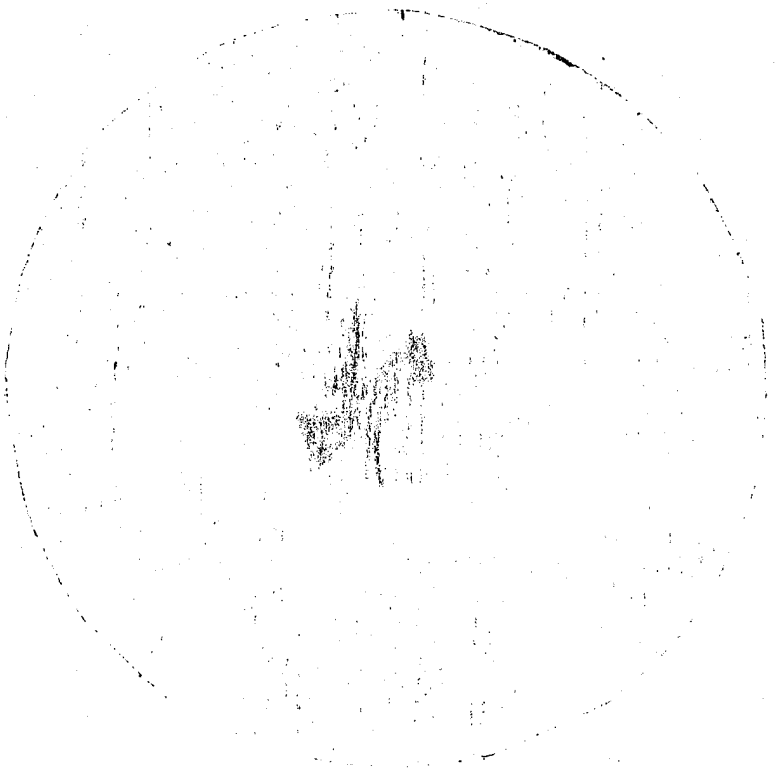

(E)

Figure 29 Scans of Delaminations in Disk 61

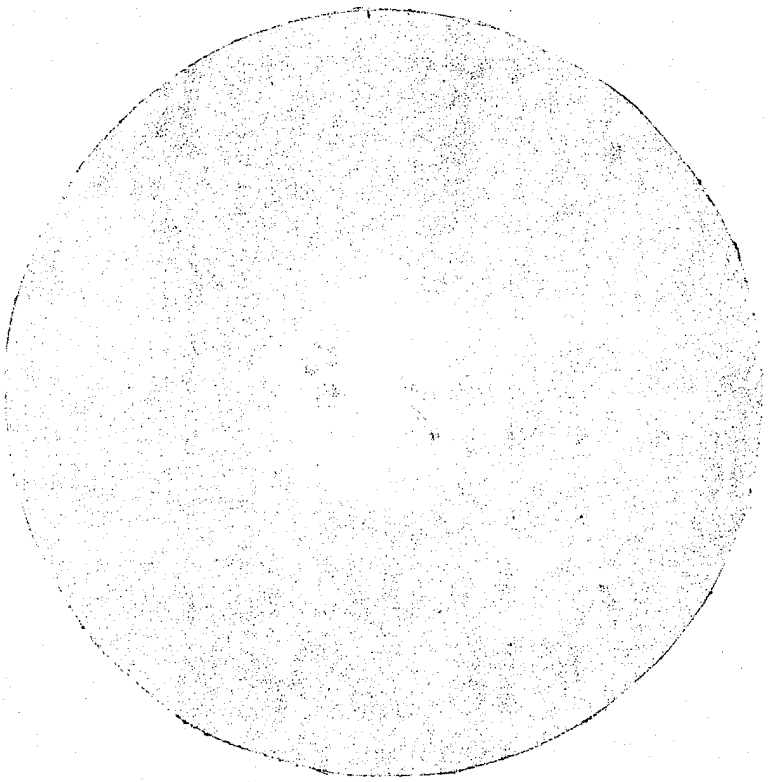

Scan of the unloaded side of the disk

Figure 30 Scan of the Delaminations in Disk 61

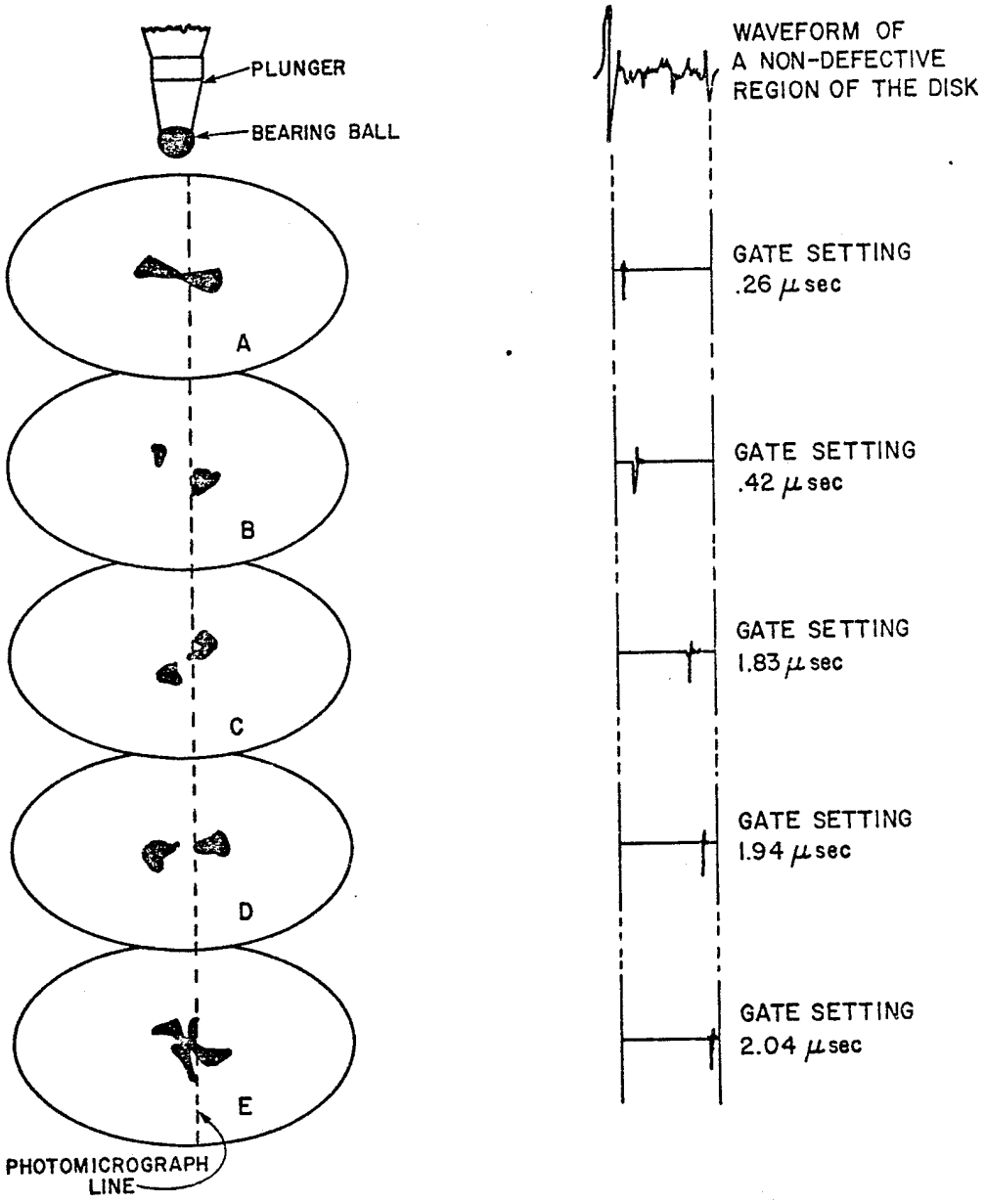

Figure 31 A Drawing of the Damage in Disk 61

photomicrograph. This comparison is shown in the following table:

Table 4 A Comparison for Disk 61

Disk Letter	Gate Delay (μsec)	Corresponding Depth (Inches)	Corresponding Ply Interface	Delamination Label on Photomicrograph
A	.26	.016	2- 3	1
B	.42	.026	3- 4	2
C	1.83	.112	13-14	3
D	1.94	.118	14-15	4
E	2.04	.124	15-16	5

As before, the results of the comparison are very good. The damage predicted by the scans was verified by the photomicrograph.

The scan in Figure 27 (left) shows an overall view of the damage (scanning technique "C") from the loaded side of the disk. The scan in Figure 30 shows an overall view of the damage from the unloaded side of the disk. Here, the delamination lobes appear white because the peak polarity was positive. As was stated before, the texture of the surface of a disk, as well as, the delamination appear in a scan of a delamination that lies near a surface of the disk. Figure 27 (A) shows this effect. Second multiples of another delamination are shown in Figure 28 (C) . The dark pair of lobes are the original delamination while the lighter pair of lobes are the second multiple of another delamination closer to the surface of the disk.

The scans in Figures 32, 33, 34, 35, and 36 are of the pristine disk 63 at various fatigue loading cycles. The scans show how the overall damage of the disk increases as the number of fatigue cycles also increases.

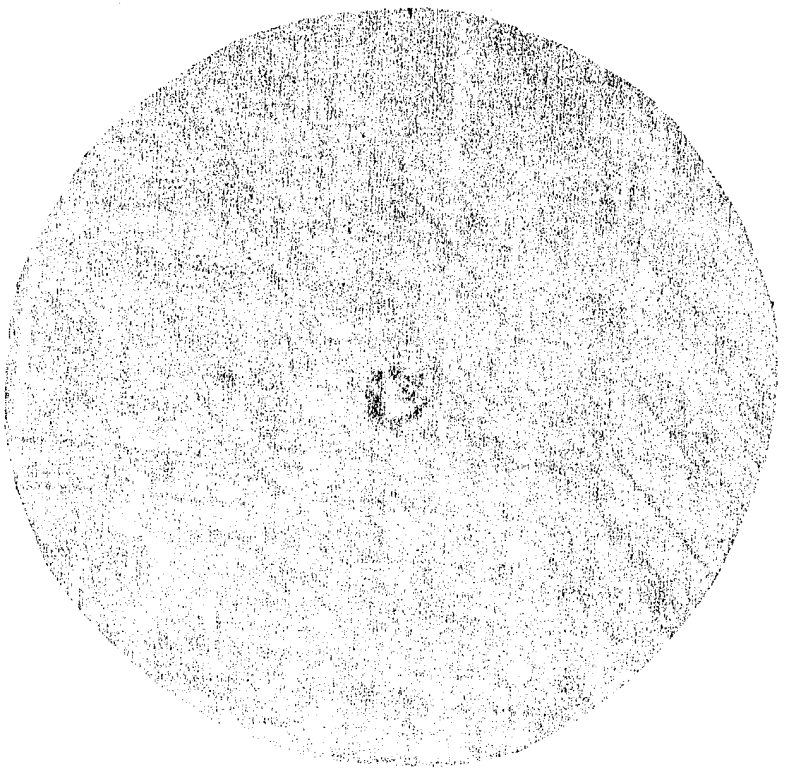

1000 cycles

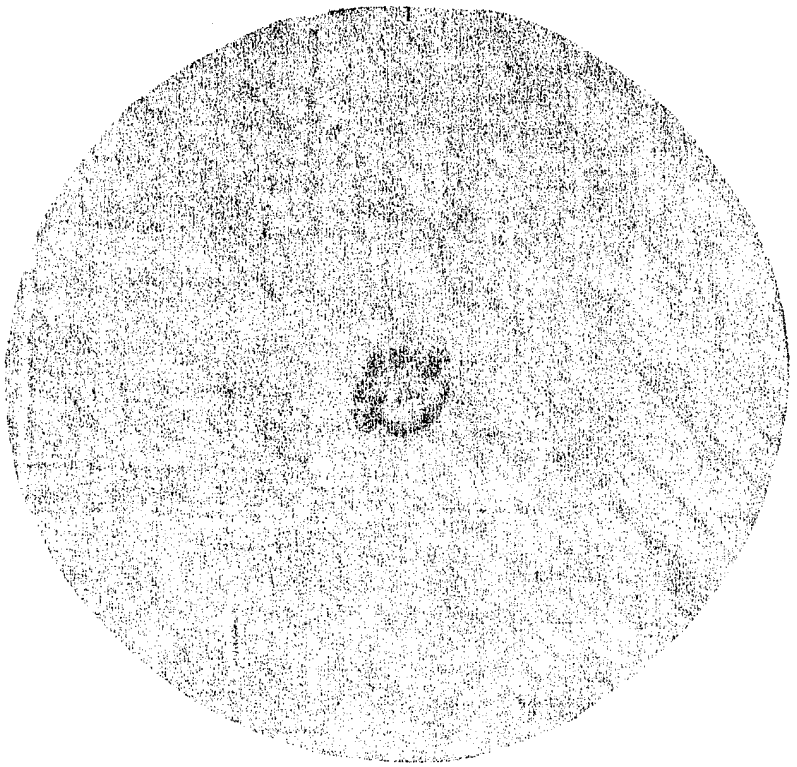

2500 cycles

Figure 32 Scans of Disk 63

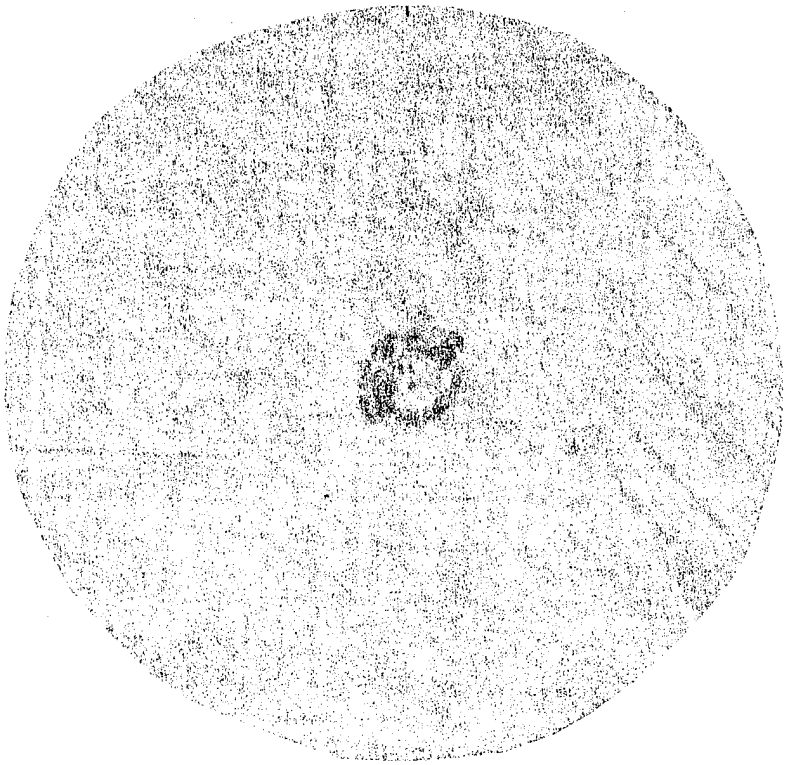

3750 cycles

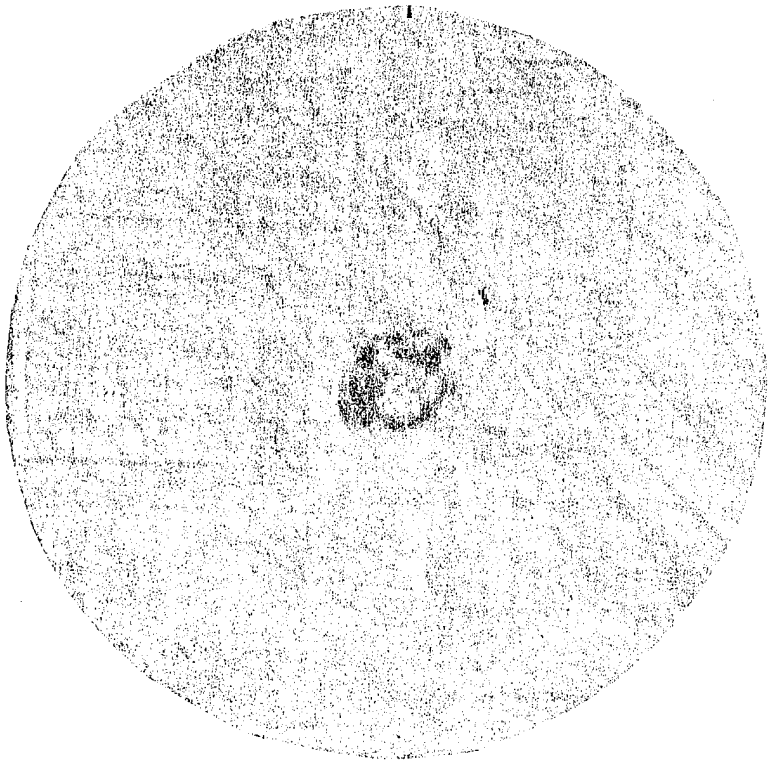

5000 cycles

Figure 33 Scans of Disk 63

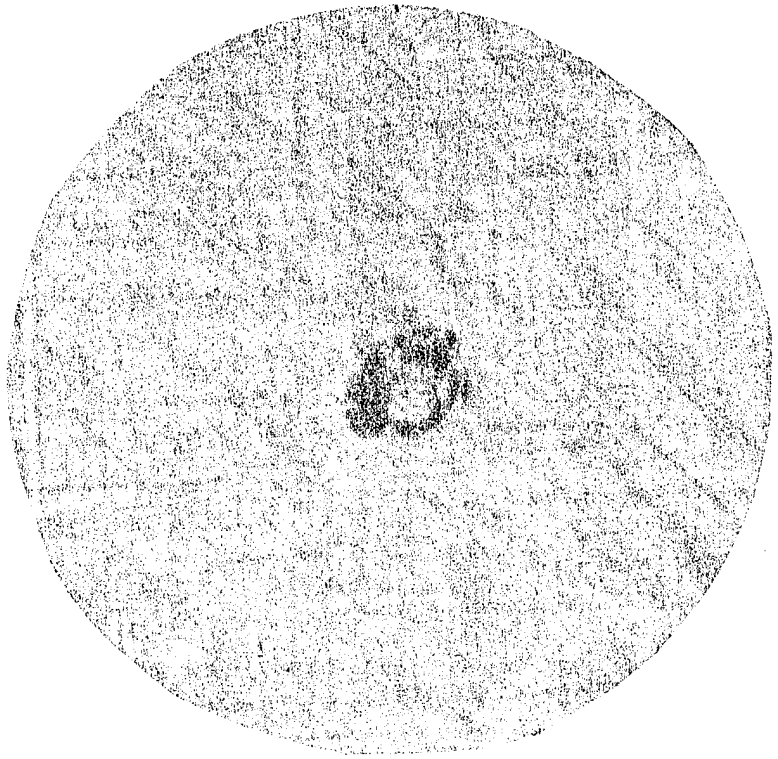

7500 cycles

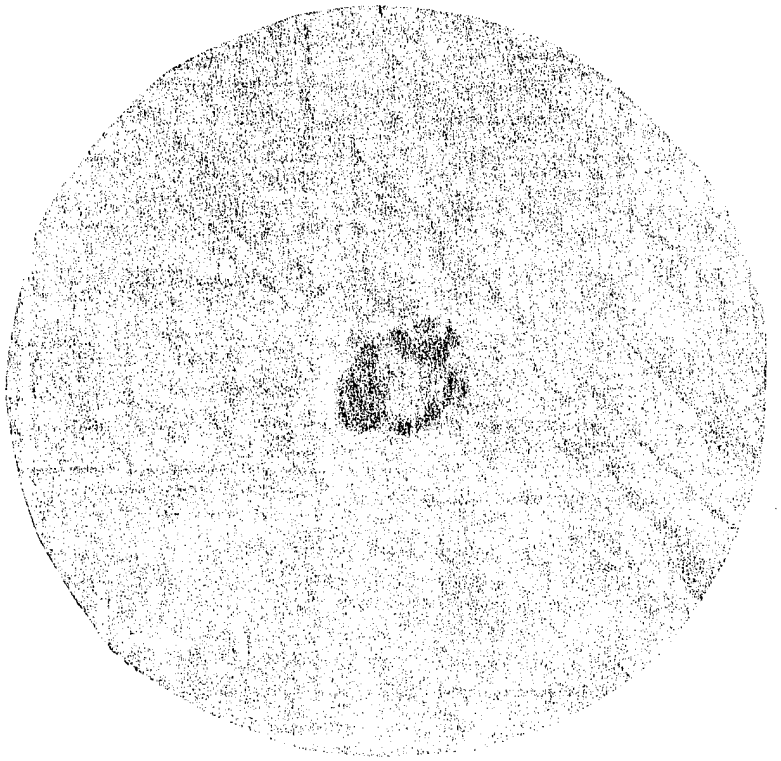

10000 cycles

Figure 34 Scans of Disk 63

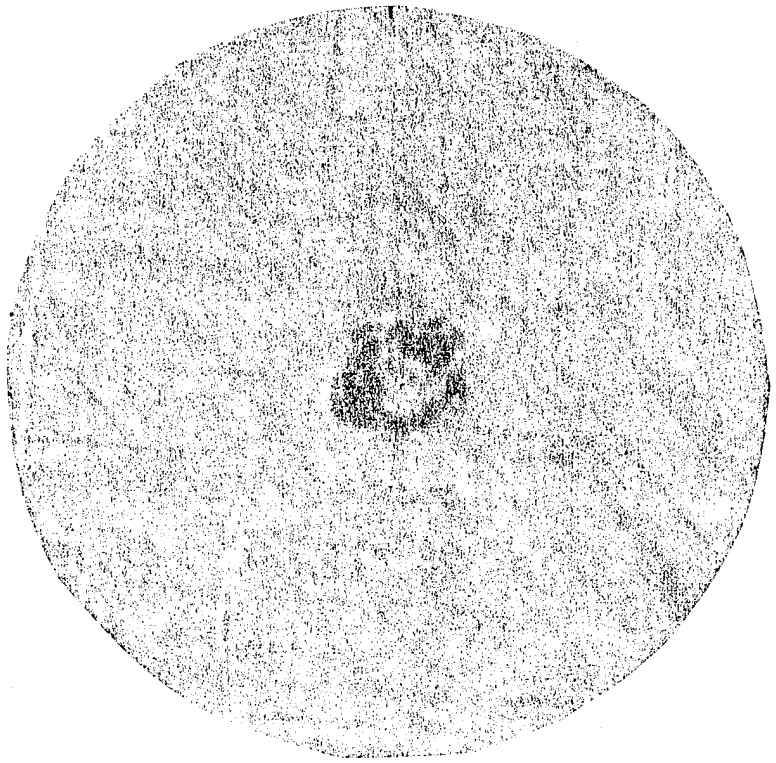

15000 cycles

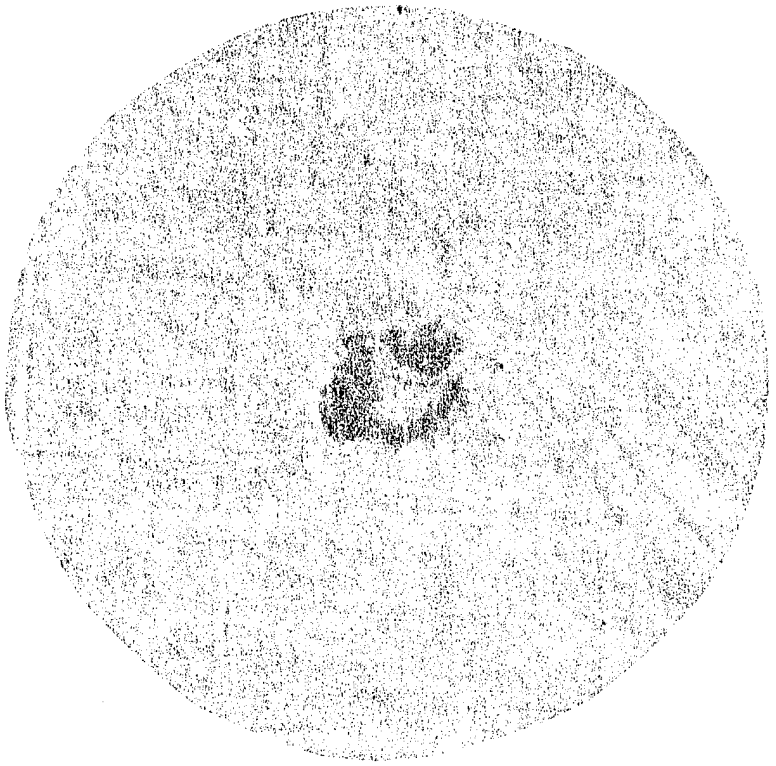

20000 cycles

Figure 35 Scans of Disk 63

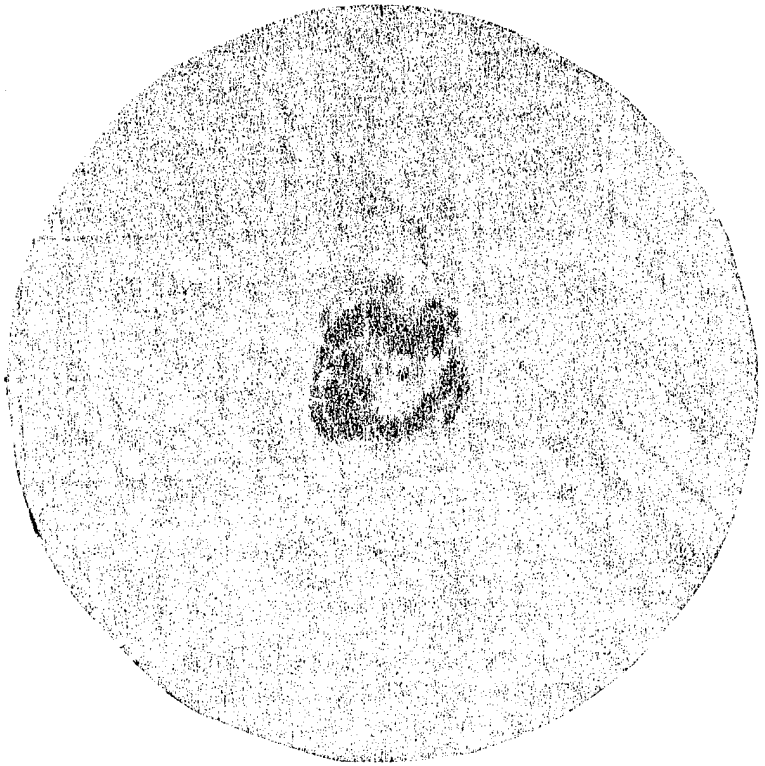

30000 cycles

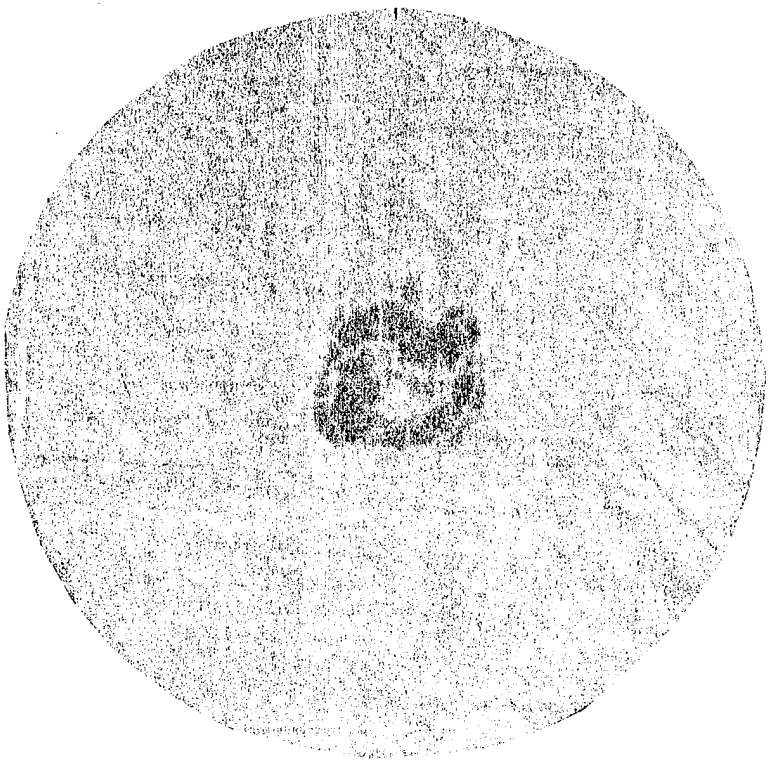

40000 cycles

Figure 36 Scans of Disk 63

IV. A Finite-Element Model of a Pristine Disk

A finite-element model of a pristine disk was developed using the finite-element program SAP V. The finite-element mesh consisted of 385 nodes and 384 elements; one half of the mesh is shown in Figure 37. A quadrilateral plate and shell element was used in the analysis. This element allows material properties to be entered as isotropic or orthotropic. In addition, properties may be specified as the stiffness matrix, Q relating stress and strain. The latter option was chosen because the stiffness of the plate is a function of orientation (θ) and this was incorporated through Q. Theta is defined in Figure 38.

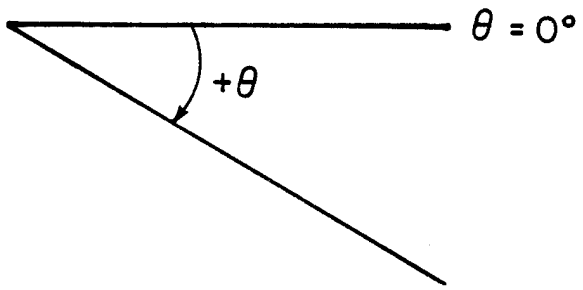

Figure 38 Definition of Theta

To find the stiffness matrix as a function of the angle θ, several steps were required. To begin with, a laminate analysis program was used to calculate the laminate matrices A, B, and D as a function of θ. A is

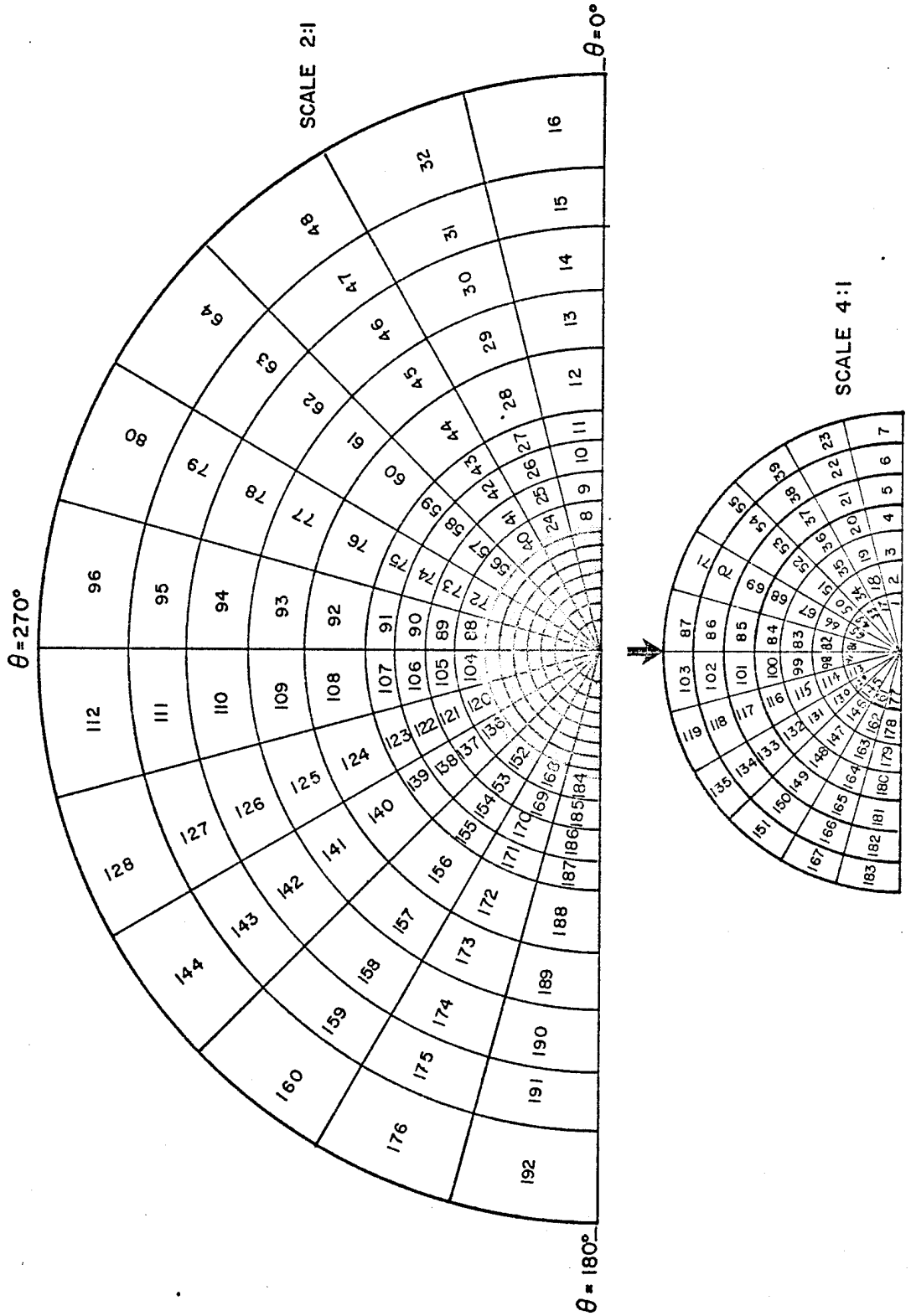

Figure 37 One Half of the Finite-Element Mesh

the extensional stiffness matrix, B is the bending-stretching coupling matrix, and D is the flexural stiffness matrix. The first stacking sequence entered was $[0/45/90/-45]_{2S}$, the disk orientation, which corresponds to $\theta = 0^{o}$. Note that when $\theta = 5^{o}$, the original orientation of the plate appears to be $[5/50/95/-40]_{2S}$. Entering the latter orientation into the laminate analysis rotates the principal properties of the laminate to $\theta = 5^{o}$ and produces the A, B, and D matrices for the rotated coordinate system. This procedure of incrementing by 5^{o} was repeated until $\theta = 360^{o}$.

From the results, several things should be noted. First, every A and B matrix was independent of θ. The B matrix was zero due to symmetry, while $A_{16} = A_{26} = A_{61} = A_{62} = 0$ because the laminate was balanced. As for the rest of the A matrix, $A_{11} = A_{22} = 4.623$ E5 psi, $A_{12} = A_{21} = 1.423$ E5 psi and $A_{66} = 1.600$ E5 psi. The D matrix values changed with θ and repeated after π radians. Thus, the D matrix for 5^{o} was the same as the D matrix for 185^{o} (see Table 5 and Figures 39-44).

To find Ex' and Ey', where Ex' and Ey' are the Elastic moduli in the x and y directions in the rotated coordinate system respectively (see Figure 45), the following equation was used:

$$D = Eh^{3}/(12(1-\nu^{2})) \quad \ldots\ldots\ldots\ldots\ldots\ldots\ldots \quad (1)$$

where D is the flexural stiffness of the plate, E is the Elastic modulus of the plate, h is the thickness of the plate, and ν is Poisson's ratio of the plate. To calculate Ex as a function of θ (i.e. Ex'), equation (1) was used substituting in the following values for D, h, and ν -

Table 5 Flexural Stiffness Matrix Values

θ	D_{11}	D_{12}	D_{16}	D_{22}	D_{26}	D_{66}
(Degrees)	(in-lb)	(in-lb)	(in-lb)	(in-lb)	(in-lb)	(in-lb)
0	8.163E2	1.918E2	3.810E1	6.204E2	3.810E1	2.185E2
5	8.003E2	1.932E2	5.369E1	6.337E2	3.837E1	2.198E2
10	7.791E2	1.971E2	6.696E1	6.471E2	3.816E1	2.237E2
15	7.539E2	2.030E2	7.698E1	6.604E2	3.809E1	2.297E2
20	7.259E2	2.103E2	8.274E1	6.738E2	3.862E1	2.370E2
25	6.967E2	2.181E2	8.408E1	6.875E2	3.996E1	2.447E2
30	6.677E2	2.254E2	8.088E1	7.018E2	4.208E1	2.521E2
35	6.407E2	2.314E2	7.346E1	7.169E2	4.467E1	2.580E2
40	6.169E2	2.353E2	6.252E1	7.329E2	4.720E1	2.169E2
45	5.973E2	2.366E2	4.899E1	7.498E2	4.899E1	2.633E2
50	5.828E2	2.353E2	3.397E1	7.670E2	4.929E1	2.619E2
55	5.737E2	2.314E2	1.860E1	7.839E2	4.740E1	2.580E2
60	5.698E2	2.254E2	3.974E0	7.997E2	4.277E1	2.521E2
65	5.707E2	2.181E2	-9.025E0	8.134E2	3.510E1	2.447E2
70	5.758E2	2.103E2	-1.976E1	8.239E2	2.436E1	2.370E2
75	5.842E2	2.030E2	-2.790E1	8.301E2	1.090E1	2.297E2
80	5.950E2	1.971E2	-3.345E1	8.312E2	-4.650E0	2.237E2
85	6.073E2	1.932E2	-3.668E1	8.267E2	-2.135E1	2.198E2
90	6.204E2	1.918E2	-3.810E1	8.163E2	-3.810E1	2.185E2
95	6.337E2	1.932E2	-3.837E1	8.003E2	-5.369E1	2.198E2
100	6.471E2	1.971E2	-3.816E1	7.791E2	-6.696E1	2.237E2
105	6.604E2	2.030E2	-3.809E1	7.539E2	-7.689E1	2.297E2
110	6.738E2	2.103E2	-3.862E1	7.259E2	-8.274E1	2.370E2
115	6.875E2	2.181E2	-3.996E1	6.967E2	-8.408E1	2.447E2
120	7.018E2	2.254E2	-4.208E1	6.677E2	-8.088E1	2.521E2
125	7.169E2	2.314E2	-4.467E1	6.407E2	-7.346E1	2.580E2
130	7.329E2	2.353E2	-4.720E1	6.169E2	-6.252E1	2.619E2
135	7.498E2	2.366E2	-4.899E1	5.973E2	-4.899E1	2.633E2
140	7.670E2	2.353E2	-4.929E1	5.828E2	-3.397E1	2.619E2
145	7.839E2	2.314E2	-4.740E1	5.737E2	-1.860E1	2.580E2
150	7.997E2	2.254E2	-4.277E1	5.698E2	-3.974E0	2.521E2
155	8.134E2	2.181E2	-3.510E1	5.707E2	9.025E0	2.447E2
160	8.239E2	2.103E2	-2.436E1	5.758E2	1.976E1	2.370E2
165	8.301E2	2.030E2	-1.090E1	5.842E2	2.790E1	2.297E2
170	8.312E2	1.971E1	4.650E0	5.950E2	3.345E1	2.237E2
175	8.267E2	1.932E2	2.135E1	6.073E2	3.668E1	2.198E2
180	8.163E2	1.918E2	3.810E1	6.204E2	3.810E1	2.185E2

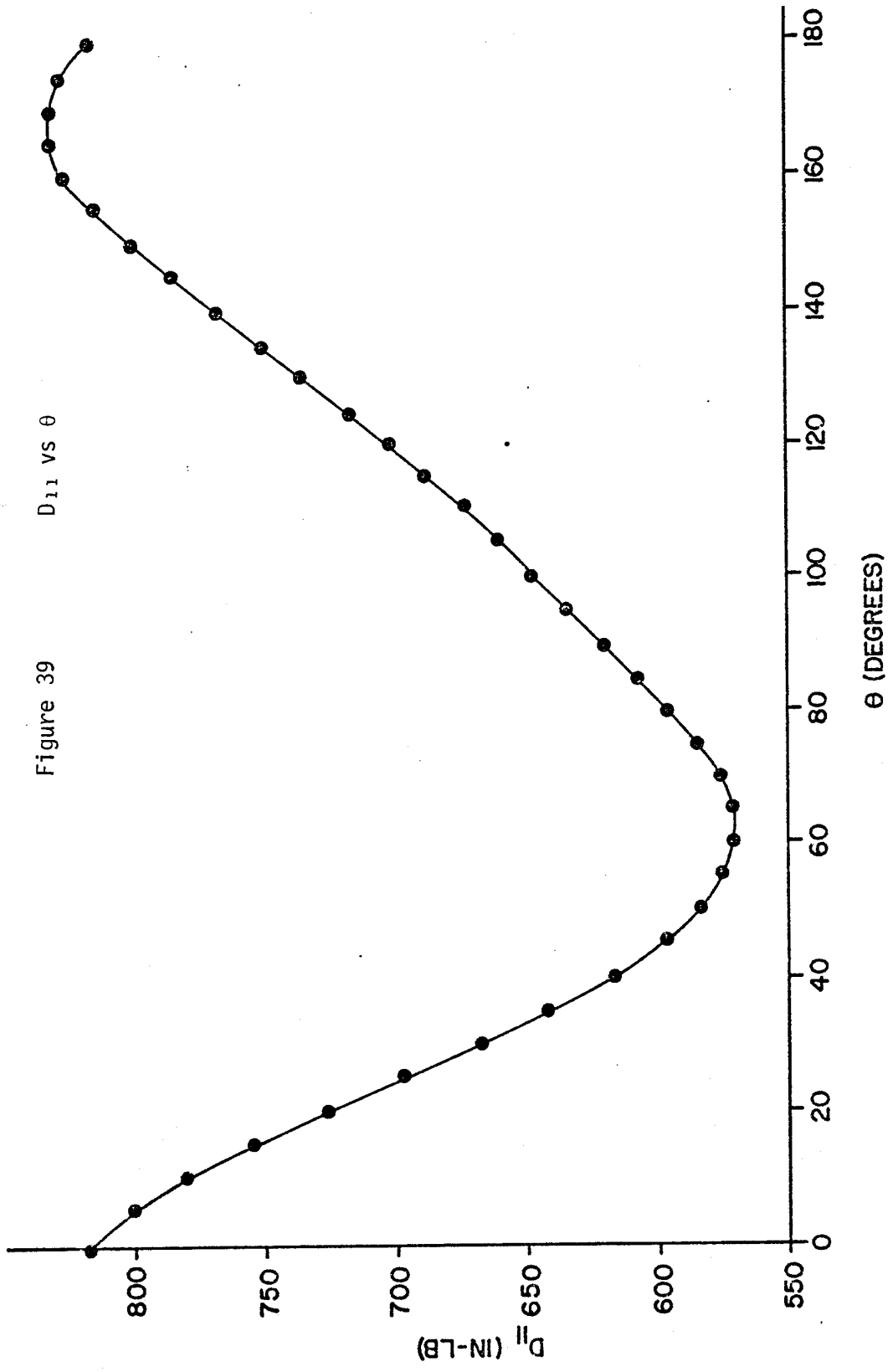

Figure 39 D_{11} vs θ

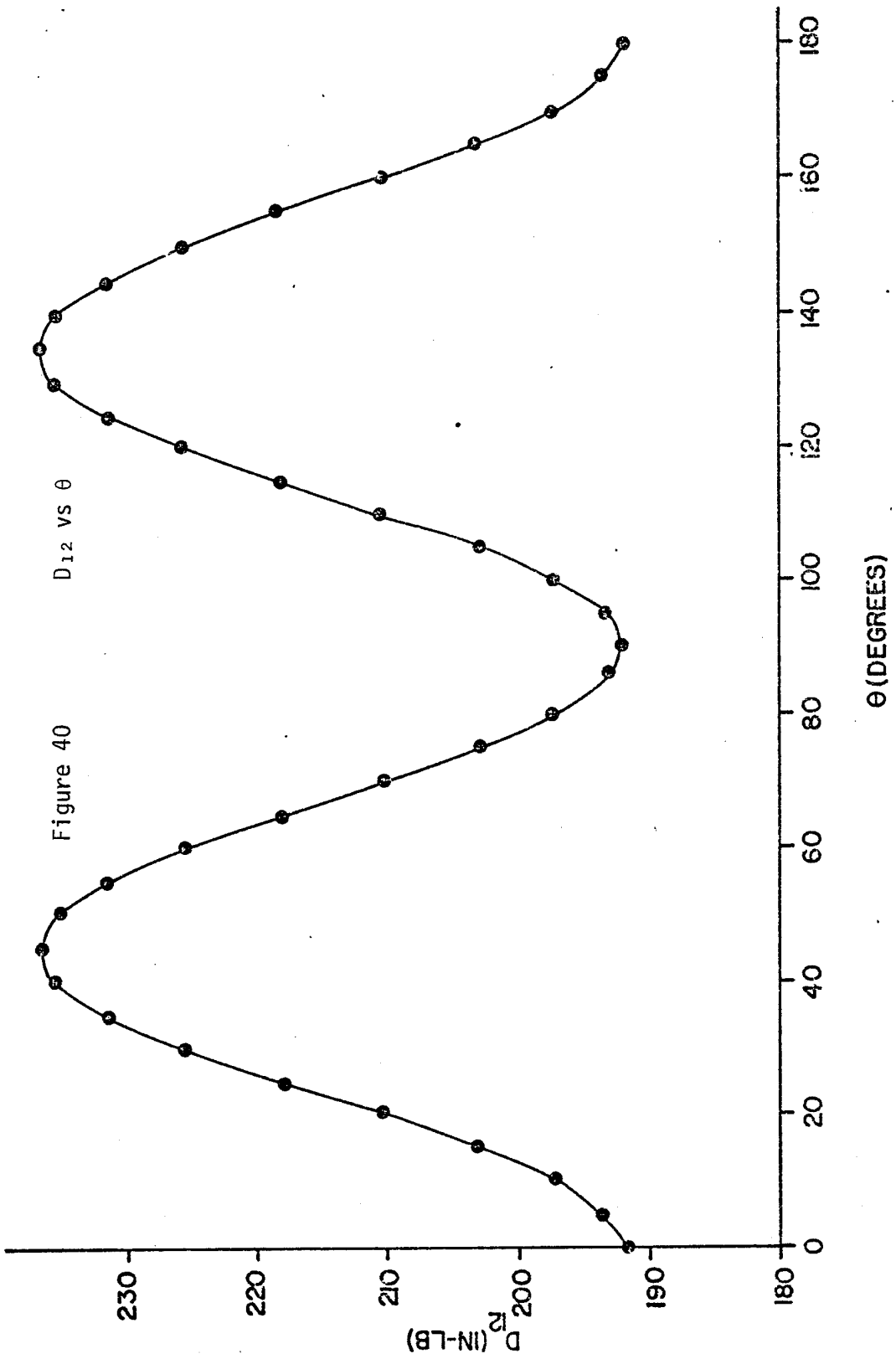

Figure 40 D_{12} vs θ

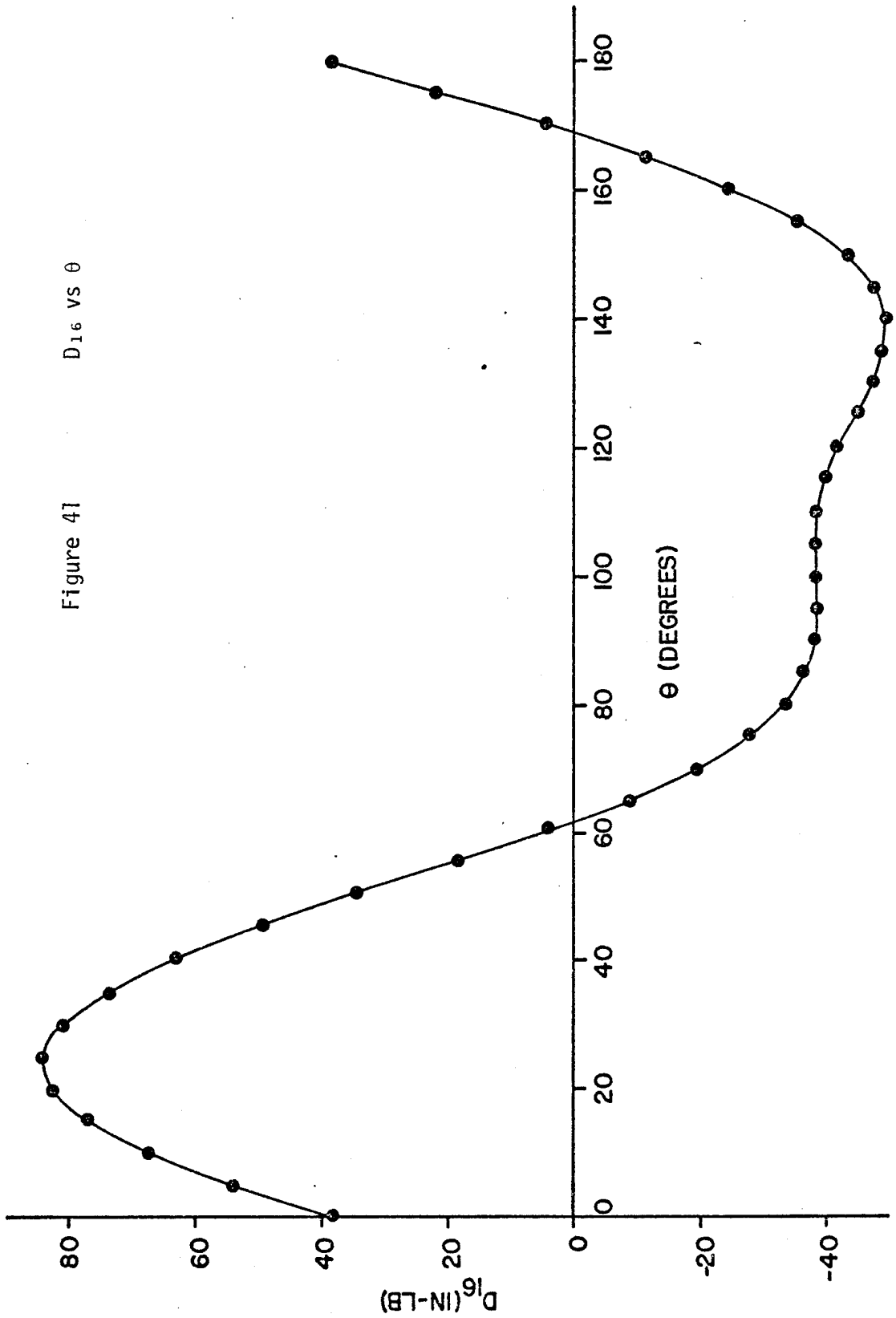

Figure 41 D_{16} vs θ

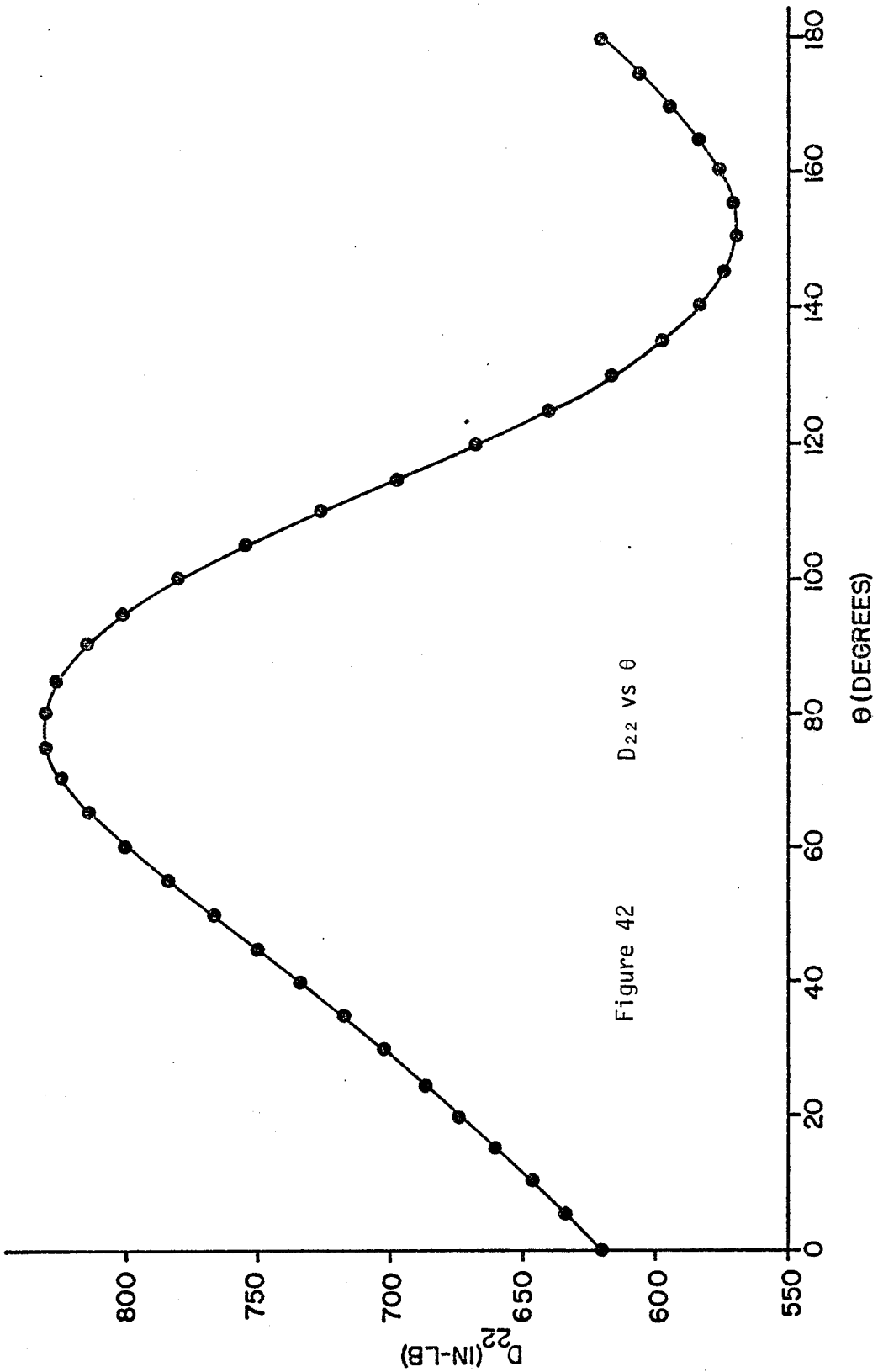

Figure 42 D_{22} vs θ

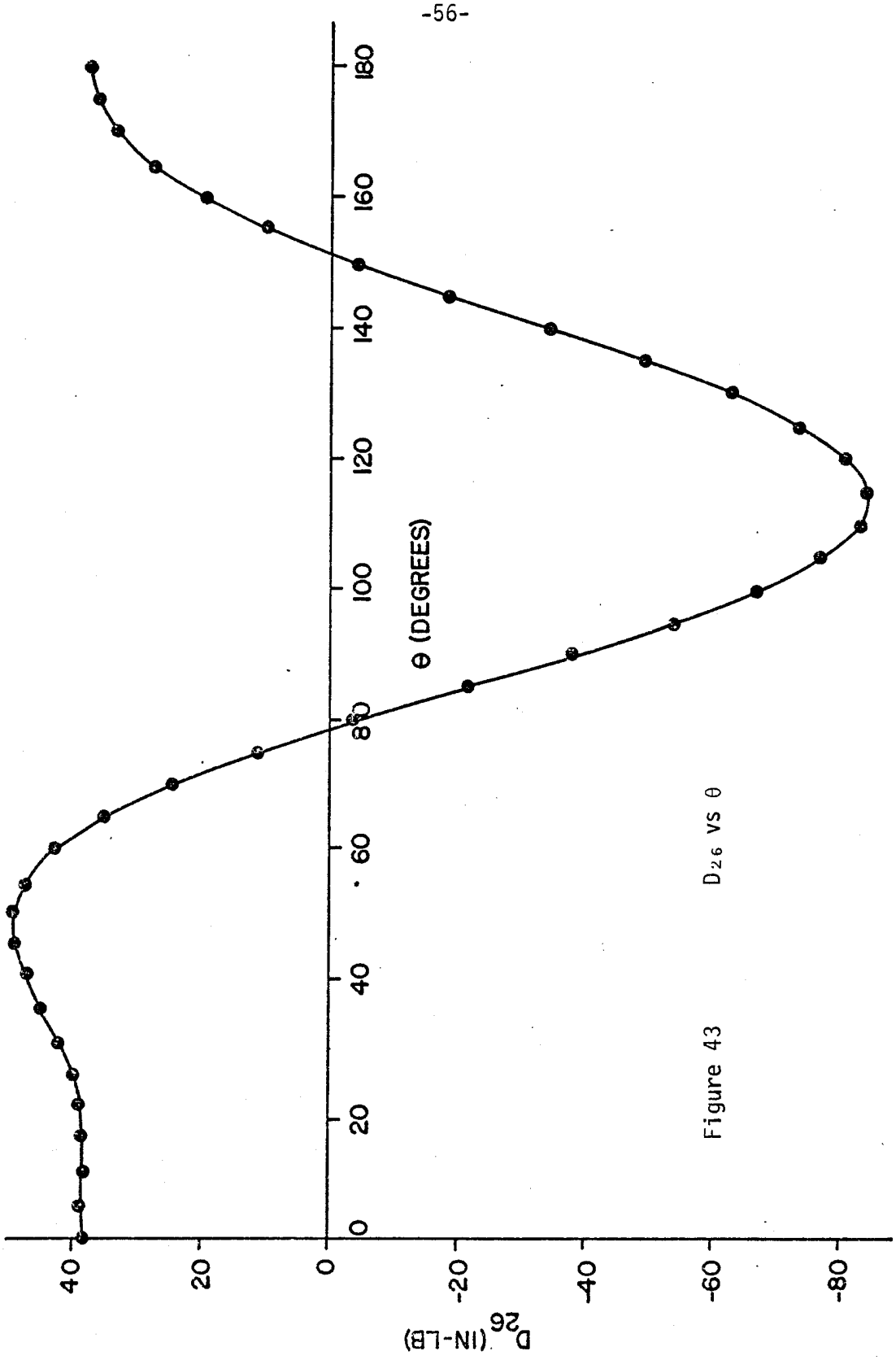

Figure 43 D_{26} vs θ

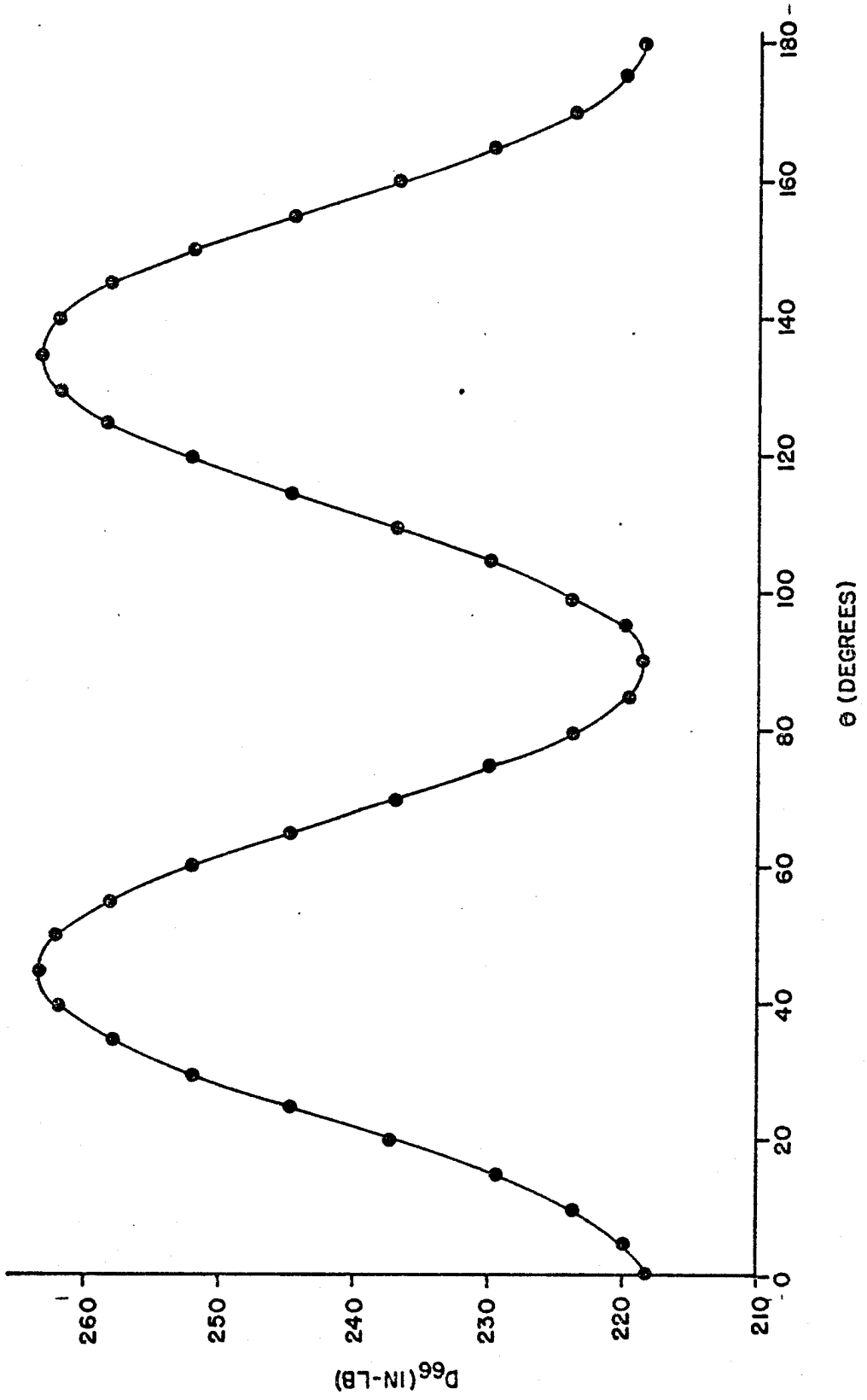

Figure 44 D_{66} vs θ

$D = D_{11}$ (obtained from the laminate analysis)

$h = 0.134$ in.

$\nu = \nu xy$ (the effective Poisson's ratio of the laminate)

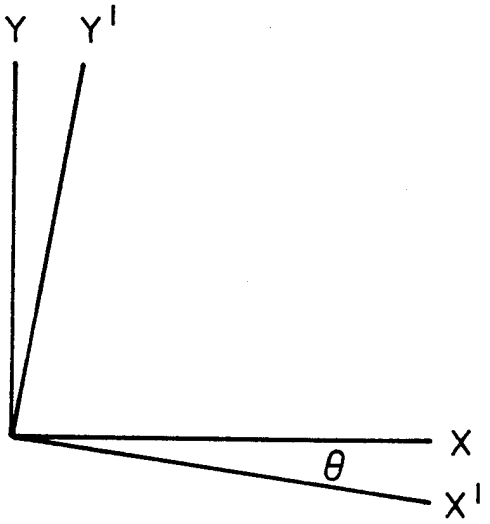

Figure 45 Definition of x' and y'

To calculate Ey' as a function of θ, the following values for D, h and ν were substituted into equation (1):

$D = D_{22}$ (obtained from the laminate analysis)

$h = 0.134$ in.

$\nu = \nu xy$ (the effective Poisson's ratio of the laminate)

Undoubtedly, the Poisson's ratio also varies with θ, but νxy (effective), with a value of 0.3078, sufficed as an approximation. The values of Ex' and Ey' are listed in Table 6.

Each element in the finite element mesh possessed an arc length of 15 degrees. Since Ex' and Ey' were calculated every 5 degrees, an average value for Ex' and Ey' was determined for each element by averaging the four

Table 6 Elastic Moduli Values

θ (Degrees)	Ex' (psi) x 10^6	Ey' (psi) x 10^6
0	3.685	2.800
5	3.613	2.861
10	3.517	2.922
15	3.404	2.982
20	3.277	3.042
25	3.145	3.104
30	3.015	3.168
35	2.893	3.237
40	2.785	3.309
45	2.697	3.385
50	2.631	3.463
55	2.590	3.539
60	2.573	3.610
65	2.577	3.672
70	2.600	3.720
75	2.638	3.748
80	2.686	3.753
85	2.742	3.732
90	2.800	3.685
95	2.861	3.613
100	2.922	3.517
105	2.982	3.404
110	3.042	3.277
115	3.104	3.145
120	3.168	3.015
125	3.237	2.893
130	3.309	2.785
135	3.385	2.697
140	3.463	2.631
145	3.539	2.590
150	3.610	2.573
155	3.672	2.577
160	3.720	2.600
165	3.748	2.638
170	3.753	2.686
175	3.732	2.742
180	3.685	2.800

values of Ex' or Ey' that pertained to that element. For example, if an element spans 30 degrees to 45 degrees and Ex' for that element was desired, the Ex' values calculated for θ = 30, 35, 40, and 45 degrees were averaged to obtain an Ex' value for that element. The Ex' and Ey' values for each element are tabulated in Table 7, where they are labeled Ex' (average) and Ey' (average). There are only 12 average values for Ex' and Ey' because, like the D matrices from which they were derived, they repeat themselves every π radians.

Using the reciprocity relationship the value of νyx for each element was calculated.

$$Ex\ \nu yx = Ey\ \nu xy \quad \ldots\ldots\ldots\ldots\ldots\ldots\ldots\ldots\ldots\ldots \quad (2)$$

The values used in equation (2) to calculate νyx were:

Ex' (average) for the element

Ey' (average) for the element

νxy = 0.3078 = the effective Poisson's ratio of the laminate

The values of νyx for each element, labeled νyx (average), are listed in Table 7.

Finally, the element stiffness matrix may be determined. In matrix notation the stress-strain relation is given as follows [1] :

$$\begin{Bmatrix} \sigma x \\ \sigma y \\ \tau xy \end{Bmatrix} = \begin{bmatrix} Q_{11} & Q_{12} & Q_{16} \\ Q_{21} & Q_{22} & Q_{26} \\ Q_{61} & Q_{62} & Q_{66} \end{bmatrix} \begin{Bmatrix} \varepsilon x \\ \varepsilon y \\ \gamma xy \end{Bmatrix}$$

For a cylindrical disk of orthotropic material, $Q_{16} = Q_{26} = Q_{61} = Q_{62} = 0$.

Table 7 Average Elastic Moduli and Average Poisson's Ratio

θ Values (Degrees)	Ex' (average) x 10^6 (psi)	Ey' (average) x 10^6 (psi)	νyx (average)
0, 5, 10, 15	3.555	2.891	.2503
15, 20, 25, 30	3.210	3.074	.2948
30, 35, 40, 45	2.848	3.275	.3539
45, 50, 55, 60	2.623	3.499	.4106
60, 65, 70, 75	2.597	3.688	.4371
75, 80, 85, 90	2.717	3.730	.4226
90, 95, 100, 105	2.891	3.555	.3785
105, 110, 115, 120	3.074	3.210	.3214
120, 125, 130, 135	3.275	2.848	.2677
135, 140, 145, 150	3.499	2.623	.2307
150, 155, 160, 165	3.688	2.597	.2167
165, 170, 175, 180	3.730	2.717	.2242

The remaining matrix terms are calculated as follows:

$$Q_{11} = Ex/(1-\nu xy\ \nu yx) \quad \ldots\ldots\ldots\ldots\ldots\ldots\ldots\ldots\ldots\ldots (3)$$

$$Q_{12} = Q_{21} = (\nu yx\ Ex)/(1-\nu xy\ \nu yx) \quad \ldots\ldots\ldots\ldots\ldots\ldots\ldots (4)$$

$$Q_{22} = Ey/(1-\nu x y\ \nu yx) \quad \ldots\ldots\ldots\ldots\ldots\ldots\ldots\ldots\ldots (5)$$

$$Q_{66} = G \quad \ldots\ldots\ldots\ldots\ldots\ldots\ldots\ldots\ldots\ldots\ldots\ldots\ldots (6)$$

where

Ex = Ex' (average) for each element

Ey = Ey' (average) for each element

νyx = νyx (average) for each element

νxy = the effective Poisson's ratio of the laminate = 0.3078

G = the effective Shear modulus of the laminate

The stiffness matrix values for each element are listed in Table 8.

Utilizing the stiffness matrices for each element, a finite-element deck was created as shown in Figure 46. The data deck was input into the SAP V program and the resulting output from the SAP V program consisted of plate deflections in the normal direction (these are out-of-plane deflections) and the stress couples Mx and My. A concentrated load of 440 lb. was applied at the center of the mesh (node no. 1) and simply-supported boundary conditions were specified at the outer edge of the mesh to simulate the testing conditions.

Table 8 Stiffness Matrix Values

θ (Degrees)	Q_{11} (psi) x 10^6	$Q_{12} = Q_{21}$ (psi) x 10^6	Q_{22} (psi) x 10^6	Q_{66} (psi) x 10^6
0, 5, 10, 15	3.852	0.964	3.132	1.191
15, 20, 25, 30	3.530	1.041	3.381	1.191
30, 35, 40, 45	3.196	1.131	3.675	1.191
45, 50, 55, 60	3.003	1.233	4.005	1.191
60, 65, 70, 75	3.000	1.312	4.261	1.191
75, 80, 85, 90	3.123	1.320	4.288	1.191
90, 95, 100, 105	3.272	1.239	4.024	1.191
105, 110, 115, 120	3.411	1.096	3.562	1.191
120, 125, 130, 135	3.569	0.955	3.104	1.191
135, 140, 145, 150	3.766	0.869	2.823	1.191
150, 155, 160, 165	3.952	0.856	2.783	1.191
165, 170, 175, 180	4.006	0.898	2.918	1.191

```
00100   A FINITE ELEMENT PROGRAM FOR CONCENTRATED LOADINGS OF A DISK
00200      385     1     1
00300   D    1     1     1                          1          0                    0Z
00400   D    2     1     1                          1       .125                    0Z
00500   D   25     1     1                          1       .125                  345Z    1
00600   D   26     1     1                          1      .1875                    0Z
00700   D   49     1     1                          1      .1875                  345Z    1
00800   D   50     1     1                          1       .25                     0Z
00900   D   73     1     1                          1       .25                   345Z    1
01000   D   74     1     1                          1      .3125                    0Z
01100   D   97     1     1                          1      .3125                  345Z    1
01200   D   98     1     1                          1       .375                    0Z
01300   D  121     1     1                          1       .375                  345Z    1
01400   D  122     1     1                          1      .4375                    0Z
01500   D  145     1     1                          1      .4375                  345Z    1
01600   D  146     1     1                          1         .5                    0Z
01700   D  169     1     1                          1         .5                  345Z    1
01800   D  170     1     1                          1       .625                    0Z
01900   D  193     1     1                          1       .625                  345Z    1
02000   D  194     1     1                          1        .75                    0Z
02100   D  217     1     1                         .1        .75                  345Z    1
02200   D  218     1     1                          1       .875                    0Z
02300   D  241     1     1                          1       .875                  345Z    1
02400   D  242     1     1                          1        1.0                    0Z
02500   D  265     1     1                          1        1.0                  345Z    1
02600   D  266     1     1                          1       1.25                    0Z
02700   D  289     1     1                          1       1.25                  345Z    1
02800   D  290     1     1                          1        1.5                    0Z
02900   D  313     1     1                          1        1.5                  345Z    1
03000   D  314     1     1                          1       1.75                    0Z
03100   D  337     1     1                          1       1.75                  345Z    1
03200   D  338     1     1                          1        2.0                    0Z
03300   D  361     1     1                          1        2.0                  345Z    1
03400   D  362     1     1     1                    1      2.375                    0Z
03500   D  385     1     1     1                    1      2.375                  345Z    1
03600        6   384    12
03700              1
03800         4.006E6     8.983E5          2.918E6          1.191E6
03900              2
04000         3.952E6     8.563E5          2.783E6          1.191E6
04100              3
04200         3.766E6     8.689E5          2.823E6          1.191E6
04300              4
04400         3.569E6     9.554E5          3.104E6          1.191E6
04500              5
04600         3.411E6     1.096E6          3.562E6          1.191E6
04700              6
04800         3.272E6     1.239E6          4.024E6          1.191E6
04900              7
```

Figure 46 Finite Element Deck

05000	3.123E6		1.320E6			4.288E6			1.191E6	
05100	8									
05200	3.000E6		1.312E6			4.261E6			1.191E6	
05300	9									
05400	3.003E6		1.233E6			4.005E6			1.191E6	
05500	10									
05600	3.196E6		1.131E6			3.675E6			1.191E6	
05700	11									
05800	3.530E6		1.041E6			3.381E6			1.191E6	
05900	12									
06000	3.852E6		9.640E5			3.132E6			1.191E6	
06100										
06200										
06300										
06400										
06500										
06600	1	1	2	3		1		.134		
06700	2	2	26	27	3	1	24	.134		
06800	16	338	362	363	339	1		.134		
06900	17	1	3	4		2		.134		
07000	18	3	27	28	4	2	24	.134		
07100	32	339	363	364	340	2		.134		
07200	33	1	4	5		3		.134		
07300	34	4	28	29	5	3	24	.134		
07400	48	340	364	365	341	3		.134		
07500	49	1	5	6		4		.134		
07600	50	5	29	30	6	4	24	.134		
07700	64	341	365	366	342	4		.134		
07800	65	1	6	7		5		.134		
07900	66	6	30	31	7	5	24	.134		
08000	80	342	366	367	343	5		.134		
08100	81	1	7	8		6		.134		
08200	82	7	31	32	8	6	24	.134		
08300	96	343	367	368	344	6		.134		
08400	97	1	8	9		7		.134		
08500	98	8	32	33	9	7	24	.134		
08600	112	344	368	369	345	7		.134		
08700	113	1	9	10		8		.134		
08800	114	9	33	34	10	8	24	.134		
08900	128	345	369	370	346	8		.134		
09000	129	1	10	11		9		.134		
09100	130	10	34	35	11	9	24	.134		
09200	144	346	370	371	347	9		.134		
09300	145	1	11	12		10		.134		
09400	146	11	35	36	12	10	24	.134		

09500	160	347	371	372	348	10		.134
09600	161	1	12	13		11		.134
09700	162	12	36	37	13	11	24	.134
09800	176	348	372	373	349	11		.134
09900	177	1	13	14		12		.134
10000	178	13	37	38	14	12	24	.134
10100	192	349	373	374	350	12		.134
10200	193	1	14	15		1		.134
10300	194	14	38	39	15	1	24	.134
10400	208	350	374	375	351	1		.134
10500	209	1	15	16		2		.134
10600	210	15	39	40	16	2	24	.134
10700	224	351	375	376	352	2		.134
10800	225	1	16	17		3		.134
10900	226	16	40	41	17	3	24	.134
11000	240	352	376	377	353	3		.134
11100	241	1	17	18		4		.134
11200	242	17	41	42	18	4	24	.134
11300	256	353	377	378	354	4		.134
11400	257	1	18	19		5		.134
11500	258	18	42	43	19	5	24	.134
11600	272	354	378	379	355	5		.134
11700	273	1	19	20		6		.134
11800	274	19	43	44	20	6	24	.134
11900	288	355	379	380	356	6		.134
12000	289	1	20	21		7		.134
12100	290	20	44	45	21	7	24	.134
12200	304	356	380	381	357	7		.134
12300	305	1	21	22		8		.134
12400	306	21	45	46	22	8	24	.134
12500	320	357	381	382	358	8		.134
12600	321	1	22	23		9		.134
12700	322	22	46	47	23	9	24	.134
12800	336	358	382	383	359	9		.134
12900	337	1	23	24		10		.134
13000	338	23	47	48	24	10	24	.134
13100	352	359	383	384	360	10		.134
13200	353	1	24	25		11		.134
13300	354	24	48	49	25	11	24	.134
13400	368	360	384	385	361	11		.134
13500	369	1	25	2		12		.134
13600	370	25	49	26	2	12	24	.134
13700	384	361	385	362	338	12		.134
13800	1	1				-440.0		
13900								
14000								
14100								
14200								

V. Finite-Element Model Verification

The validity of the finite-element model was determined through two tests. One test compared the deflection of the plate, as predicted by a modified classical plate theory, to the deflection of the plate as given by the finite-element model. The other test compared radial strains given by the finite-element model to radial strains measured from strain gages mounted on two of the pristine disks. These tests are described in detail in the following pages.

A. Deflection Comparison

The plates used in the static and fatigue loading tests were quasi-isotropic inplane and non-axisymmetric. Classical plate theory assumes an isotropic, axisymmetric plate. To use classical plate theory for our disks to obtain approximate results for the deflection of the plate, the effective laminate properties of the plate were used. These properties were obtained from a laminate analysis; their use in the evaluation of a modified classical plate theory provides plate deflections which can be compared to the deflections predicted by the finite-element model. The equation which predicts the modified classical plate theory deflections is derived in Appendix D.

Table 9 lists the deflection of the plate as a function of the radius of the plate, r. The deflection, w, for several values of θ (as given by

	Modified Classical Plate Theory	Finite-Element Model: w (inches)			
r (inches)	w (inches)	$\theta = 0^o$	$\theta = 45^o$	$\theta = 90^o$	$\theta = 135^o$
0.125	-0.18010	-0.17857	-0.17821	-0.17816	-0.17855
0.250	-0.17755	-0.17504	-0.17402	-0.17388	-0.17499
0.500	-0.16879	-0.16346	-0.16122	-0.16086	-0.16335
0.750	-0.15590	-0.14747	-0.14433	-0.14378	-0.14736
1.000	-0.13947	-0.12835	-0.12470	-0.12402	-0.12825
1.500	-0.09747	-0.08417	-0.08068	-0.07996	-0.08413
2.000	-0.04509	-0.03620	-0.03425	-0.03382	-0.03620

Table 9 Deflection Results

the finite-element model) are listed. The results show that for small values of r ($r \leq 1$ inch), the modified classical plate theory and the finite-element model agree within 10 percent. Larger values of r ($r > 1$ inch) result in greater margins of error.

The "ball park" agreement of deflection values between the modified classical plate theory and the finite-element model suggests that the finite-element model is valid within reason. However, another comparison was needed to truly validate the finite-element model. The radial strain comparison, which is described next, provided this validation of the finite-element model.

B. Radial Strain Comparison

To measure the radial strains in the pristine disks, strain gages were mounted on the disks (numbers 33 and 34) as shown in Figure 47. The disks were loaded statically in the apparatus shown in Figure 1. The load was applied at the center of each disk with a 1 inch diameter ball bearing. The strain gages were connected to a strain recorder; load and strain readings were taken while the disks were loaded to 550 (lb). After the data was collected (see Tables 10 and 11), load vs. strain graphs were prepared for each gage (see Figures 48-50). Using these graphs, the strain at any gage location for a given load can be determined.

The location of the strain gages used in the radial strain comparison (gages 1 and 3 only) present a problem in trying to compare their strain output to the strain predicted by the finite-element model. To compare the measured strains and the finite-element strains, the centers of the strain gages and the centers of two elements must coincide. However, as shown in Figure 51, this does not occur.

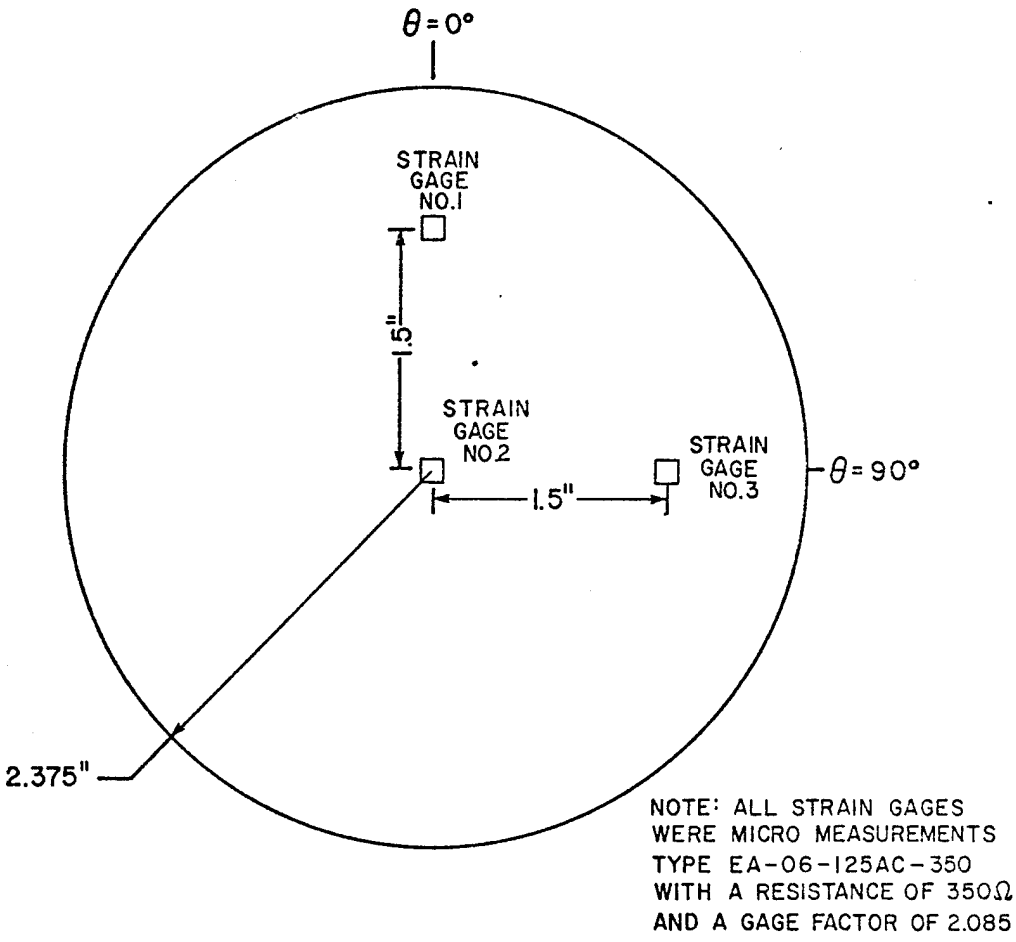

Figure 47 Location of Strain Gages

Table 10 Strain Results from Disk 33

Load lb	Gage # 1 Strain (μ in/in)	Gage # 2 Strain (μ in/in)	Gage # 3 Strain (μ in/in)
11	30	340	0
22	50	680	20
33	80	970	30
44	100	1290	30
55	100	1600	60
66	140	1930	80
77	140	2250	100
88	170	2580	120
99	200	2910	140
110	240	3270	180
121	240	3600	200
132	290	3940	220
143	310	4310	240
154	340	4680	260
165	380	5060	300
176	400	5430	310
187	430	5800	330
198	470	6200	370
209	510	6580	400
220	530	7000	420
242	600	7800	470
264	680	8560	530
286	730	9320	590
308	790	10100	630
330	850	10910	690
352	930	11730	750
374	1000	12510	800
396	1050	13330	880
418	1140	14110	940
440	1200	14980	1000
495	1370	17170	1150
550	1550	19400	1320

Table 11 Strain Results from Disk 34

Load lb	Gage # 1 Strain (μ in/in)	Gage # 2 Strain (μ in/in)	Gage # 3 Strain (μ in/in)
11	0	230	30
22	10	450	40
33	40	700	80
44	40	920	100
55	60	1140	120
66	90	1400	130
77	110	1640	160
88	110	1880	180
99	150	2130	210
110	170	2380	240
121	200	2640	260
132	240	2900	280
143	240	3190	300
154	290	3430	340
165	300	3710	360
176	340	4000	400
187	380	4300	410
198	400	4580	440
209	430	4840	470
220	440	5130	500
242	520	5680	570
264	600	6260	610
286	630	6840	690
308	690	7400	760
330	780	7980	820
352	840	8540	870
374	900	9100	940
396	960	9640	1000
418	1040	10210	1070
440	1100	10790	1130
495	1260	12330	1310
550	1430	14060	1470

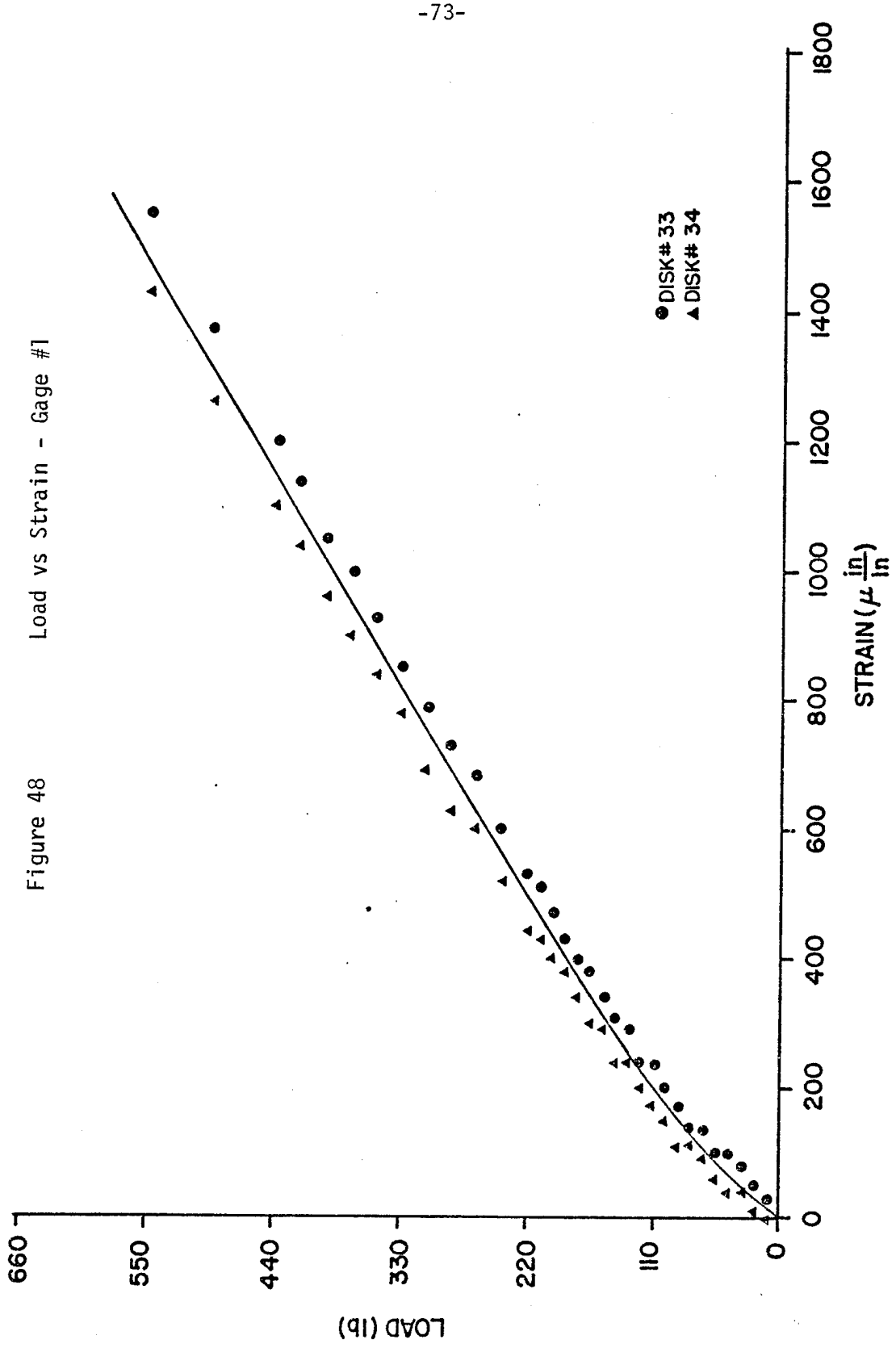

Figure 48 Load vs Strain - Gage #1

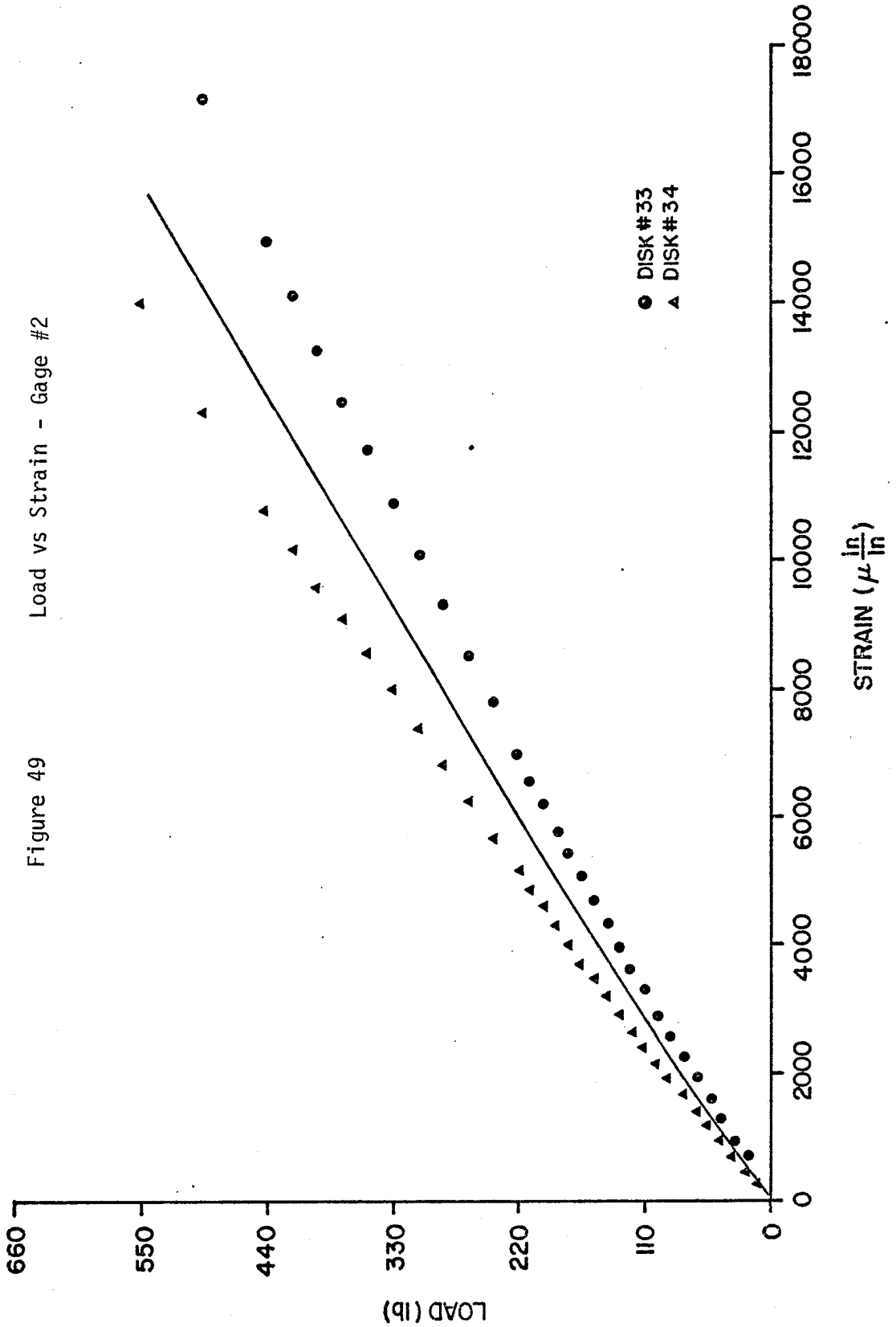

Figure 49 Load vs Strain - Gage #2

Figure 50 Load vs Strain - Gage #3

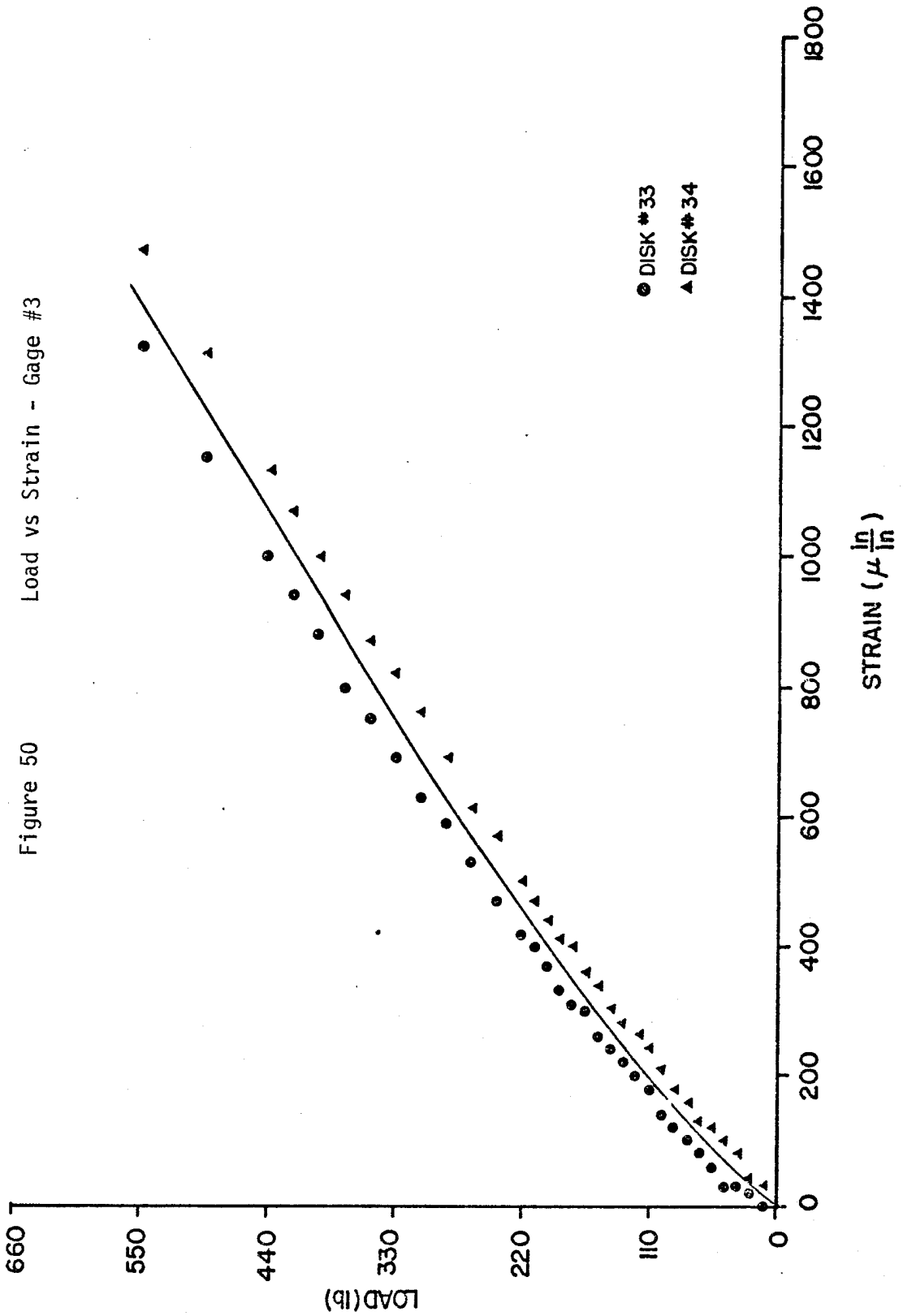

To find the Mx and My values (the bending moment components of the plate) at r = 1.5 inches (the distance from the center of a disk to the center of a strain gage), interpolation techniques were used. Mr, which is equivalent to Mx in the element coordinate system as defined by the finite-element program, versus angular position, θ was plotted using the elements whose centers lie at radial distances of 1.125, 1.375, 1.625, and 1.875 inches (see Figure 52 and Table 12). Likewise, Mθ, which is equivalent to My in the element coordinate system, versus angular position, θ was plotted using the elements whose centers lie at radial distances of 1.125, 1.375, 1.625, and 1.875 inches (see Figure 53 and Table 13). Using these curves as guidlines, a curve for r = 1.500 inches was determined by interpolation. The new curves provided the Mr and Mθ values that were needed to compare the strain gage radial strains with the radial strains predicted by the finite-element model and Appendix E.

A radial strain comparison using gage no. 1 ($\theta = 0^{o}$), a concentrated loading of 440 lb (which corresponds to the load input into the finite-element program), and equation (10) in Appendix E shows that for $\theta = 0^{o}$ the values of Mr and Mθ are:

Mr = -24.3 lb Mθ = -42.2 lb

$|\varepsilon r|$(finite-element model) = 1025.7 μin/in

εr (strain gage) = 1140 μin/in

A radial strain comparison using gage no. 3 ($\theta = 90^{o}$), a concentrated loading of 440 lb (which corresponds to the load inputed to the finite-element program), and equation (13) in Appendix E, shows that for

Table 12 Mr (as a function of r) vs Theta

θ Value (Degrees)	Mr (lbs) r = 1.125 in.	Mr (lbs) r = 1.375 in.	Mr (lbs) r = 1.625 in.	Mr (lbs) r = 1.875 in.
-172.5	-37.29	-27.51	-19.46	-12.65
-157.5	-34.68	-25.63	-18.18	-11.86
-142.5	-32.25	-23.93	-17.07	-11.21
-127.5	-30.82	-22.90	-16.38	-10.79
-112.5	-30.49	-22.59	-16.10	-10.54
- 97.5	-31.03	-22.87	-16.19	-10.50
- 82.5	-32.15	-23.67	-16.71	-10.82
- 67.5	-33.69	-24.90	-17.66	-11.50
- 52.5	-35.60	-26.44	-18.87	-12.41
- 37.5	-37.59	-27.98	-20.02	-13.22
- 22.5	-38.99	-28.96	-20.65	-13.58
- 7.5	-38.96	-28.81	-20.44	-13.33
7.5	-37.29	-27.51	-19.46	-12.65
22.5	-34.68	-25.63	-18.18	-11.86
37.5	-32.25	-23.93	-17.07	-11.21
52.5	-30.82	-22.90	-16.38	-10.79
67.5	-30.49	-22.59	-16.10	-10.54
82.5	-31.03	-22.87	-16.19	-10.50
97.5	-32.15	-23.67	-16.71	-10.82
112.5	-33.69	-24.90	-17.66	-11.50
127.5	-35.60	-26.44	-18.87	-12.41
142.5	-37.59	-27.98	-20.02	-13.22
157.5	-38.99	-28.96	-20.65	-13.58
172.5	-38.96	-28.81	-20.44	-13.33

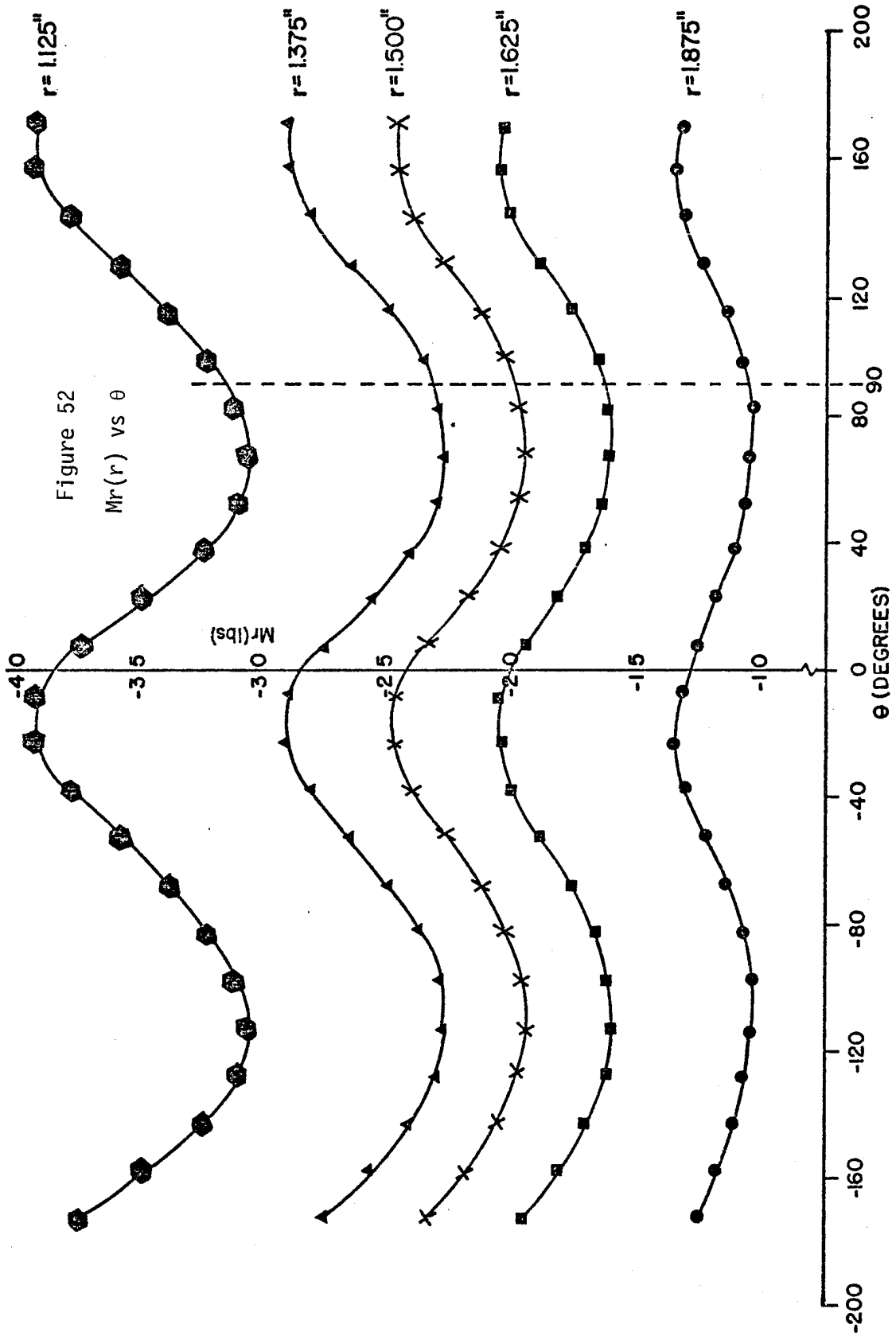

Figure 52
Mr(r) vs θ

Table 13 Mθ (as a function of r) vs Theta

θ Value (Degrees)	Mθ (lbs) r = 1.125 in.	Mθ (lbs) r = 1.375 in.	Mθ (lbs) r = 1.625 in.	Mθ (lbs) r = 1.875 in.
-172.5	-55.32	-46.60	-39.47	-33.44
-157.5	-57.63	-48.68	-41.29	-34.99
-142.5	-60.05	-50.86	-43.20	-36.62
-127.5	-62.07	-52.73	-44.92	-38.16
-112.5	-63.16	-53.82	-45.99	-39.20
-97.5	-62.94	-53.69	-45.95	-39.26
-82.5	-61.36	-52.24	-44.64	-38.10
-67.5	-58.77	-49.76	-42.30	-35.92
-52.5	-55.91	-47.02	-39.71	-33.50
-37.5	-53.74	-44.98	-37.83	-31.80
-22.5	-52.94	-44.31	-37.29	-31.39
-7.5	-53.59	-45.00	-38.00	-32.11
7.5	-55.32	-46.60	-39.47	-33.44
22.5	-57.63	-48.68	-41.29	-34.99
37.5	-60.05	-50.86	-43.20	-36.62
52.5	-62.07	-52.73	-44.92	-38.16
67.5	-63.16	-53.82	-45.99	-39.20
82.5	-62.94	-53.69	-45.95	-39.26
97.5	-61.36	-52.24	-44.64	-38.10
112.5	-58.77	-49.76	-42.30	-35.92
127.5	-55.91	-47.02	-39.71	-33.50
142.5	-53.74	-44.98	-37.83	-31.80
157.5	-52.94	-44.31	-37.29	-31.39
172.5	-53.59	-45.00	-38.00	-32.11

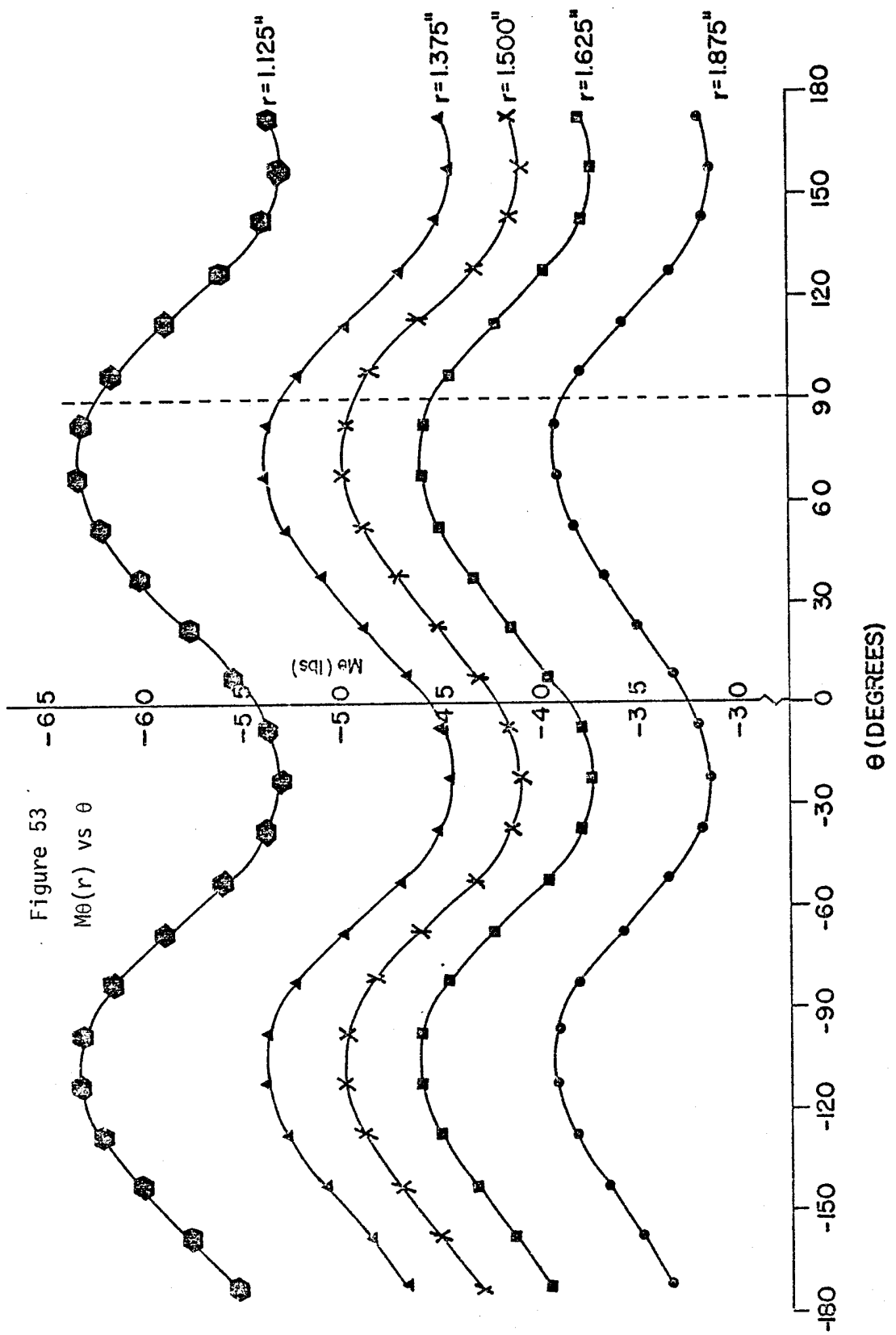

Figure 53
Mθ(r) vs θ

$\theta = 90^{o}$ the values of Mr and Mθ are:

Mr = -20.0 lb Mθ = -49.2 lb

$|\varepsilon r|$(finite-element model) = 1012.8 μin/in

εr (strain gage) = 1065 μin/in

The radial strains for $\theta = 0^{o}$ differed by 10 percent while the radial strains for $\theta = 90^{o}$ differed by only 5 percent. Taken collectively, these results, as well as, the deflection comparison results prove that the finite-element model that was developed is a good tool in predicting the behavior of the fiberglass disks used in this study.

VI. Conclusions and Recommendations

The ultrasonic scans of the fiberglass disks tested in the Fatigue I Phase show that the ball bearing size had no effect on the rate and amount of damage produced in the disk. In the Fatigue II Phase, the size of the implanted defects had no effect on the rate and amount of damage that occured in the disks. However, the amount of damage that occured in the pristine disks after 50,000 fatigue cycles was comparable to the amount of damage that occured in the defective disks after only 10,000 fatigue cycles. Thus, as one would expect, an implanted defect increases the rate of damage. The results of the Static I Phase also show that the size of the implanted defects had no effect on the rate and amount of damage that occured in the disks.

Predicting the location of individual delaminations by ultrasonic scanning techniques proved to be very successful. By moving the ultrasonic transducer over the damaged regions and recording their waveforms, the location of each delamination could be determined. Not every delamination could be located; delaminations near the center of the material could not be detected due to the reasons discussed in Section III.

One disadvantage of using ultrasonic scanning techniques is the amount of time it takes to make a scan. A scan of a single disk required approximately 15 minutes; therefore, to use ultrasonic scanning in a mass production environment is highly impractical.

The finite-element model that was developed can be used to predict (within an accuracy of 5-10 percent) the deflections and bending moment components (Mx, My, and Mxy) for a pristine disk. The finite-element model also explains the symmetrical, "lobe-like" damage patterns. Symmetrical damage patterns were formed because the strains in a disk repeated after π radians.

Three recommendations for future studies are as follows: First, a technique could be developed which utilized the finite-element model to predict the magnitude of the interlaminar shear stresses. Knowing the magnitude of the interlaminar shear stresses would lead to answers as to why the delaminations occur where they do.

The second recommendation is that ultrasonic scanning techniques should be used to evaluate the damage patterns of other materials. Robert Blake (reference [2]) has conducted damage analysis with graphite-epoxy disks. He discovered that the damage is of the same form, "lobe-like" patterns,and that the damage can be detected ultrasonically as to show individual delaminations. SMC materials, which have tremendous potential in automotive applications, should also be examined by scanning techniques.

The last recommendation to be suggested would require the separation of each disk into its individual plys. By isolating each ply, the size of the delaminations could be determined and compared to the size of the delaminations as shown in the "C" scans. Photomicrographs show that delaminations exist and their size to some extent, but the actual size of the delaminations is indeterminant.

VII. References

1. J.R. Vinson and T.W. Chou, "Composite Materials and Their Use in Structures", Wiley, 1975.

2. Robert A. Blake, "Instructions for Operation of Panametrics Ultrasonic Analyzer and Tektran Immersion Scanner", 1978.

3. J.R. Vinson, "Structural Mechanics: The Behavior of Plates and Shells", Wiley, 1974.

4. S.G. Lekhnitskii, "Anisotropic Plates", Gordon and Breach, 1968.

VIII. Acknowledgments

The authors would like to thank Robert Blake for his assistance in the ultrasonic scanning work and Jack Gillespie, Jr. for his assistance in creating the finite-element model.

Appendix A

Producing Ultrasonic "C" Scans [2]

Ultrasonic "C" scanning is a method of non-destructive evaluation that utilizes sound waves to interrogate the internal structure of materials. Voids, delaminations, and changes in thickness are just a few of the many uses of "C" scanning. There are basically two types of "C" scans - a peak amplitude based "C" scan and a frequency based "C" scan. All of the "C" scanning involved in this project employed peak amplitude based "C" scans. Thus, the following discussion centers around peak amplitude based "C" scans.

The Equipment Used in Ultrasonic Scanning

The pieces of equipment used in "C" scanning the fiberglass disks will be referred to during the course of this paper, so they are listed below for easy reference. The equipment is shown in Figures 54 and 55.

RIA - 10A TS Amplifier by TekTran

5052UA Ultrasonic Analyzer by Panametrics

SR-254 Ultrasonic Recording System by TekTran

565 Oscilloscope by Tektronics

Basic Theory of Operation

The specimen is submerged into water and is placed on two plexiglass supports. These supports are supported by a large plexiglass plate

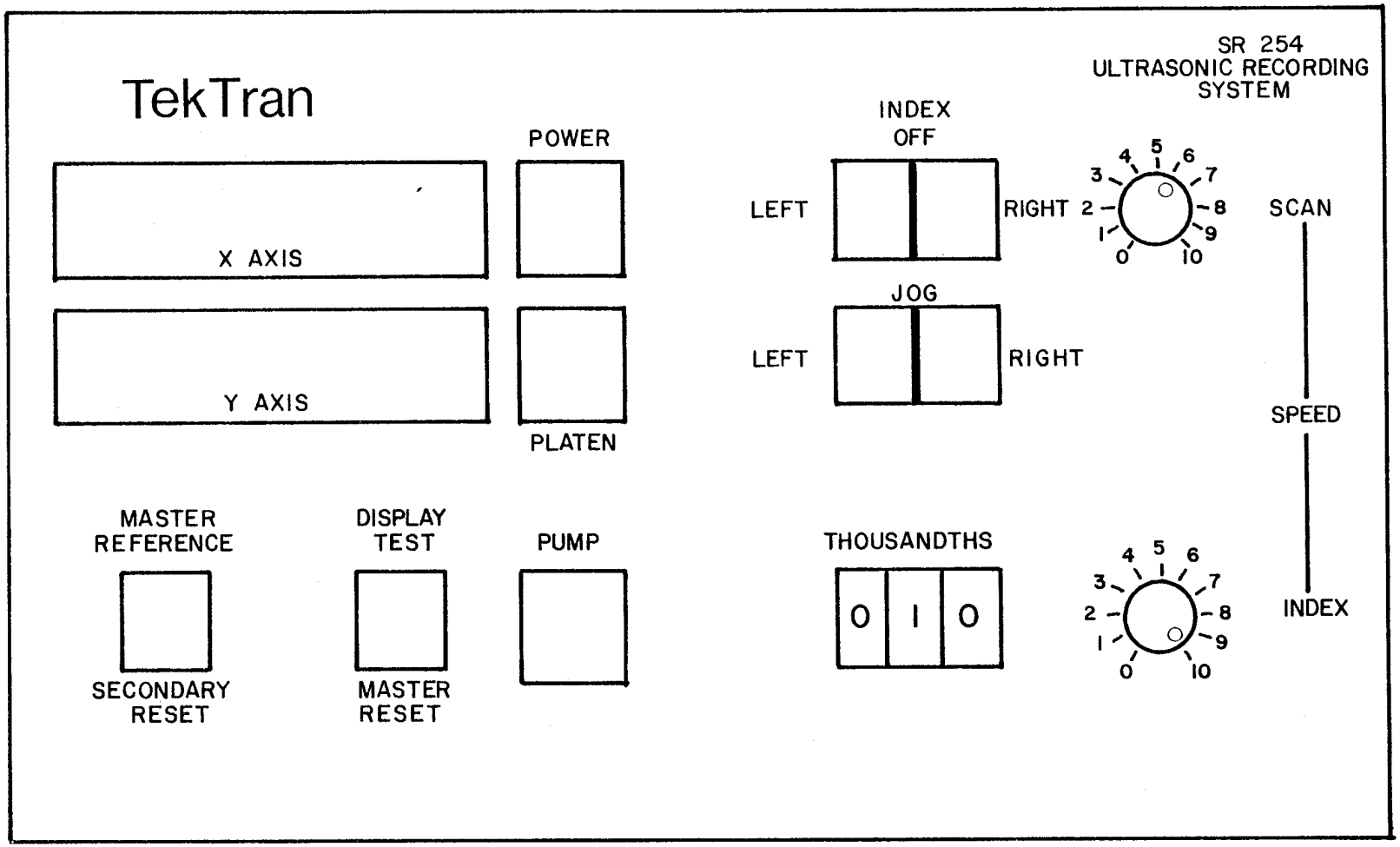

Figure 54 Ultrasonic Recording System

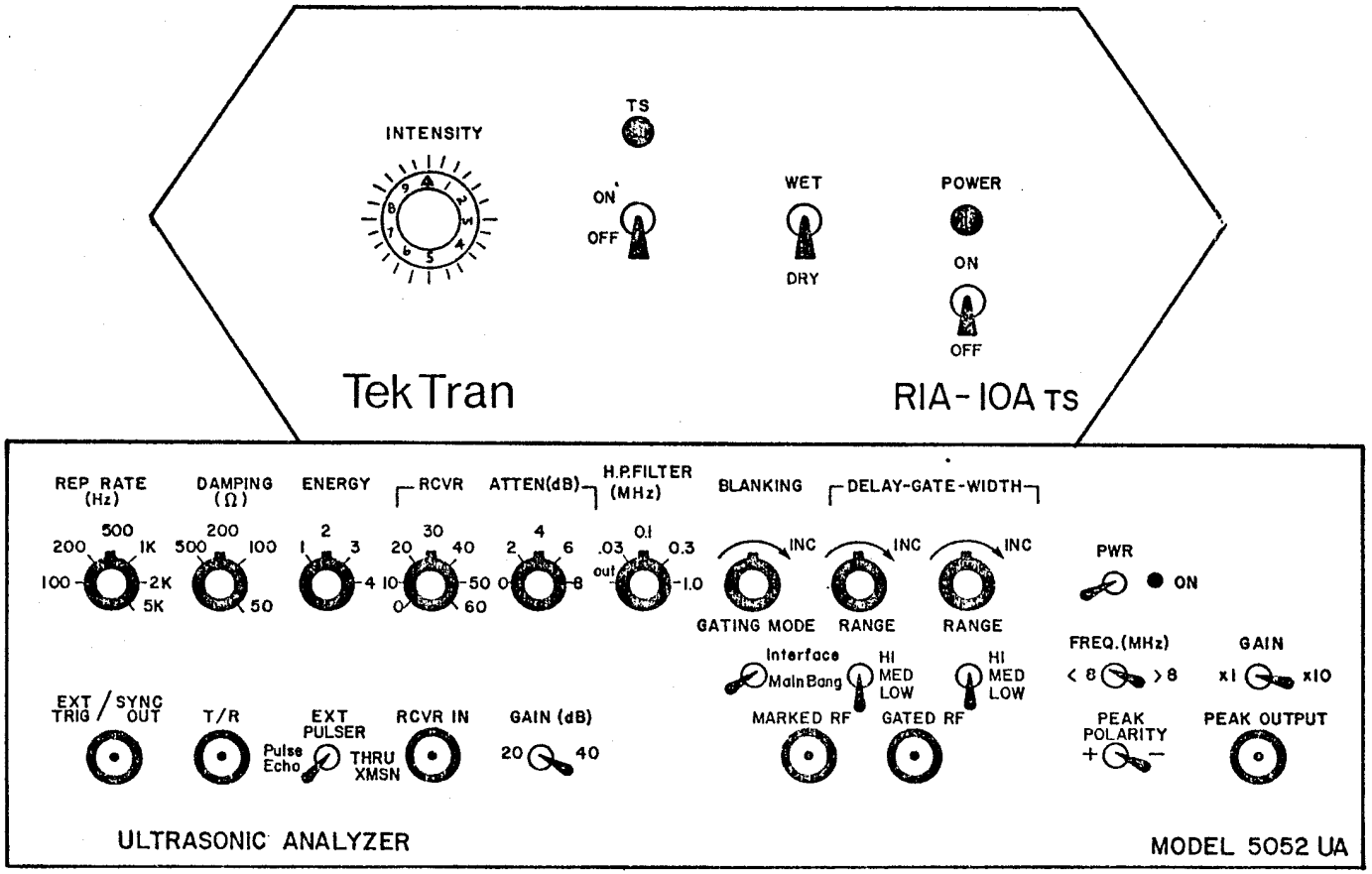

Figure 55 Ultrasonic Analyzer and Pen Amplifier

as shown in Figure 56. The water serves as a coupler between the specimen and the sound waves emitted by the transducer. Oil or some other medium may be used in place of water, but water is readily available and it is easy to work with. Once the specimen is in place, the transducer is lowered into the water and is set at a prescribed height above and perpendicular to the specimen. This prescribed height will be defined later.

When the transducer is excited by an electrical impulse, it emits a pulse of sound. After penetrating the specimen, the sound wave is reflected back to the transducer. A reflected wave of an undamaged region of a disk is shown in Figures 57 and 58. The front surface of the speciment, as well as the back surface, produce large relections because they represent the boundaries between the water and the specimen. Water, and in this case fiberglass, have different densities so the sound wave emitted by the transducer travels at different speeds while traversing through them. Changes in density create the peaks shown in the waveform.

Using the oscilloscope, the distance from the mainbang pulse (the sound wave emitted by the transducer) to the front surface reflection should be set at 50 μsec. This distance, the prescribed height mentioned before, is obtained by moving the transducer up and down. The mainbang pulse is arbitrarily set at 0 μsec; thus when the front surface reflection is set at 50 μsec, the transducer is properly focused.

Behind the back surface reflection are three sets of smaller wavefroms. The first set of waveforms are labeled second multiples. Second multiples are the sound waves that have penetrated the specimen and have

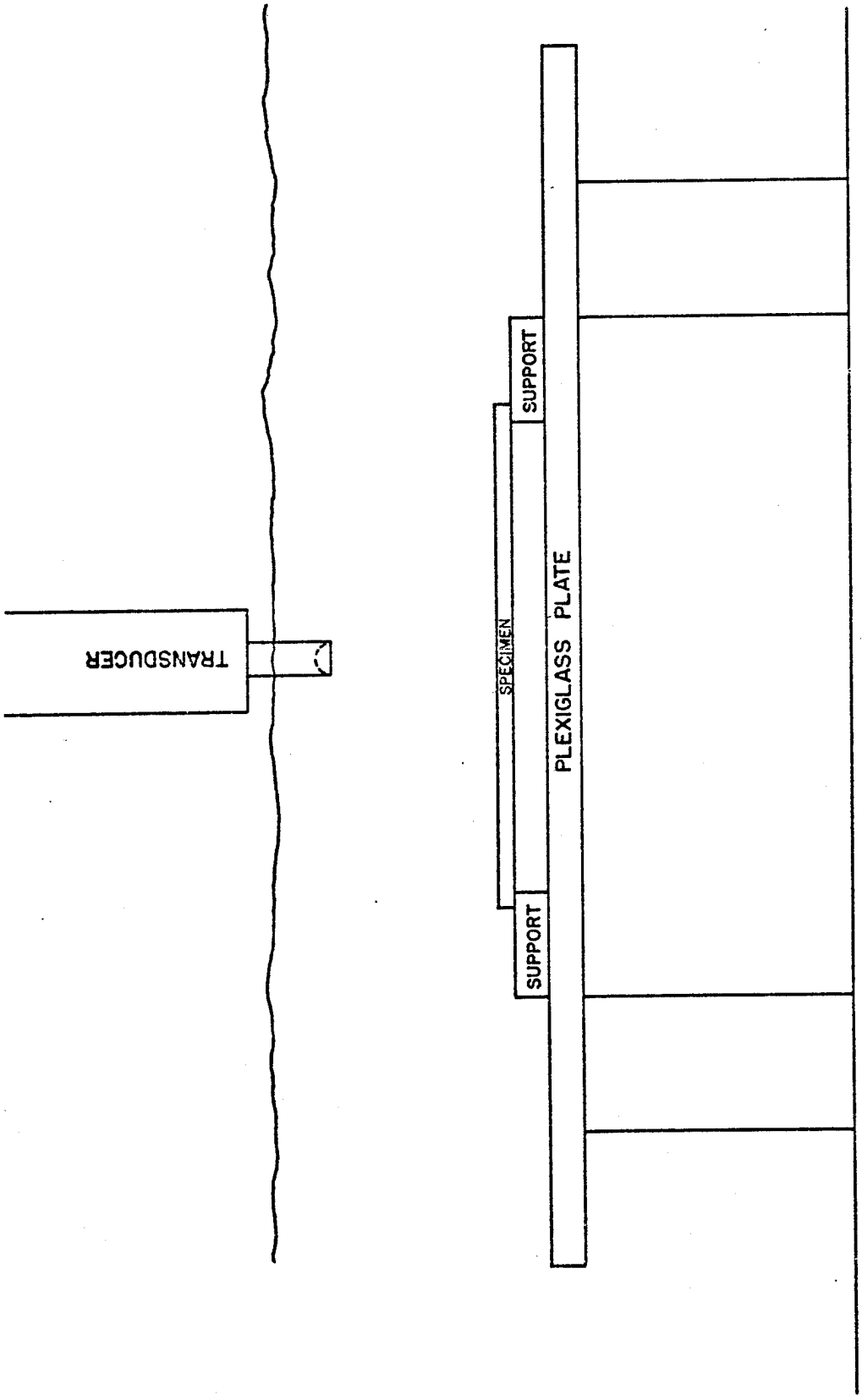

Figure 56 "C" Scan Tank Set Up

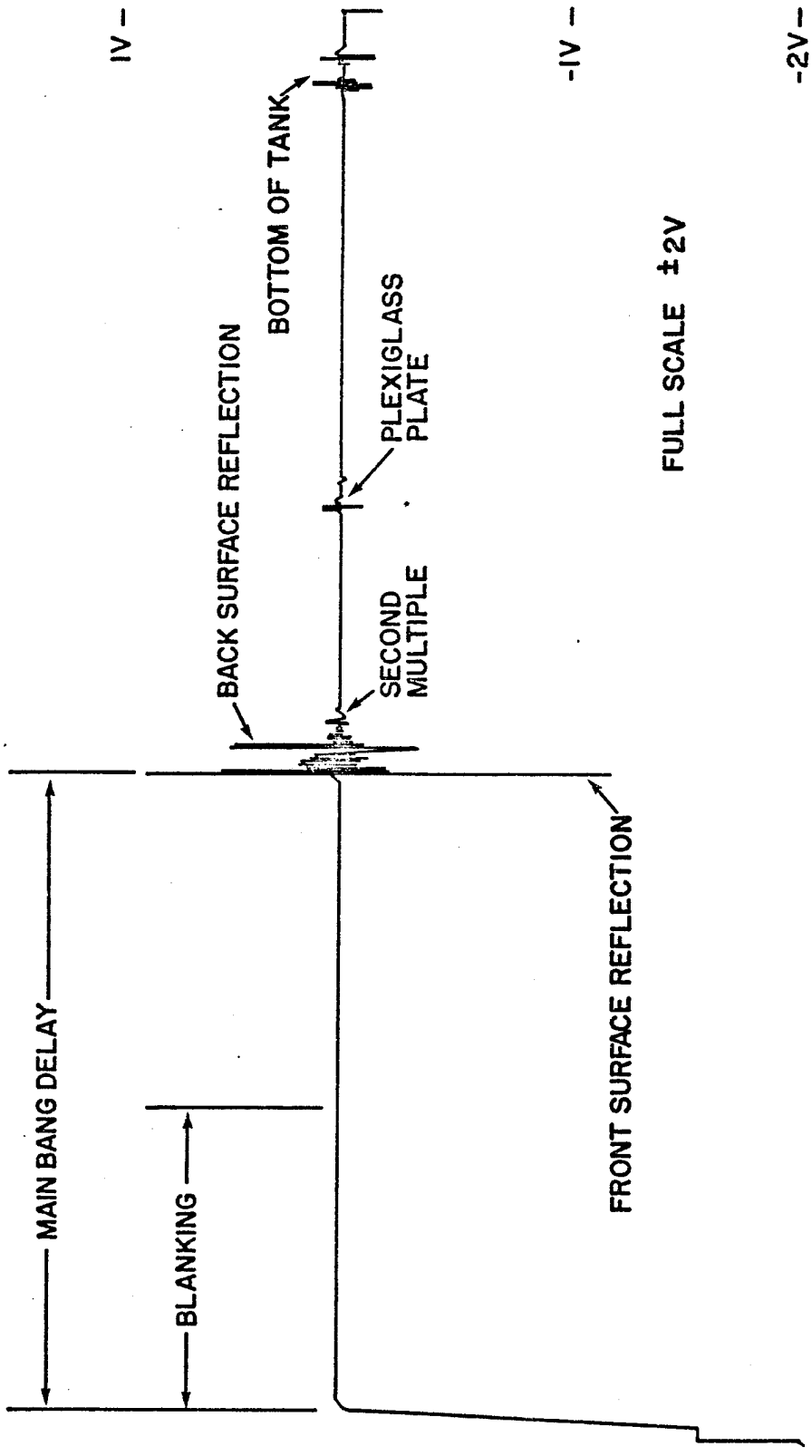

Figure 57 An Ultrasonic Waveform of an Undamaged Region

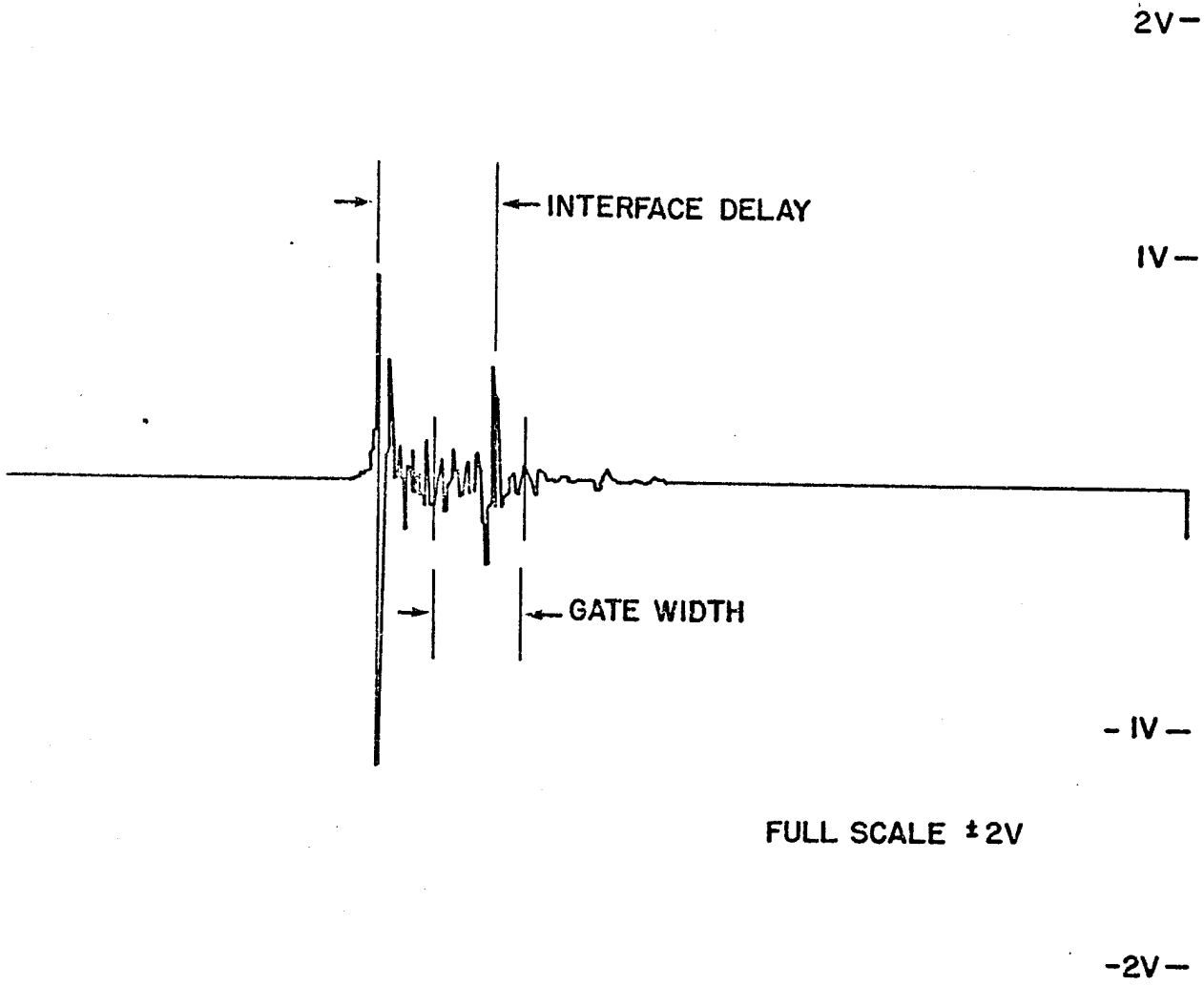

Figure 58 An Ultrasonic Waveform of an Undamaged Region (x4)

not been reflected back to the transducer directly. Instead, they have reflected back to the front surface of the specimen, then through the specimen again, and finally they have been reflected back to the transducer. Third and fourth multiples are like second multiples but the sound waves have bounced around inside the specimen more before being reflected back to the transducer.

The other two waveforms are reflections from the plexiglass plate and the bottom of the tank, respectively. In order to obtain a clear back surface reflection that was not distorted by the plexiglass plate or the tank bottom echos, the specimen had to be placed on the plexiglass supports that were mentioned earlier. Without these supports, the back surface reflection would have been considerably distorted.

Once the reflected waveform is received by the transducer, it enters some gating circuitry where a selected portion of the waveform is analyzed. The gating circuitry is located in the Ultrasonic Analyzer. Each peak in the gated region is converted into a D.C. voltage, which is amplified to values between 1 and 10 volts. From the Analyzer the amplified voltage is sent to the Pen Amplifier, where it is quantisized into one of 10 regions. Each region constitutes one volt and represents a different shade of gray. The quantisized voltage enters current limiting circuitry, from which varying amounts of current are sent to the pen tip. Here, the current determines the amount of oxide that is burned off ink impregnated, oxide coated paper. The image formed by the hot pen is composed of scan lines which in turn are composed of many dots. The shade

of gray of each dot was determined in the Pen Amplifier. The image is a 1:1 scale of the actual specimen. A schematic of the path of an ultrasonic waveform is drawn in Figure 59.

Additional Notes on the Theory of Operation

The resolution of a "C" scan, as well as, it's lightness or darkness may be controlled through knobs and switches located on the "C" scan equipment. The following pages discuss each piece of equipment and its importance in producing a "C" scan.

I. Ultrasonic Analyzer

The Ultrasonic Analyzer controls the number of sound waves produced by the transducer and their energy level. The gating circuitry is also contained in the Analyzer. The knobs and switches on the Analyzer (see Figure 55) and their functions are as follows:

Rep Rate (Hz)	The Rep Rate controls the rate at which electrical impulses are sent into the transducer. Inside the transducer is a crystal with a large natural frequency at 5MHz and a smaller one at 20 MHz. The electrical impulses excite one of these natural frequencies and sound waves are emitted. Thus a setting of 5K Hz implies that 5000 impulses are given to the transducer, which in turn produces 5000 sound waves.
Frequency (MHz)	This switch is set at less than 8 or greater than 8 depending upon the center frequency of the transducer. The factory rated value for the center frequency of the transducer is 20 MHz.
Energy	The voltage of the electrical impulses sent to transducer is controlled by the Energy knob.

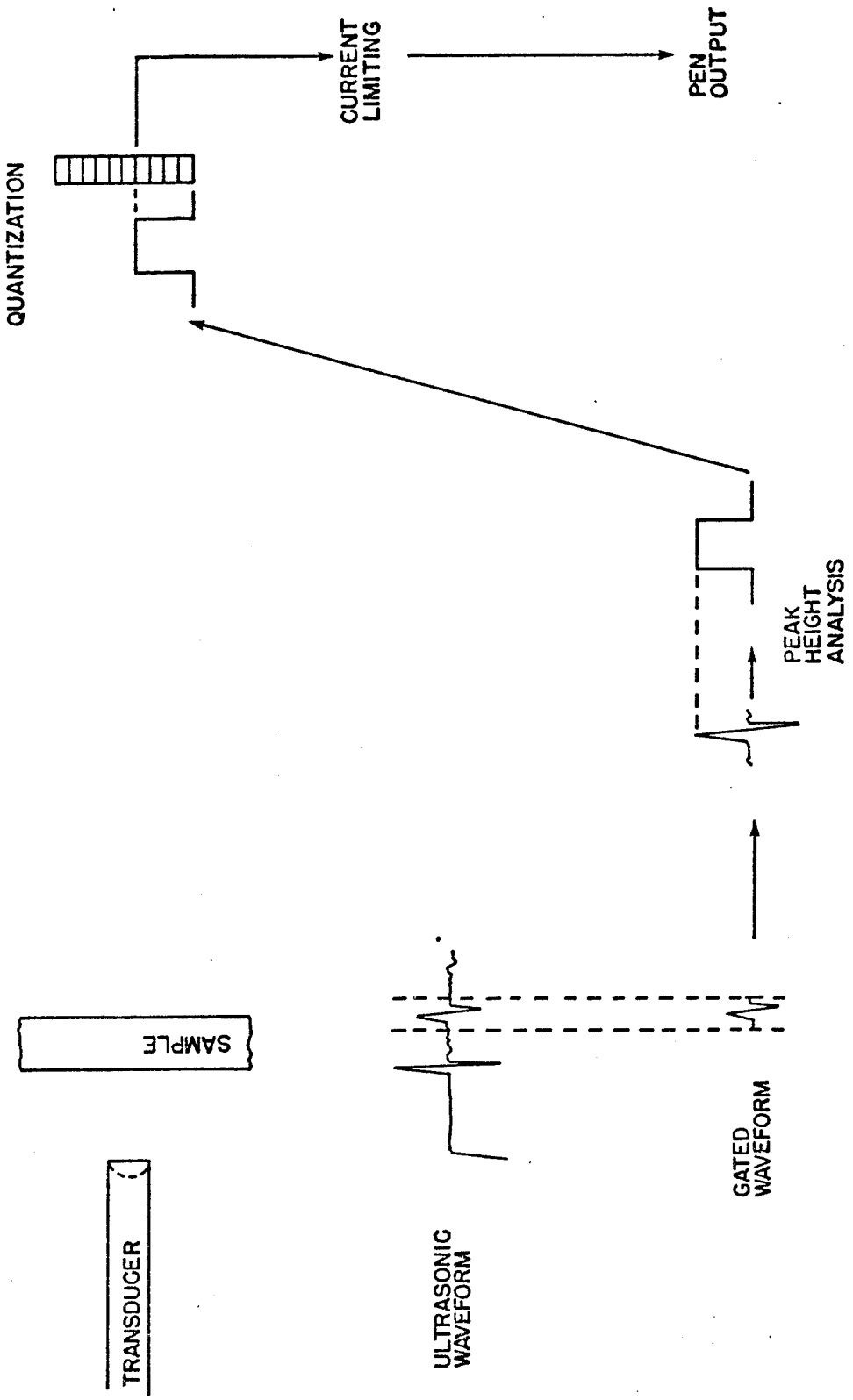

Figure 59 The Path of the Ultrasonic Waveform

As the thickness of materials increases, the required energy for penetration also increases. A setting of one is a small amount of energy while a setting of three is a large amount. The energy should be set as low as possible to avoid damaging the transducer.

H.P. Filtering (MHz) — H.P. stands for high pass; thus a setting of .3 MHz allows any frequencies of the reflected waveform that lie above .3 MHz to proceed to the gating circuitry. Any frequencies below .3 MHz are filtered out; this eliminates a lot of noise in the system.

Pulse Echo/ Thru Xmsn — The Pulse Echo/Thru Transmission switch pertains to the type of scanning set up that is being used. For example, a pulse echo system would have a transducer transmitting sound waves and the same transducer would receive the reflected waves. This is analogous to the type of system used in this project. A thru transmission system would have one transducer transmitting sound waves and another transducer would receive the reflected waves.

Gain (dB) — The gain of the receiver, either 20 dB or 40 dB, may be chosen using this switch.

Interface/Mainbang — This switch allows the operator to trigger the gated region from the front surface reflection or the mainbang pulse. For example, suppose the operator set the beginning of the gated region at 50.5 μsec, or .5 μsec beyond the front surface reflection. If the Interface mode is chosen, the gate will always be triggered at .5 μsec beyond the front surface. If the Mainbang mode is chosen, the gate will always be trigered at 50.5 μ sec beyond the mainbang pulse. An advantage of the former over the latter is shown by a wavy surface. Suppose the operator wished to look at a region of the specimen that started at 50.2 μ sec and ended at 50.5 μ sec. By choosing the Interface mode, the operator's "C" scan would show the structure of that region only. However, by choosing the Mainbang mode, the operator may get a "C" scan showing the waviness of the surface, damage that may lie at the center of the specimen, or both if the specimen has large thickness variations in addition to a wavy surface.

Gate Delay — The time interval between the mainbang pulse and the beginning of the gated region is controlled through this knob.

Gate Width — The operator can adjust the width of the gated region by turning this knob.

Peak Polarity — Each peak in the reflected waveform has a positive and a negative half; the Peak Polarity switch allows the operator to choose which half of the peaks he wishes to use. By selecting the negative half of the peaks, the scan's background is normally lighter than the darker background obtained by choosing the positive half of the peaks.

Blanking — The Blanking knob eliminates any noise in front of the front surface reflection so that the beginning of the gated region will be triggered from the front surface reflection when the Interface mode is in use (see Figure 57).

Gain (x10) — The Pen Amplifier uses voltages that lie between 1 and 10 volts. However, after the selected portion of the reflected waveform (i.e. the gated region) is converted into a D.C. voltage, the peaks of the waveform lie between .1 and 1 volts. Thus the Gain (x10) switch increases the voltages of the peaks in the gated region tenfold so that they may be used in the Pen Amplifier.

Rcvr Atten (dB) — When the reflected waveform first enters the gating circuitry, it's peaks do not lie between .1 and 1 volts. Initially, the peaks have amplitudes varying between .1 and 1.6 volts. However, the darkest shade of gray corresponds to 1 volt, so peaks with amplitudes of 1.2 volts or 1.6 volts will appear (on a "C" scan) as dark as a peak with an amplitude of 1 volt. No contrast between the three voltages will appear on the scan. To alleviate this problem, the Receiver Attenuation knob is used. This knob moves the range of voltage values either up or down towards the middle of the gray scale (.5 volts). For example, suppose the range of voltage values in the gating circuitry vary between .7 and 1.2 volts. By increasing the receiver attenuation (i.e.-a larger number increases the receiver attenuation) the range of voltage values will lie between .4 and .9 volts. This latter range of voltage values has every

peak (after amplification by the Gain (x10) switch) in the gray region where peaks above 10 volts have no use. By increasing the receiver attenuation, the "C" scan becomes lighter because the voltage range is shifted towards the middle of the gray scale.

Damping (Ω) — The damping knob may be used to increase or decrease the resolution of a "C" scan by increasing or decreasing the damping of the waveform in the gating circuitry. While in this circuity, the waveform is oscillating in several potential regions of gray. As was stated before, these regions are determined by the amplitudes of the peaks in the gated region and by the Receiver Attenuation if it is in use. By increasing the damping, the waveform cannot oscillate as much as before and, therefore, potential areas of gray are omitted; thus the resolution of the scan decreases. On the other hand, decreasing the damping allows the waveform to oscillate more and areas of gray are added; thus the resolution of the scan increases. A large amount of damping requires a small amount of resistance (say 50 Ω) while a small amount of damping requires a large amount of resistance (say 200 Ω).

II. Amplifier

The Pen Amplifier has one knob of importance - the intensity knob. A high intensity setting (i.e. a high number) produces a dark "C" scan background while a low intensity setting (i.e. a small number) produces a light background (see Figure 55).

III. Ultrasonic Recording System

The index speed knob on the Recording System dictates the speed of the pen horizontally, while the scan speed knob controls the speed of the pen vertically (see Figure 60). The thousandths setting is the

increment (in thousandths of an inch) that the pen moves horizontally after each movement it makes either up or down (see Figure 54).

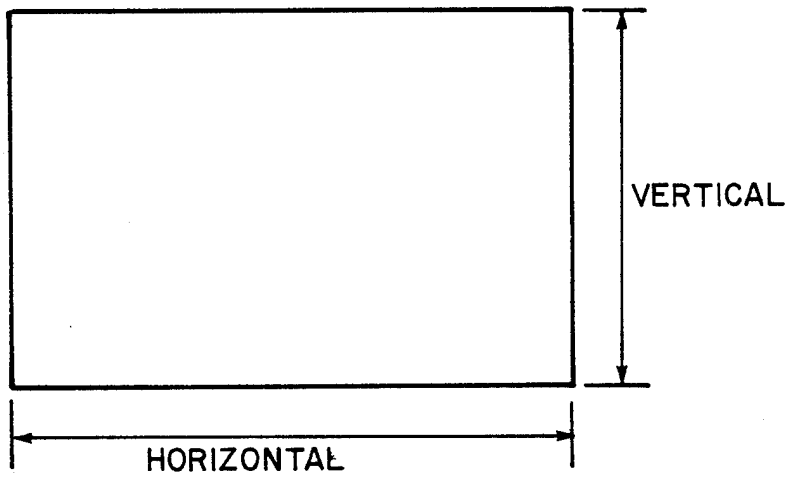

Figure 60 Pen Movement

The line spacing as well as the Rep Rate of the Analyzer are very influential in the resolution of the scan. The Rep Rate determines how many dots per inch there are vertically, while the line spacing determines how many dots per inch there are horizontally. A lot of dots provide great resolution, but the scanning time is greatly increased. Too few dots offer little resolution, but the scanning time is greatly decreased.

The scanning speed and pen tip diameter also affect the "C" scan's resolution. A scanning speed that is too fast may not allow the pen enough time to burn off the required amount of oxide; thus little resolution is achieved. The pen tip diameter is .012 inches, but the size of the dot it creates due to actual contact with the paper is only .005 inches in diameter. Thus the standard line spacing setting of .010 inches leaves a small amount of spacing between each vertical column of dots. This

setting is a fine compromise between a larger setting, where the lines are farther apart and the resolution decreases, and a smaller setting, where the lines overlap one another and provide excellent resolution but greatly increase the scanning time.

IV. Oscilloscope

The basic purposes of the oscilloscope are twofold. The Blanking setting, as well as the settings for the Gate Width and Gate Delay can be made using the oscilloscope. The oscilloscope allows the operator to record and photograph these settings. Figure 6 is a picutre of a photograph taken from the oscilloscope. The top waveform is the reflected waveform in its entirety, while the bottom waveform is the gated region of the reflected waveform.

The second purpose of the oscilloscope is to focus the transducer. Focusing the transducer was discussed in the section entitled "Basic Theory of Operation".

Appendix B

Fabrication of the Defective and the Unflawed Laminates

1. All of the plates were made of "Scotchply Reinforced Plastic-1003 Unidirectional Prepreg".
2. Each plate measured 12 inches square and had 16 plies.
3. The stacking sequence of each plate was $[0/45/90/-45]_{2s}$. Circular defects were placed between the eighth and ninth plies of the defective panels.

   A. The defects were fabricated as follows:

      i. Two pieces of clear Teflon film were laid on top of one another.

      ii. A piece of 600 grit sandpaper was placed under the two layers of Teflon film. The grit of the sandpaper held the two pieces of film together so they would not separate during the cure cycle.

      iii. Four hollow punches, measuring 1.000 inches, 0.875 inches, 0.750 inches, and 0.500 inches in diameter, were used to punch out the defects.

   B. The defects were located as follows:

      i. One defect of each size was placed in the plate.

      ii. The defects were located as shown in Figure 61.

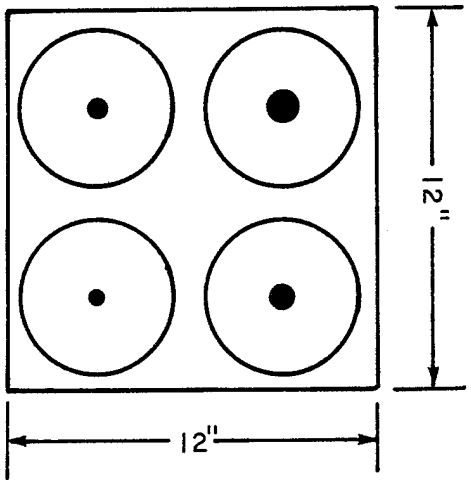

Defective Panel Layout

Figure 61

4. The plates were prepared for the autoclave as follows: (see Figure 62)
   A. Release agent was applied to the surface of the aluminum processing plate.
   B. Each side of the prepreg laminate was covered with a piece of Peel Ply cloth.
   C. A piece of clear Teflon film, cut to fit the prepreg laminate, was laid on the aluminum plate. The film prevented the laminate from sticking to the plate during the cure cycle.
   D. The laminate was laid on the Teflon film.
   E. Two layers of Corprene Cork dam material were placed around the edges of the laminate.

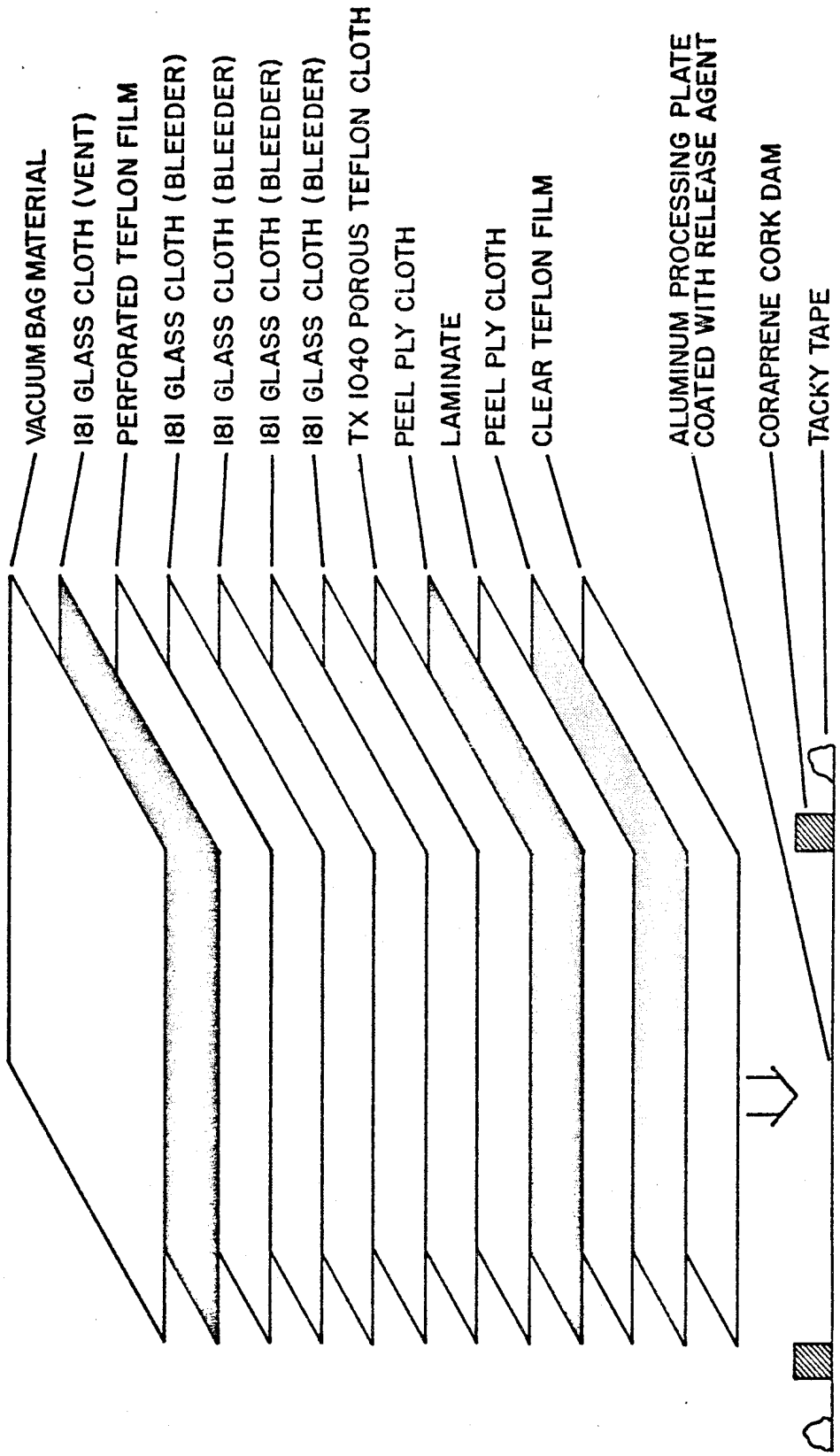

Figure 62 Autoclave Preparation

F. Tx 1040 Teflon cloth, cut to fit, was laid on the laminate.

G. Four pieces of 181 Glass cloth (one piece of cloth for every four plies in the laminate), cut to fit, were placed on top of the Teflon cloth.

H. A piece of clear Teflon film, approximately 13 inches square and perforated (1 hole/in^2), was laid over the Glass cloth.

I. 181 Glass cloth was placed over the Teflon film to act as a vent cloth.

J. Vacuum bag material was laid over the vent cloth and was sealed to the aluminum plate with Tacky tape.

5. The panel was cured in the autoclave using the following cure cycle:

A. A vacuum of 30 inches of Mercury was drawn in the vacuum bag.

B. The plate was heated to 330^{o}F at a rate of approximately 20 degrees Fahrenheit per minute.

C. 50 psig of nitrogen was applied to the plate.

D. The plate was allowed to cure for 2 hours.

E. While under pressure, the plate was allowed to cool to 200^{o}F.

F. The pressure was released and the plate was allowed to cool to room temperature in the autoclave overnight (approximately 16 hours).

6. The plate was removed from the autoclave and all the cloths and films were removed.

Appendix C

Fabrication of the Defective and the Unflawed Disks

1. Each plate was ultrasonically "C" scanned in order to locate the implanted defects and any other imperfections.
2. Using a compass and a ruler, four five inch diameter disks were laid out. When the disks were taken from the unflawed plates, they were taken from as near the center of the plate as possible to eliminate edge effects such as non-uniform thickness. When the disks were taken from the defective plates, the defects were placed at the center of the disks.
3. The disks were cut out on a band saw.
4. A belt sander was used to "round" the disks.
5. The disks were "C" scanned to detect any damage incurred through sawing and sanding. Before scanning each disk, however, they were numbered using the following number scheme. The first one or two digits denotes the plate from which the disk was taken; plates 1-7 contain no implanted Teflon defects while plates 8-13 contain implanted Teflon defects. The last digit indicates the size of the implanted defect. A one indicates a half inch defect, a two indicates a three-quarter inch defect and so on. In the case of plates 1-7, the last digit is arbitrarily a 1, 2, 3, or 4. For example, the four disks taken from panel 5 were numbered 51, 52, 53, and 54, respectively. Figures 63 and 64 show "C" scans of a defective disk and a pristine disk, respectively.

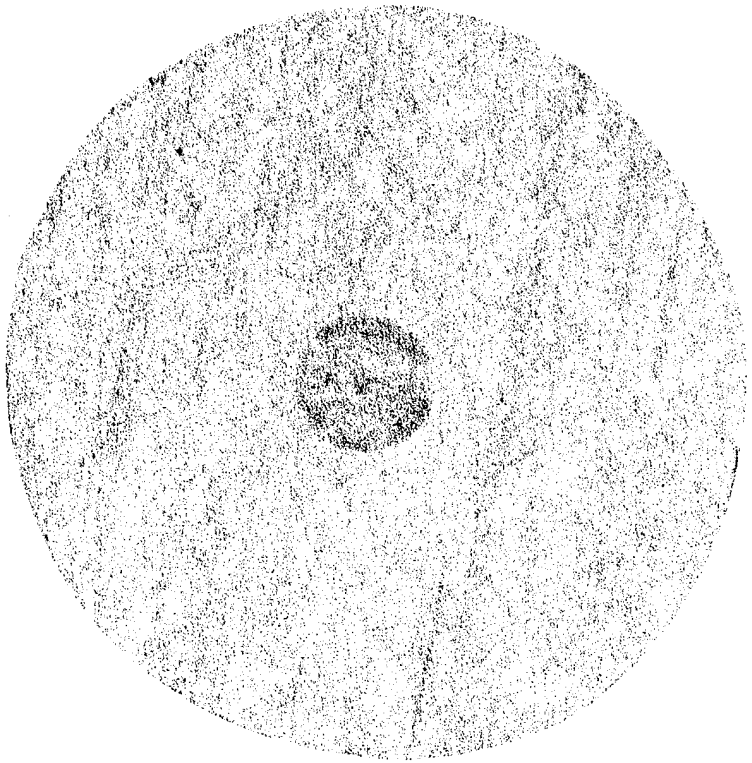

Scan of a Defective Disk

Figure 63

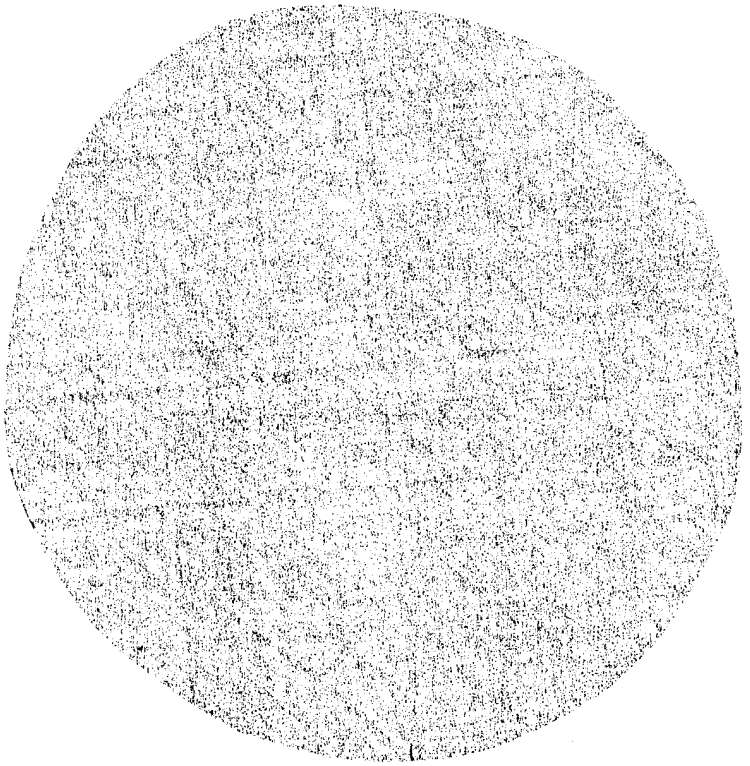

Scan of a Pristine Disk

Figure 64

Appendix D

The Deflection Solution for an Isotropic, Axisymmetric, Circular Plate [3]

The governing equation for the deflection of an isotropic, axisymmetric circular plate in polar coordinates (r, θ, z) is:

$$\nabla^4 w = p(r)/D \quad \ldots\ldots\ldots\ldots\ldots\ldots\ldots\ldots\ldots\ldots \quad (1)$$

where w is the displacement in the z direction, ∇^4 is the bi-harmonic operator, p(r) is the lateral loading, and D is the flexural stiffness of the plate. For this study, p(r) = 0 and the governing equation of the plate becomes:

$$\nabla^4 w = 0 \quad \ldots\ldots\ldots\ldots\ldots\ldots\ldots\ldots\ldots\ldots \quad (2)$$

The solution of this equation is:

$$w(r) = C_1 + C_2 r^2 + C_3 \log r + C_4 r^2 \log r \quad \ldots\ldots\ldots\ldots \quad (3)$$

where C_1, C_2 , C_3, and C_4 are constants and r is any radius of the plate. A concentrated load at r = 0 implies $C_3 = 0$ and $C_4 = -P/(8\pi D)$, where P is the magnitude of the concentrated load. Substituting these constants into (3) implies:

$$w(r) = C_1 + C_2 r^2 - P r^2 \log r/(8\pi D) \quad \ldots\ldots\ldots\ldots\ldots \quad (4)$$

The initial conditions for a simply supported plate of radius a are:

$w(r = a) = 0$ . . . . (5)

$Mr(r = a) = 0$ . . . . (6)

where Mr is a stress couple in the r direction.

Utilizing equation (4) and equation (5):

$w(a) = C_1 + C_2a^2 - Pa^2\log a/(8\pi D) = 0$ . . . . (7)

For a plate:

$M(r) = -2D(1 + \nu)C_2 + C_4D(-2(1 + \nu)\log r - (3 + \nu))$ . . . (8)

where ν is Poisson's ratio for the plate.

Utilizing equation (6) and equation (8) and the fact that $C_4 = -P/(8\pi D)$ implies:

$M(a) = -2D(1+\nu)C_2 - PD(-2(1+\nu)\log a-(3+\nu))/(8\pi D) = 0$ . . (9)

Solving (9) for C_2 implies:

$C_2= P(\log a + (3 + \nu)/(2 + 2\nu))/(8\pi D)$ . . . .(10)

Substituting (10) into (7) and solving for C_1 gives:

$C_1 = P(-a^2(3 + \nu)/(2 + 2\nu))/(8\pi D)$ . . . . (11)

Plugging (10) and (11) into (4) and simplifying provides the deflection w, at any radius:

$w(r) = P(r^2\log(a/r) + (r^2-a^2)(3+\nu)/(2+2\nu))/(8\pi D)$ . . . (12)

For the plate under consideration, equation (12) can be simplified by substituting the effective properties of the laminate as well as the values of a and h (the thickness of the plate):

E(effective) = 3.114E6 psi a = 2.375 in.

ν(effective) = 0.3078 h = 0.134 in.

D, the flexural stiffness, is found through the following equation:

$$D = Eh^3/(12(1 - \nu^2)) \quad \ldots\ldots\ldots\ldots\ldots\ldots\ldots\ldots \quad (13)$$

where E is the effective Elastic modulus of the laminated plate and ν is the effective Poisson's ratio for the plate. Substituting the values listed above and the number obtained from equation (13) into equation (12), the expression for w(r) becomes:

$$w(r) = (5.769\ E\text{-}5)\ P\ (r^2(\log(2.375/r) + 1.265) - 7.135) \quad \ldots (14)$$

The final expression for w(r) is obtained by substituting the magnitude of the concentrated load P. For this analysis P = 440 lb, and w(r) becomes:

$$w(r) = (2.538\ E\text{-}2)(r^2(\log(2.375/r) + 1.265) - 7.135) \text{ in} \quad \ldots (15)$$

Appendix E

The Derivation of an Expression for the Radial Strain [4]

Assuming no buckling loads, the stresses within a plate in the x and y directions are:

$$\sigma x = (Mx\ 12z)/h^3 \quad \ldots\ldots\ldots\ldots\ldots\ldots\ldots\ldots\ (1)$$

$$\sigma y = (My\ 12z)/h^3 \quad \ldots\ldots\ldots\ldots\ldots\ldots\ldots\ldots\ (2)$$

where h is the thickness of the plate, Mx is the stress couple in the x direction, My is the stress couple in the y direction, and z is the out of plane distance from the center of the plate. For the disks used in this experiment, h = 0.134 in.. The bending moment components of the plate (i.e. the stress couples) that are given in the output of the finite-element program are the bending moment components at the surface of the plate. This implies that z = h/2 = 0.67 in.. For each element in the finite mesh, the finite-element program states that x is analogous to r and y is analogous to θ in the element's coordinate system. Thus equations (1) and (2) reduce to the following polar equations:

$$\sigma r = 334.15\ Mr \quad \ldots\ldots\ldots\ldots\ldots\ldots\ldots\ldots\ (3)$$

$$\sigma\theta = 334.15\ M\theta \quad \ldots\ldots\ldots\ldots\ldots\ldots\ldots\ldots\ (4)$$

The radial strain, εr, is given by the following equation:

$$\varepsilon r = \sigma r/Er - \nu\theta r\ \sigma\theta)/E\theta \quad \ldots\ldots\ldots\ldots\ldots\ldots\ (5)$$

where Er is the Elastic modulus in the radial direction, $E\theta$ is the Elastic

modulus in the theta direction, and $\nu\theta r$ is minor Poisson's ratio and is equal to $-(\varepsilon r/\varepsilon\theta)$. Substituting equations (3) and (4) into equation (5) implies:

$$\varepsilon r = 334.15\ ((Mr/Er) - (\nu\theta r\ M\theta)/E\theta) \quad \ldots\ldots\ldots\ldots\ (6)$$

Using Table 6, the values of Er and $E\theta$ at 0^o (Ex' and Ey' respectively) are:

$$Er = 3.685\ E6\ psi \quad \ldots\ldots\ldots\ldots\ (7)$$

$$E\theta = 2.800\ E6\ psi \quad \ldots\ldots\ldots\ldots\ (8)$$

The effective Poisson's ratio of the laminate is $\nu xy = 0.3078$. At $\theta = 0^o$, $\nu xy = \nu r\theta = 0.3078$. Thus, to find $\nu\theta r$ at $\theta = 0^o$, the reciprocity relationship must be used:

$$\nu\theta r = (E\theta\ \nu r\theta)/Er = 0.2339 \quad \ldots\ldots\ldots\ldots\ (9)$$

Substituting equations (7), (8), and (9) into equation (6) produces an expression for the radial strain at $\theta = 0^o$:

$$\varepsilon r\ (\theta = 0^o) = (9.068\ E\text{-}5)\ Mr - (2.791\ E\text{-}5)\ M\theta \quad \ldots\ldots\ (10)$$

Again using Table 6, the values of Er and $E\theta$ at 90^o (Ex' and Ey' respectively) are:

$$Er = 2.800E6\ psi \quad \ldots\ldots\ldots\ldots\ (11)$$

$$E\theta = 3.685E6\ psi \quad \ldots\ldots\ldots\ldots\ (12)$$

At $\theta = 90^{o}$, $\nu xy = \nu \theta r = 0.3078$. Substituting equations (11) and (12) as well as $\nu \theta r = 0.3078$ into equation (6) produces an expression for the radial strain at $\theta = 90^{o}$:

$$\varepsilon r \ (\theta = 90^{o}) = (1.193 \text{ E-4}) \ Mr - (2.791 \text{ E-5}) \ M\theta \ . \ . \ . \ . \ . \ (13)$$